A Theoretical Analysis of the Current-Voltage Characteristics of Solar Cells

Annual Report on
NASA Grant NGR 34-002-195

June 1974

J. R. Hauser and P. M. Dunbar

Semiconductor Device Laboratory
Department of Electrical Engineering
North Carolina State University
Raleigh, North Carolina 27607

(NASA-CR-138828) A THEORETICAL ANALYSIS OF THE CURRENT-VOLTAGE CHARACTERISTICS OF SOLAR CELLS Annual Report (North Carolina State Univ.)
N74-28544
CSCL 10A G3/03
Unclas
54111

ABSTRACT

This report summarizes work to date performed under NASA Grant NGR 34-002-195, entitled A Theoretical Analysis of the Current-Voltage Characteristics of Solar Cells. The objective of the research is to provide a theoretical understanding of the operation of solar cells so they can be designed for maximum efficiency. These objectives are being pursued through the application of a general computer device analysis program to the study of solar cell properties. During the past twelve months considerable progress has been made toward these objectives. Specifically an analysis program for solar cells has been developed which provides for non-uniform doping profiles, generation-recombination effects, field and doping dependent mobility, and optical generation. Preliminary results with the analysis program indicates that the predicted efficiencies agree reasonably well with experimental efficiencies for silicon solar cells.

This report summarizes the major work to date on the current-voltage characteristics and efficiencies of solar cells. For one solar cell structure detailed curves are presented which include carrier densities, current densities, potential, and quasi-Fermi levels at different voltage levels both with and without optically generated carriers (AM0 conditions). In addition some results are presented concerning the influence of various parameter variations such as lifetime, cell thickness, and high-low junction width on solar cell performance.

I. COMPUTER ANALYSIS PROGRAM

A considerable part of the effort during this first year's research has been devoted to adapting a computer device analysis program to the analysis of solar cells. The present computer analysis program is able to account for the following physical effects in a semiconductor device:

1. Drift and diffusion currents
2. Non-uniform doping profiles
3. Bulk generation-recombination effects
4. Field dependent and doping dependent mobility
5. Optical carrier generation
6. Surface recombination

The effects above which have been included in the analysis program during the present research work are non-uniform doping profiles, optical carrier generation, and surface recombination.

Two papers have been prepared for submission for publication. One of these discusses the computer analysis program and the mathematical techniques used to solve the nonlinear semiconductor device equations, while the other discusses the studies which have been carried out on optical carrier generation and the effects of antireflecting layers on optical carrier generation in silicon. Copies of these manuscripts are included in Appendices A and B. These provide detailed summaries of the work performed on developing the computer analysis programs.

II. DETAILED CHARACTERISTICS AND PROPERTIES OF n^+-p-p^+ SOLAR CELLS

A considerable number of detailed calculations have been made of the electrostatic potential, quasi-Fermi levels, carrier densities, and current densities in solar cells. Both the conventional n^+-p cell and the back surface field (or high-low junction) n^+-p-p^+ cell, as shown in cross section in Figure 1, have been analyzed. More effort has been directed toward the n^+-p-p^+ structure than the conventional cell because of questions concerning the enhanced efficiency of the n^+-p-p^+ cell.

Since the device analysis program solves for the internal potential and quasi-Fermi levels, it provides a detailed look at the internal operation of the solar cell. A large amount of data is generated on each device studied. The results presented in this section show detailed internal characteristics for one particular solar cell under both conditions of no illumination and under the full solar spectrum illumination (AM0). Material and dimensional properties of the device for which detailed plots are presented are given in Table I. The lifetime of 100 μsec in the

Table I. Material and dimensional properties

Overall cell thickness	-	250 μM
n^+ thickness	-	0.25 μM
p^+ thickness	-	0.50 μM
n^+ surface concentration	-	$10^{20}/cm^3$
p doping concentration (10 Ω·cm)	-	$1.3x10^{15}/cm^3$
p^+ doping concentration	-	$10^{18}/cm^3$
minority carrier lifetime τ_{no}	-	100 μsec
τ_{po}	-	0.1 μsec

p-region corresponds to a diffusion length of about 588 μM or a little more than twice the cell thickness. The first sequence of Figures 2-8 show the device characteristics without illumination. Figure 2 shows the electrostatic potential across the device with 2(a) showing the entire device length while 2(b) and 2(c) shows expanded views about the $p\text{-}n^+$ and $p^+\text{-}p$ junctions respectively. The various curves correspond to applied voltages ranging from 0.1 to 0.7 volts. The expanded views are needed to see details about the junctions because of their small thickness. Of special interest in this figure is the reduction in potential across the high-low junction as seen in Figure 2(c) for large values of applied voltage. This reduction begins to occur when the minority carrier density exceeds the doping in the p-region, i.e. when high injection occurs.

Figures 3(a), 3(b), and 3(c) show complete and expanded plots of electron quasi-Fermi level in the device. The expanded plots illustrate that the quasi-Fermi level is essentially constant across both junction space charge regions as is assumed in most first order analytical device calculations. This first order assumption is not made in this calculation but it is seen that relatively constant quasi-Fermi levels in the space charge regions do in fact result. The major feature of these plots is the almost abrupt change in ϕ_n' as seen in Figure 3(c) at the high-low junction. This change in slope is required because of the essentially constant current density across the high-low junction coupled with the large change in electron density across the high-low junction.

Figure 4(b) shows the hole quasi-Fermi level around the $p\text{-}n^+$ junction. Plots for the $p\text{-}p^+$ junction are not shown since ϕ_p is essentially constant in this region as seen from Figure 4(a). Changes in ϕ_p only occur very near the surface, and these large changes only occur because of the value of surface recombination used in the calculations (infinite value used).

Figures 5(a), 5(b), and 5(c) show electron concentration for the complete device and expanded views near the two surfaces for various applied voltage values. The large changes in carrier density across the high-low junction as seen in Figure 5(c) illustrate the minority carrier reflecting properties of the high-low junction. The log scales used to plot electron density are needed to cover the large range of densities encountered as the applied voltage ranges from 0.1 volt to 0.7 volt; however, these log scales tend to distort somewhat the carrier density plots. For example the electron concentrations in the p^+ region as shown in Figure 5(c) from 0 to 0.5 μM vary approximately linearly with distance. This linear variation plots on a log scale as a very rapidly varying function near zero and a slowly varying function as 0.5 μM is approached. The very rapid decrease in electron concentration near the back contact is due to the assumption of an ohmic contact. This does not allow the carrier density to increase from its equilibrium value which is slightly above $10^2/\text{cm}^3$. The change in electron concentration across the high-low junction is related to the high-low junction potential as

$$n_{p^+} = n_p \exp(-qV_{hl}/kT). \qquad (1)$$

The high-low junction potential is given as

$$V_{hl} = \frac{kT}{q} \ell n \left[\frac{N_{p^+}}{N_p}/(1 + n_p/N_p)\right]. \qquad (2)$$

The combination of Eqs. (1) and (2) gives

$$n_{p^+} = n_p \frac{N_p}{N_{p^+}} (1 + \frac{n_p}{N_p}). \tag{3}$$

This relationship, as discussed in Appendix C, is followed very accurately for the high-low junctions analyzed in this work.

Hole concentration curves are shown in Figures 6(a), 6(b), and 6(c) for both the complete device and expanded views about the two junctions. The hole density in the center of the device is seen to be constant and essentially independent of applied voltage except for the highest voltage values which correspond to high injection in the center p-region. Of special interest are the hole densities in Figure 6(c) for the n^+ surface region. This illustrates the injection of holes into the n^+ region ($x<0.25$ μM). The hole density exhibits a rapid decrease near $x=0$ due to the large surface recombination velocity assumed at the surface. For low values of surface recombination the hole density will not be forced to the low values (below $10^2/cm^3$) shown in Figure 6(c).

Electron and hole current densities as functions of distance at the various applied voltage values are shown in Figures 7 and 8. In this case expanded views are shown only for the surface n^+-p junction since the current densities are essentially constant through the p^+ region. As can be seen in Figures 7(b) and 8(b) at low forward voltages there is a large change in current density in the vicinity of the n^+-p junction ($x < 0.5$ μM). This occurs because a large part of the current density consists of recombination current from within the junction depletion region at low applied voltages.

A set of curves similar to those of Figures 2-8 are shown in Figures 9-15 for the same solar cell structure but including pair generation due to AMO illumination. The assumed surface condition is that of a polished surface with no antireflecting layer but reflection from the surface is taken into account. For this sequence of figures, the terminal voltage ranges from 0.6 volt to 0.0 volt with curves shown for 0.1 volt steps. The irradiated surface is at x = 250 μM. The open-circuit voltage condition occurs between the 0.5 volt and 0.6 volt curves. For all curves except the current density curves, the curves do not exhibit any unusual features near the open-circuit voltage condition.

The electrostatic potential curves of Figure 9 are for all practical purposes identical to those of Figure 2 in the absence of illumination. The potential distribution within the device is determined by the terminal voltage and is independent of the optical illumination.

The variation in the quasi-Fermi level can best be illustrated in conjunction with the carrier density curves. The illumination produces an excess electron and hole density which is quite evident in Figures 12 and 13. This excess carrier density is also indicated by the shift of the quasi-Fermi potentials. This shift is most evident for electrons in the p-region (ϕ_n of Figures 10(a) and 10(b)) and holes in the n^+ region (ϕ_p of Figure 11(b)). At lower bias the electron concentration in the p-region (Figure 12(a)) is greatly reduced near the n^+-p junction due to the collection of the electrons by this junction yielding the short circuit current. It can be noticed, however, from Figure 12(b) that the decrease in electron concentration near the junction is limited by the saturation drift velocity. The minimum electron density of around $2 \times 10^{10}/cm^3$ (near x = 0.5 μM in Figure 12(b)) is needed at the saturated carrier drift velocity to support the collected photocurrent. This is also present in Figure 13(b) which indicates that the saturation velocity is reached for holes. This is seen as the fairly flat region of hole density below x = 0.5 μM. The surface variation of p_{n^+} and ϕ_p, in Figures 13(b) and 11(b) also indicate the directional change in J_p due to surface recombination. The collection of the optically generated holes is evidenced by the small reverse curve in Figure 13(b) for voltages less than 0.4 v. Had velocity saturation not set in this would have been a much deeper curve. It is none the less quite evident that first order diffusion methods cannot properly model the case of high optical currents.

The effects of the various saturation mechanisms point out the need for future calculations to include the full generation term instead of the present methods of scaling up the results from the case of lower generation due to the absence of an antireflection layer. Included in these effects is that of high injection due to the carriers. It can be seen from Figure 12(a) that high injection (due to optical generation alone) is approached in the bulk p-region as the electron density approaches $10^{13}/cm^3$. For the situation of higher bulk generation rates it is quite likely that the high injection condition in the bulk would be met. Among other things this would alter the reflecting characteristics of the high-low junction. These conditions of drift velocity saturation and high injection could have significant effects on the terminal characteristics which would not be evident from calculations based alone on the lower generation rates.

The current density curves of Figures 14 and 15 are, as before, plotted in terms of absolute magnitude. The dips in these curves are in fact directional changes so the current does pass through zero at these points. There is no directional change in electron current for high bias (V_a = 0.6 v, Figure 14(a)) due to the overriding effect of the forward p-n junction current. At lower bias however, the predominant electron current consists of collection of optically generated carriers by the p-n^+ junction. The 0.5 v curve in Figure 14(a) represents a transitional region around the open circuit condition. For situations where the effective surface recombination velocity of the high-low junction is much lower, it has been observed that the directional change due to carriers supporting back contact recombination occurs much closer to the high-low junction than that illustrated in Figure 14(a).

The hole current density of Figure 15 illustrates a similar transitional curve but at a higher bias voltage (0.6 v) due to the lower forward pn junction hole current. The current lost due to surface recombination is quite evident from Figure 15(b), where a reversal of the current direction near the surface indicates current flow to the surface due to surface recombination. Realize that for the lower bias (less than 0.6 v) the predominant hole current consists of the optical component (except at the surface).

The terminal characteristics of this solar cell are shown in Figures 16, 17 and 18. The J-V characteristic in the absence of light is shown in Figure 16. This curve is typical of most silicon diodes. At voltages ranging from about 0.35 volt to about 0.55 volt the current density varies approximately as exp(qV/kT). At lower and higher voltages the current changes less rapidly with voltage approaching the approximate variation of exp(qV/2kT). The deviation from ideal behavior at low voltages arises from recombination of carriers within the junction depletion region while the high voltage deviation occurs because of high injection into the p-region.

The terminal J-V characteristic under illumination is seen in Figure 17. From this the short circuit current is seen to be about 34 ma and the open circuit voltage about 0.58 volt. The efficiency _vs_ voltage characteristic is seen in Figure 18 where the peak efficiency is slightly below 12%. This is the calculated efficiency without an antireflecting layer. The efficiency of such a cell with an antireflecting layer would be expected to be about 40% larger or between 16% and 17%. This calculated efficiency is significantly larger than that observed in commercial 10 Ω•cm solar cells. There are several possible reasons for this. First the lifetime of 100 μsec used in the p-region may be larger than that obtainable in present solar cells. Lifetime values of 10 μsec have frequently been quoted as typical lifetimes in 10 Ω•cm solar cells. Calculations for lower lifetime cells are given in the next section. The lifetime of 0.1 μsec used in the n^+ region may again be larger than actually obtained in commercail cells. However, very small values of lifetime are required in the n^+ layer to significantly reduce the efficiency because of the very thin n^+ region. It was also found that the calculated generation rate used in the presented data was about 10% high. As a result of this the efficiency results actually lie between that of a bare surface and that with a reflecting layer. Including this factor would lower the efficiency for the cell with the antireflecting layer to between 15 and 16%. The optical generation parameter presented in Appendix B represent the corrected generation rate.

There are other effects which may reduce the efficiency in real solar cells. The ohmic resistance due to a two-dimensional contact geometry reduces the curve factor decreasing the efficiency. Also heavy doping (degeneracy) effects in the emitter are not accounted for. These effects can enhance the loss of carriers at the surface and decrease the efficiency. These effects are to be incorporated into the theoretical analysis during the continued research work.

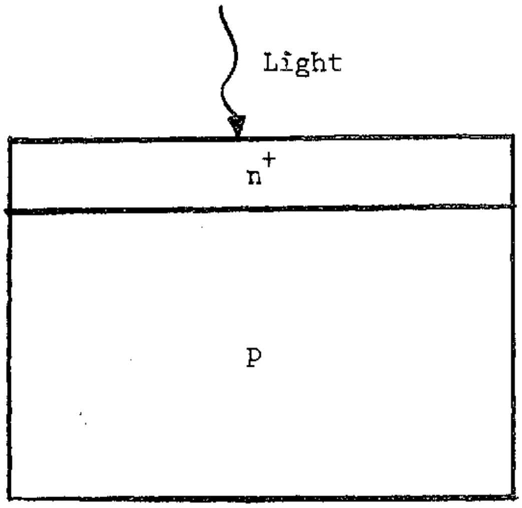

a. Conventional $p\text{-}n^+$ solar cell

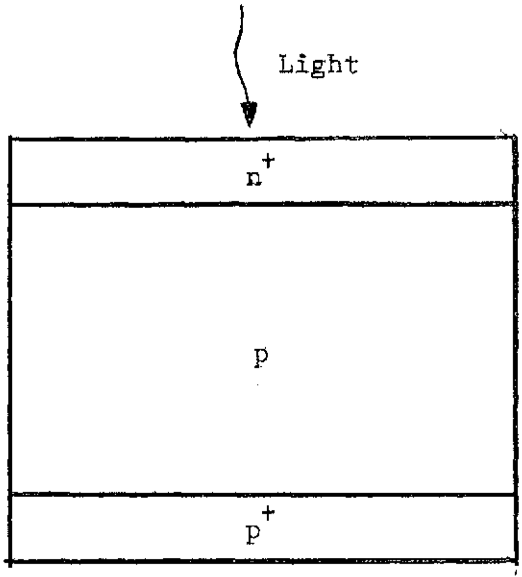

b. Back surface field, $p^+\text{-}p\text{-}n^+$ solar cell

Figure 1. Device structure utilized in the theoretical analysis.

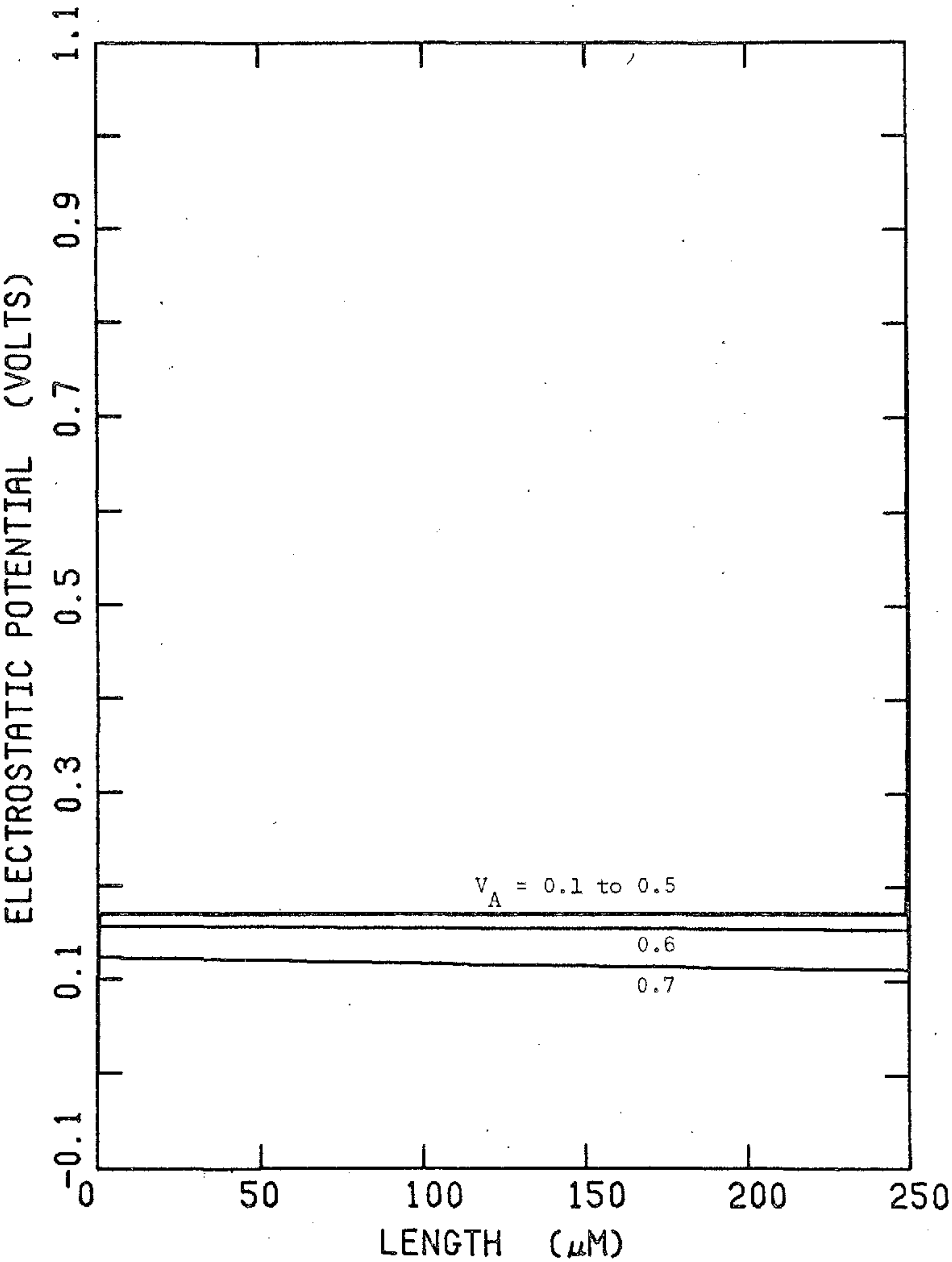

Figure 2a. Electrostatic potential variation throughout the entire device (no illumination).

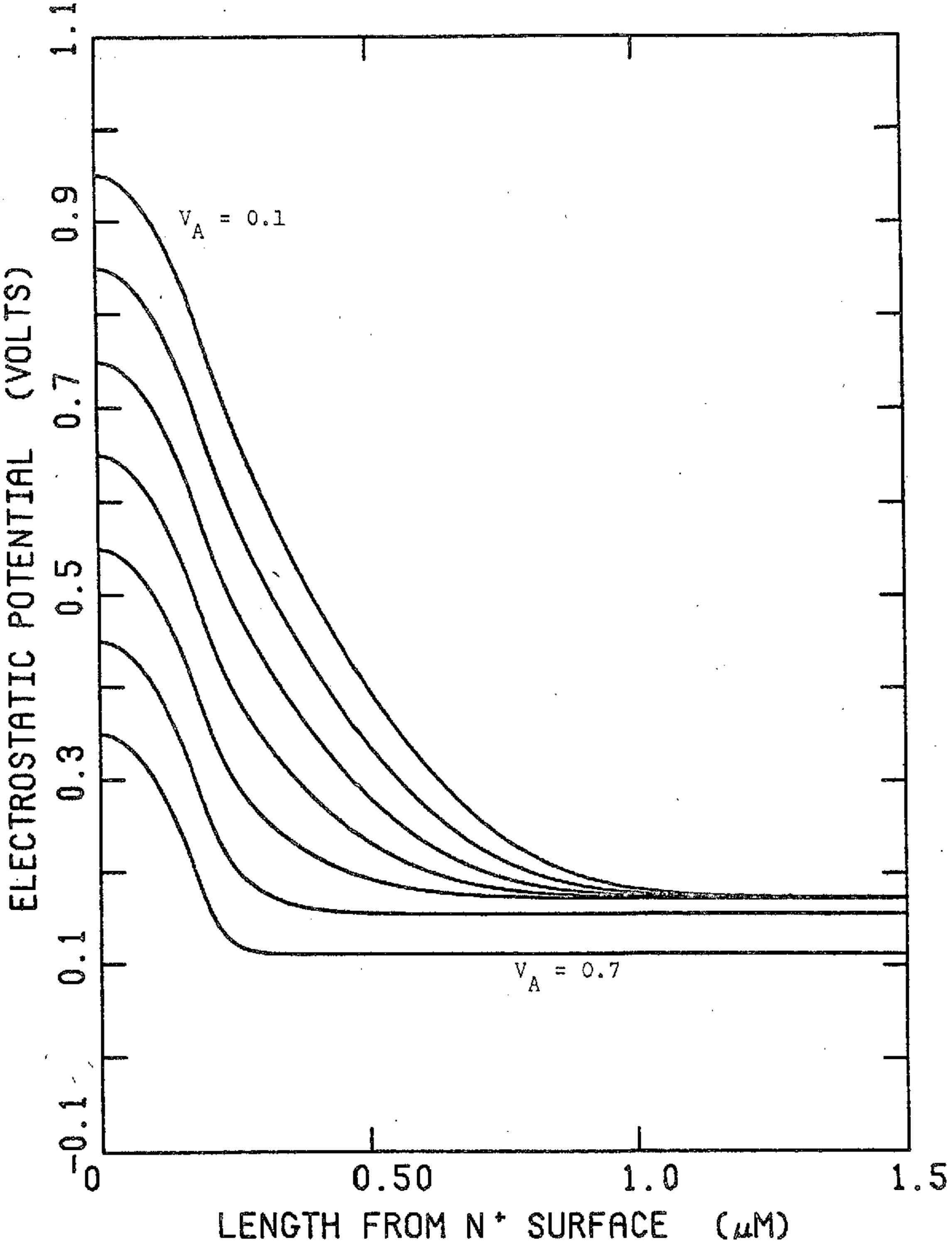

Figure 2b. Electrostatic potential variation about the p-n$^+$ junction (no illumination).

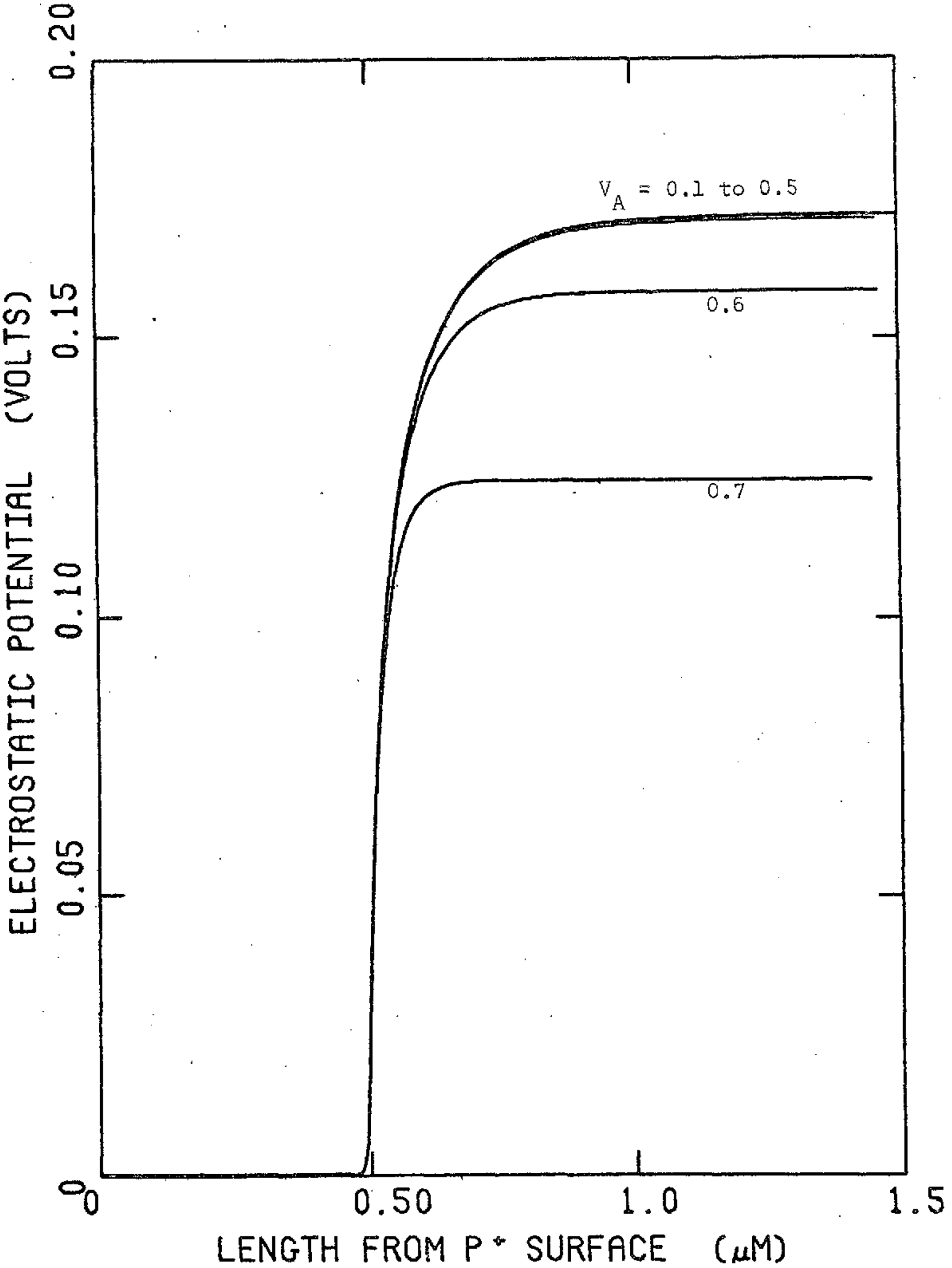

Figure 2c. Electrostatic potential variation about the high-low junction (no illumination).

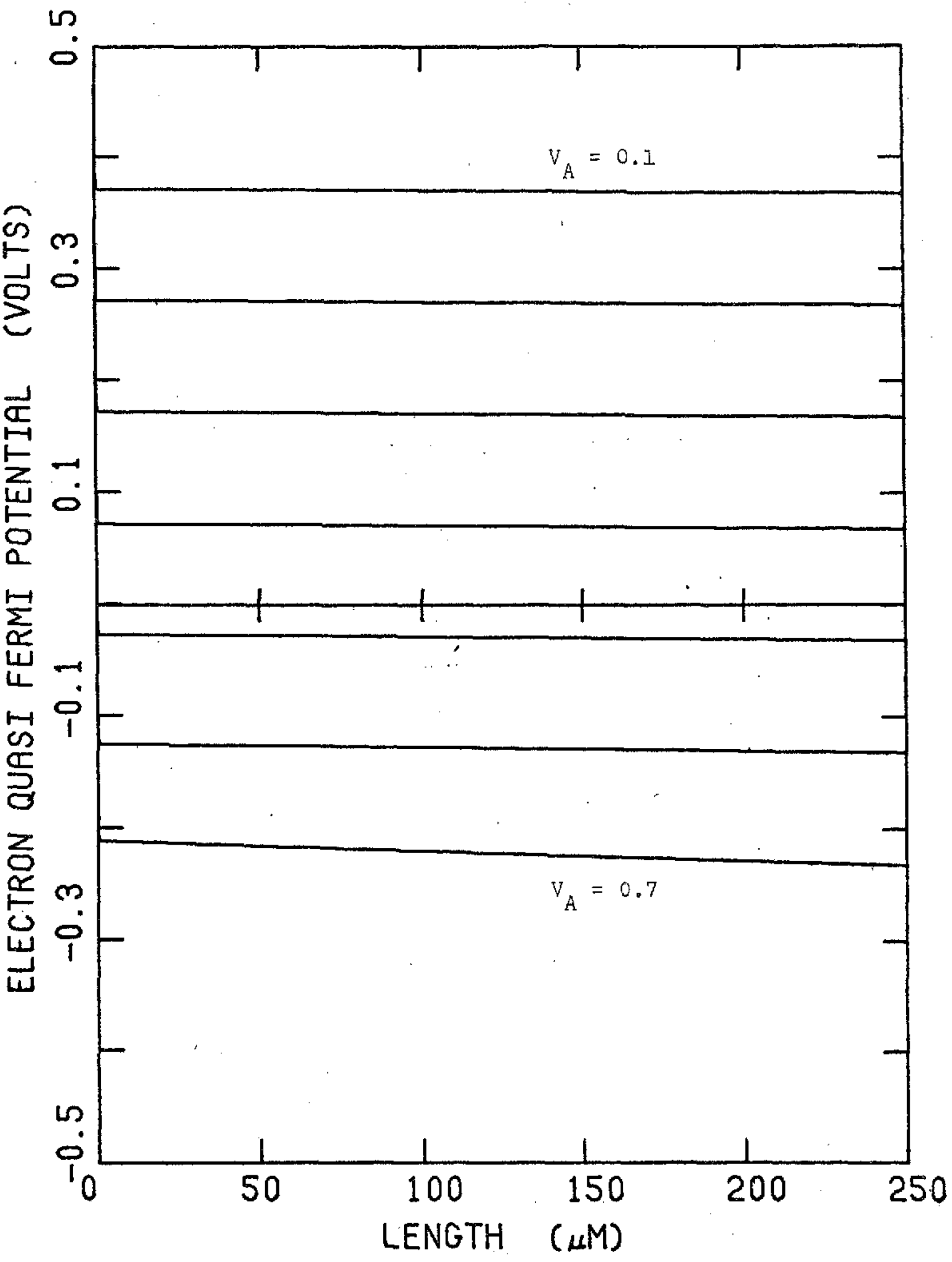

Figure 3a. Electron Quasi-Fermi potential variation throughout the entire device (no illumination).

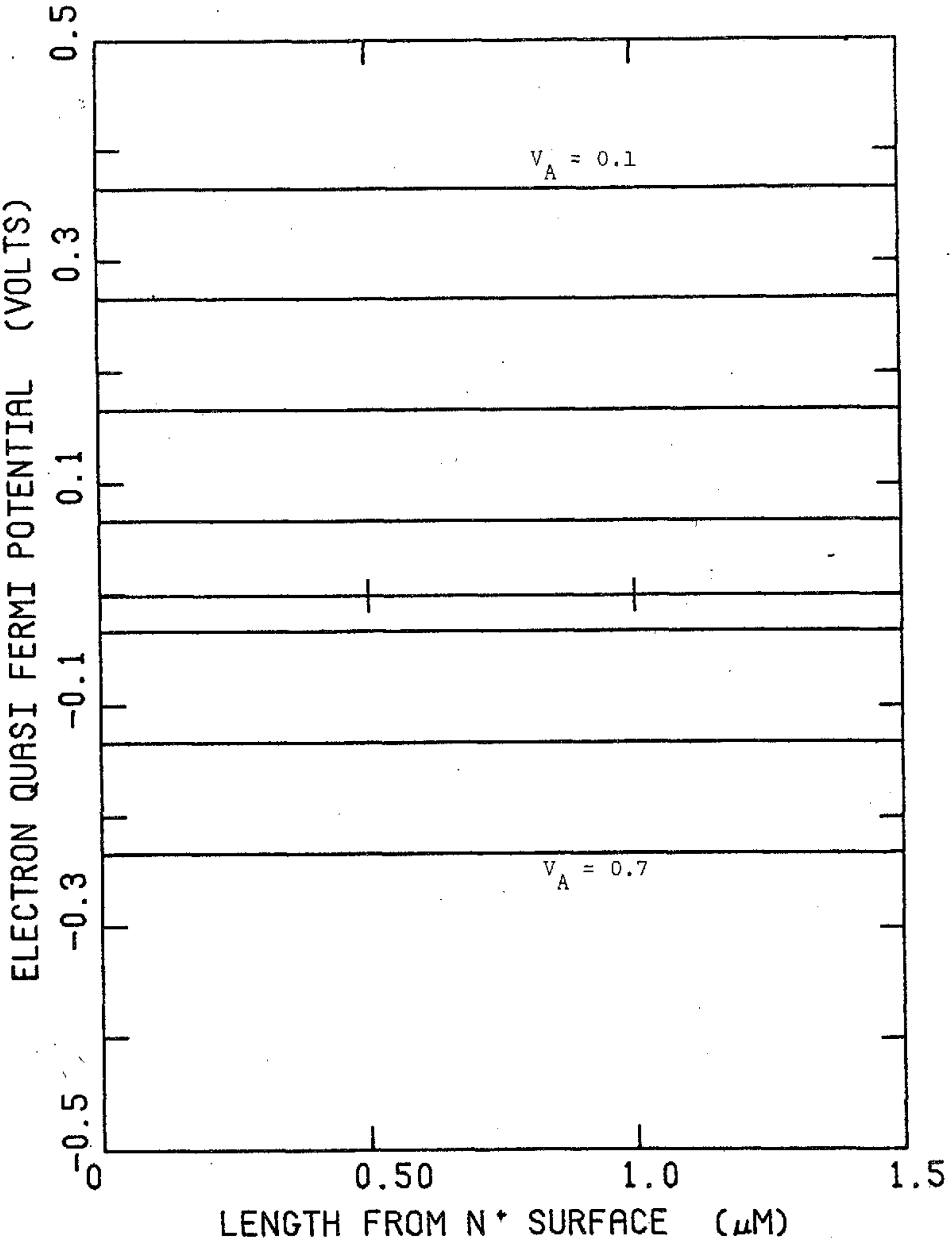

Figure 3b. Electron Quasi-Fermi potential variation about the p-n^+ junction (no illumination).

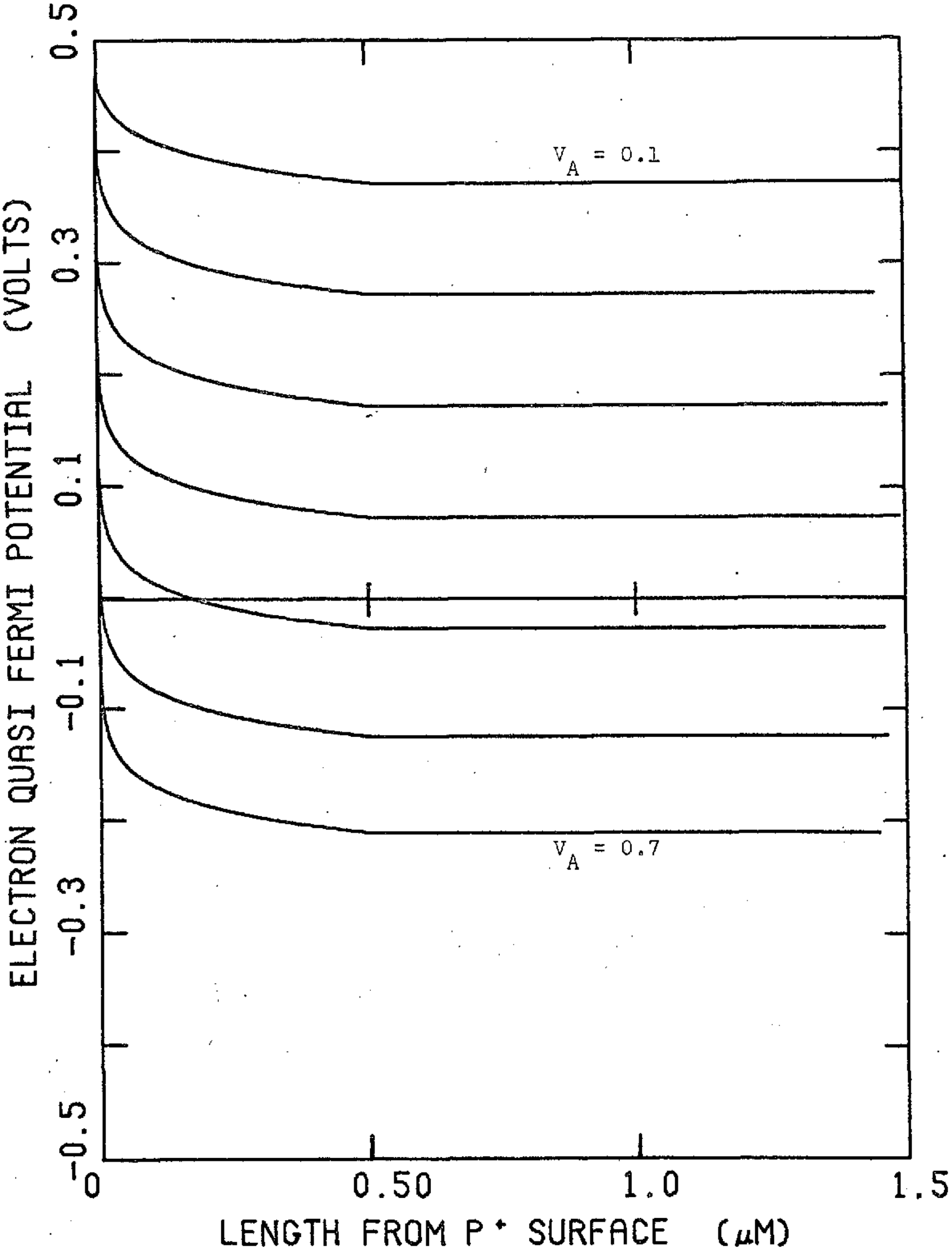

Figure 3c. Electron Quasi-Fermi potential variation about the high-low junction (no illumination).

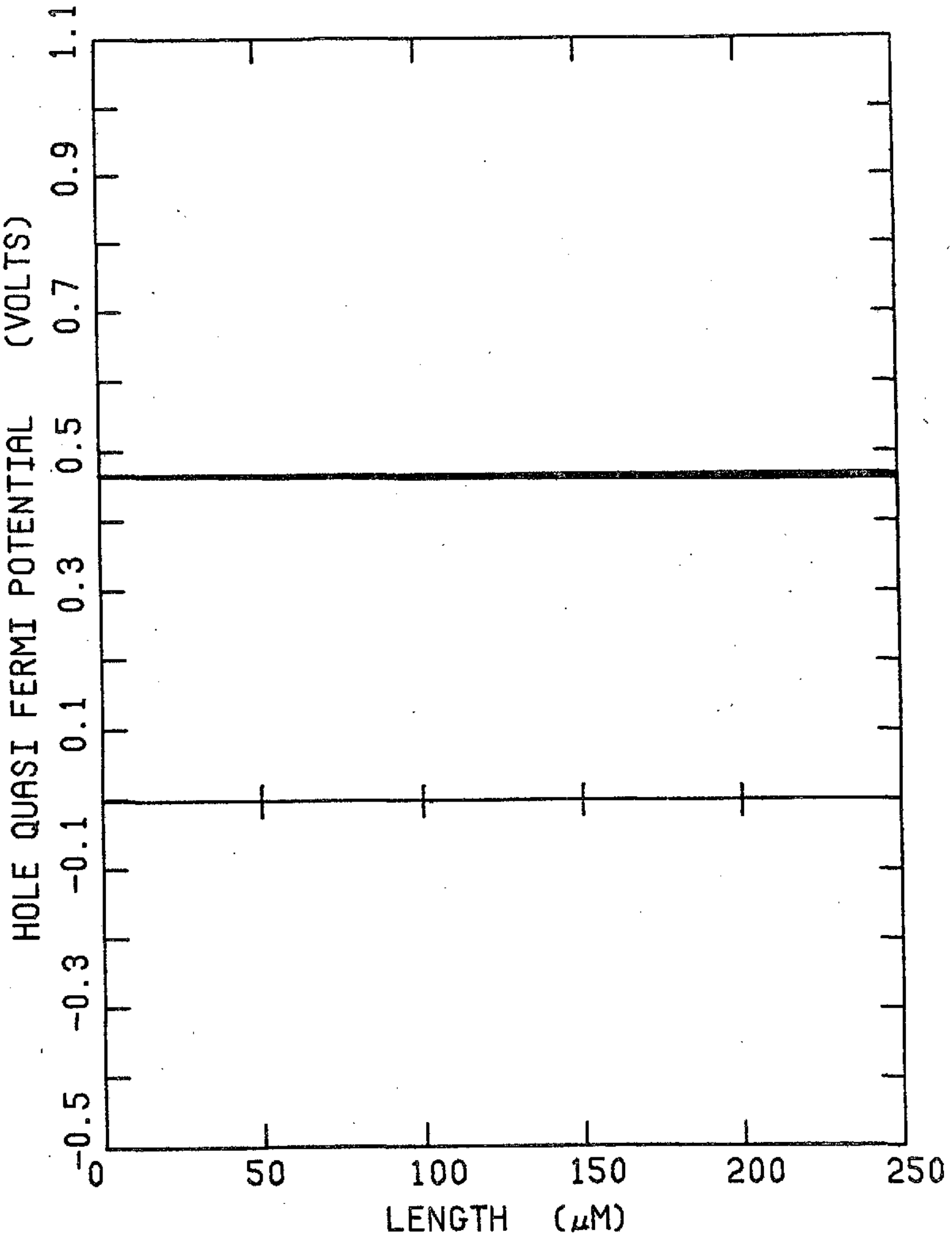

Figure 4a. Hole Quasi-Fermi potential variation throughout the entire device (no illumination).

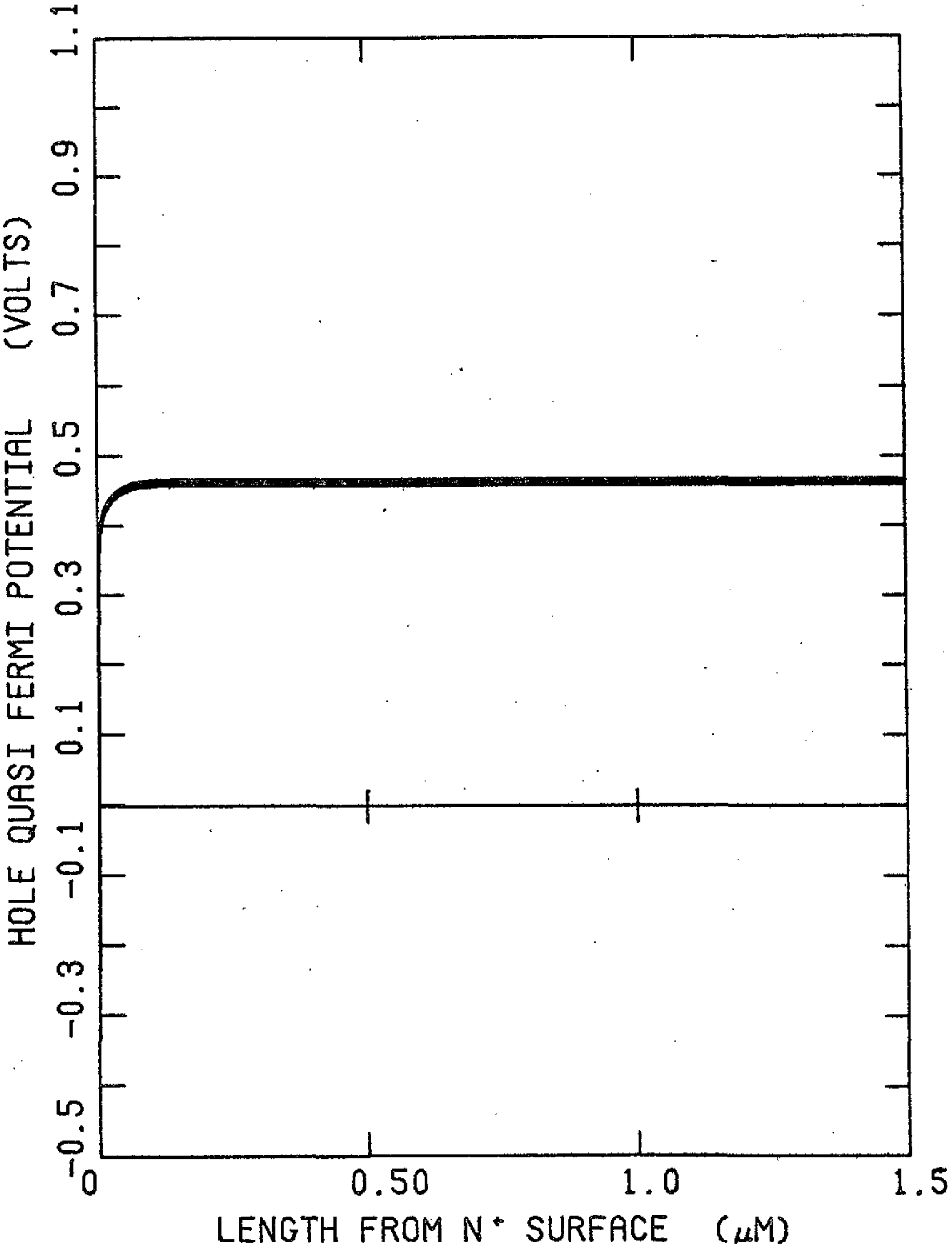

Figure 4b. Hole Quasi-Fermi potential variation about the p-n$^+$ junction (no illumination).

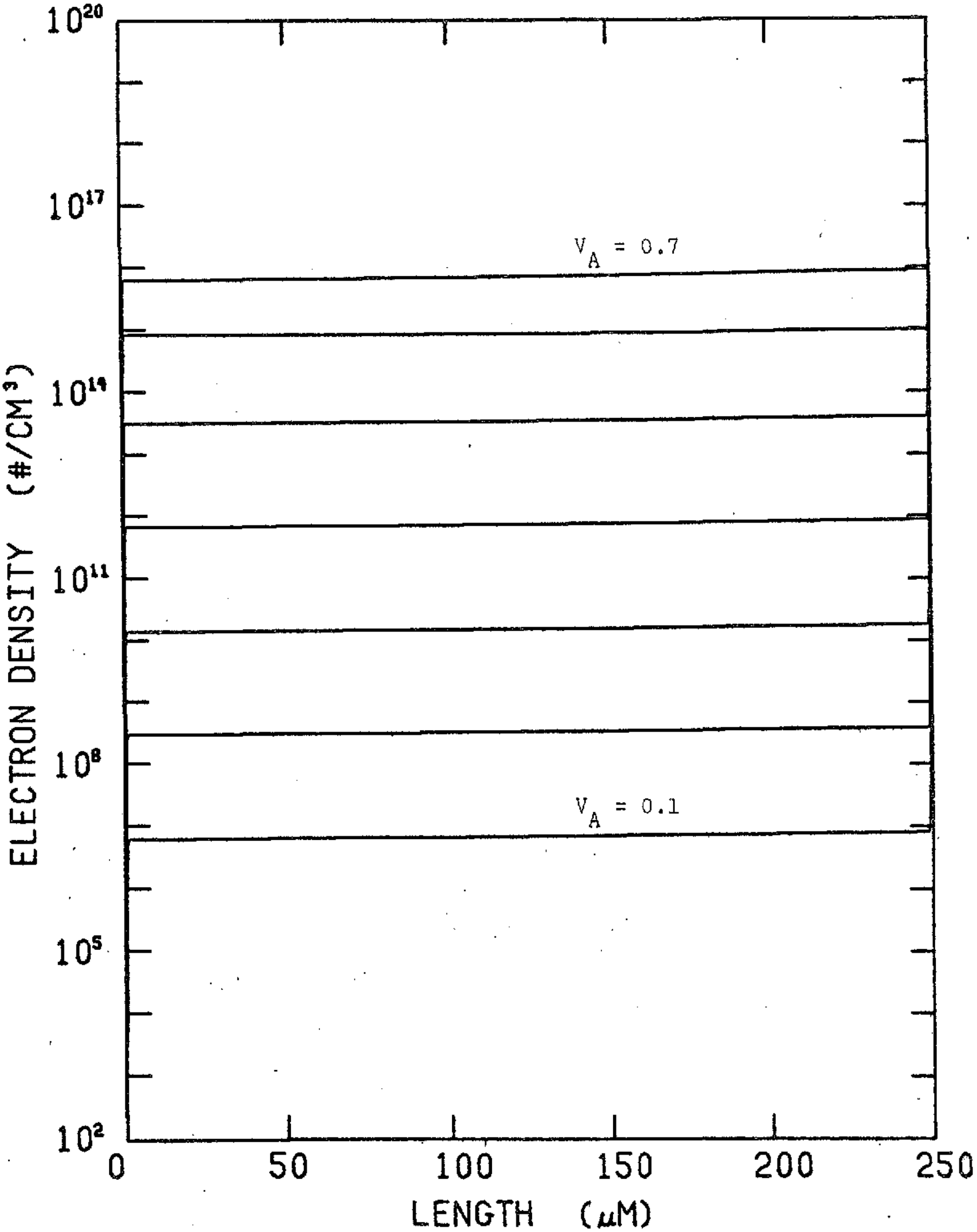

Figure 5a. Electron concentration throughout the entire device (no illumination).

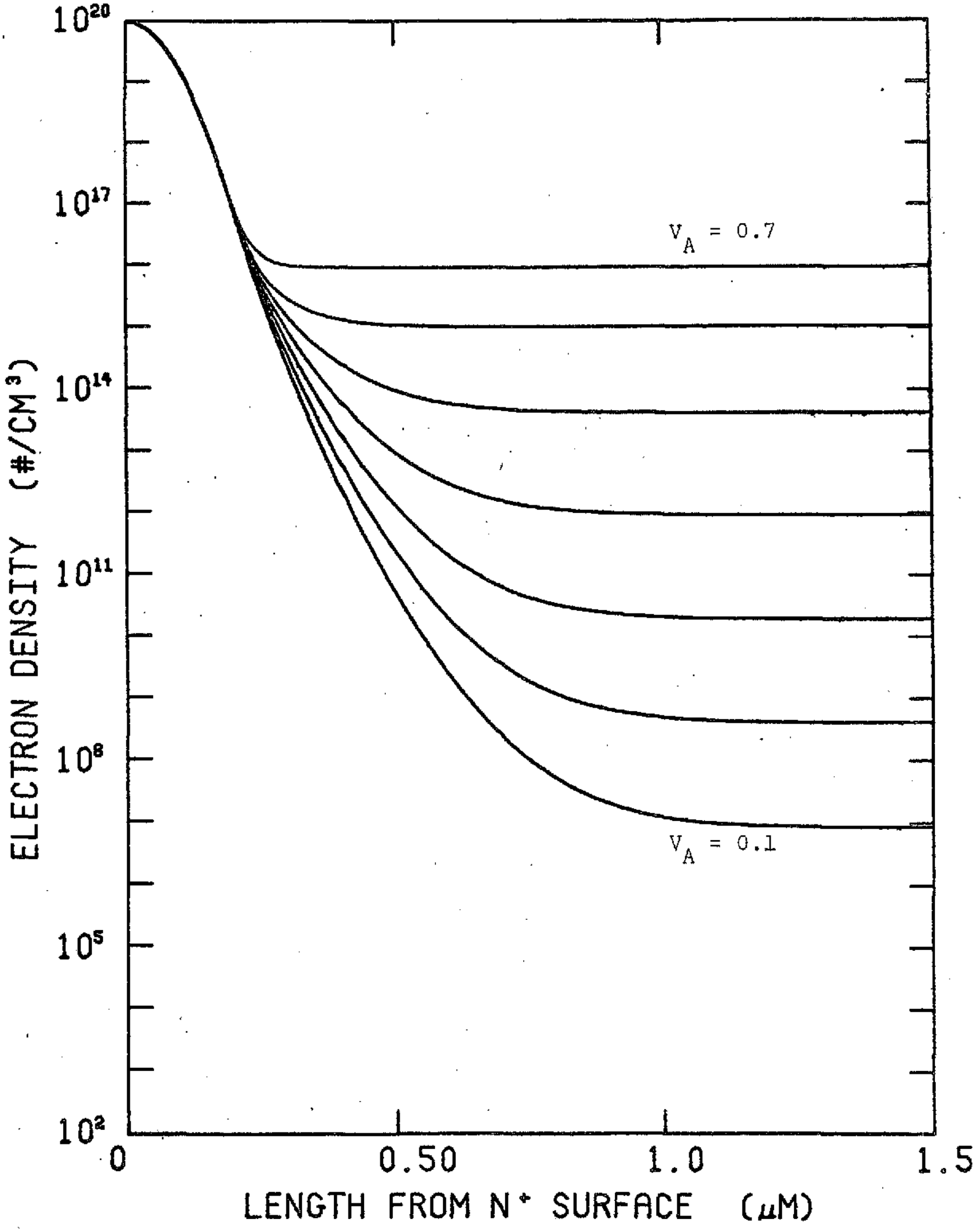

Figure 5b. Electron concentration about the n^+-p junction (no illumination).

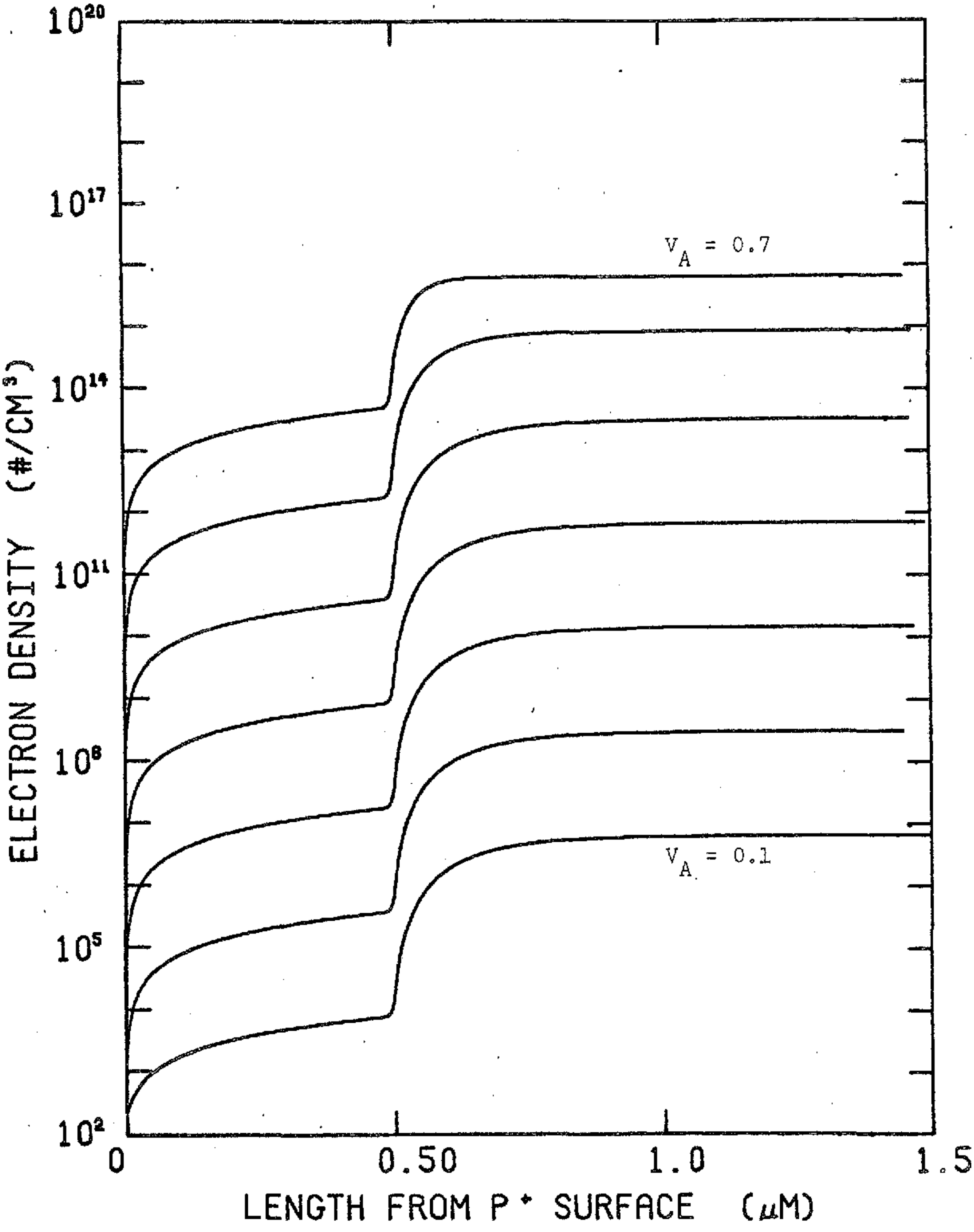

Figure 5c. Electron concentration about the high-low junction (no illumination).

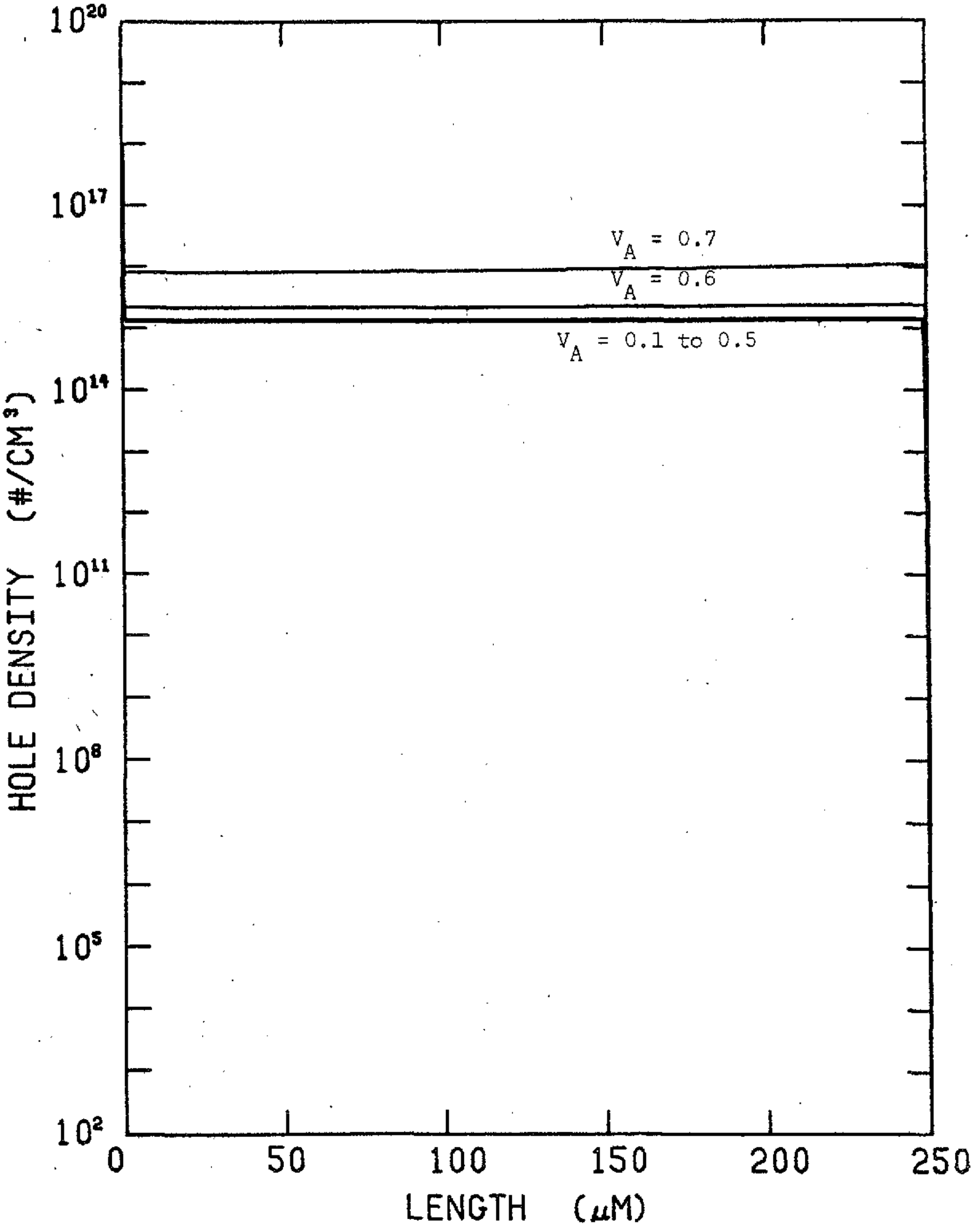

Figure 6a. Hole concentration throughout the entire device (no illumination).

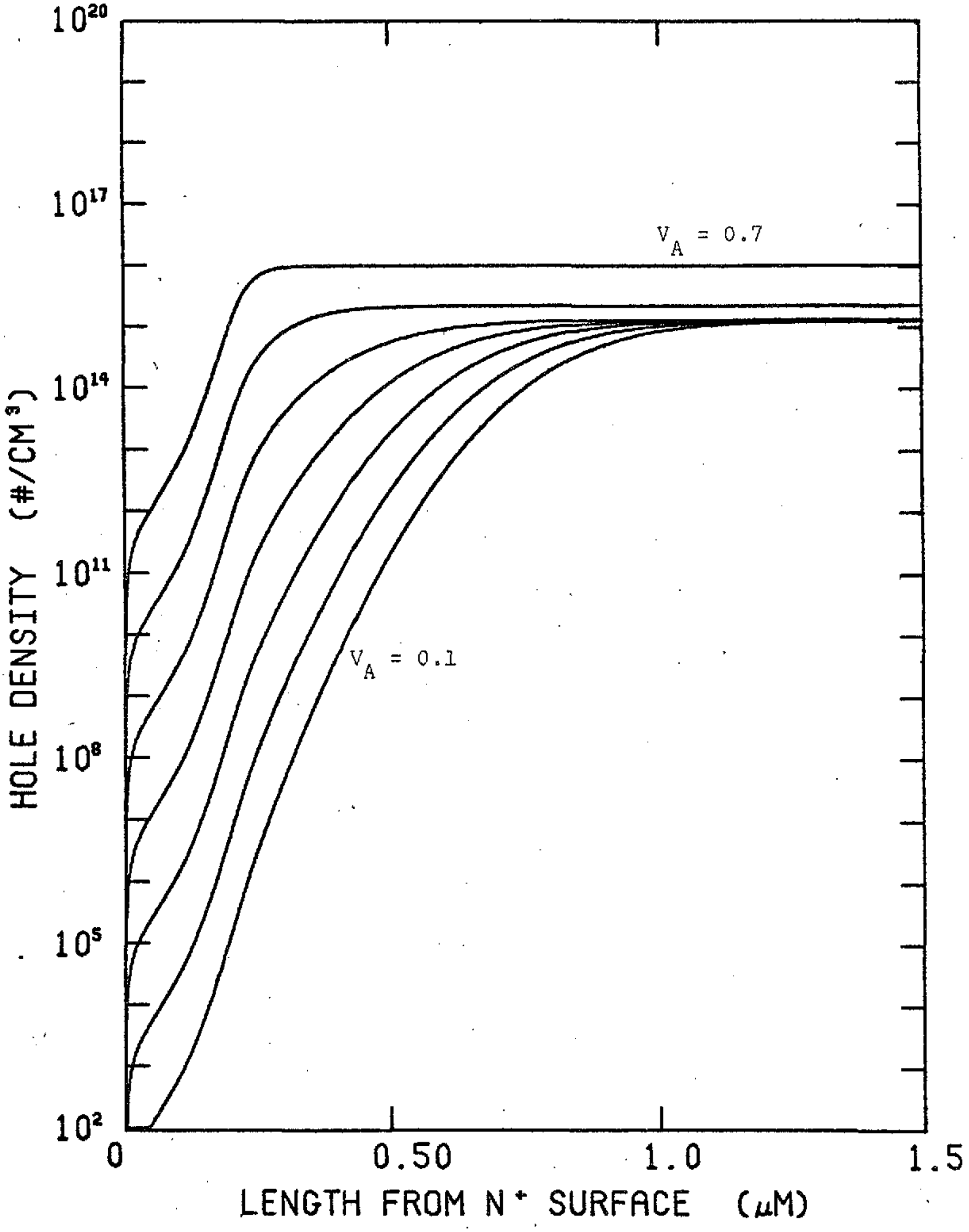

Figure 6b. Hole concentration about the n^+-p junction (no illumination).

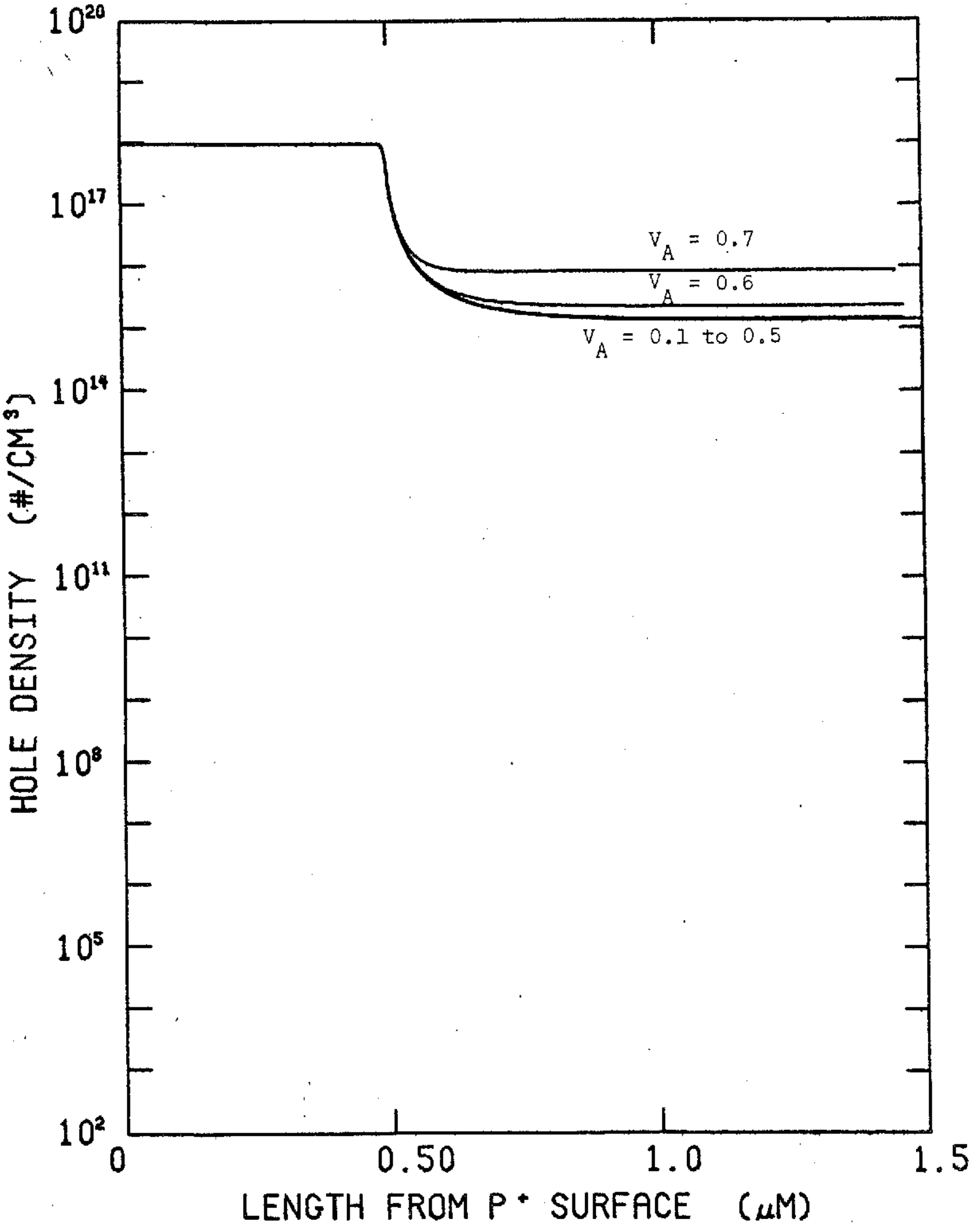

Figure 6c. Hole concentration about the high-low junction (no illumination).

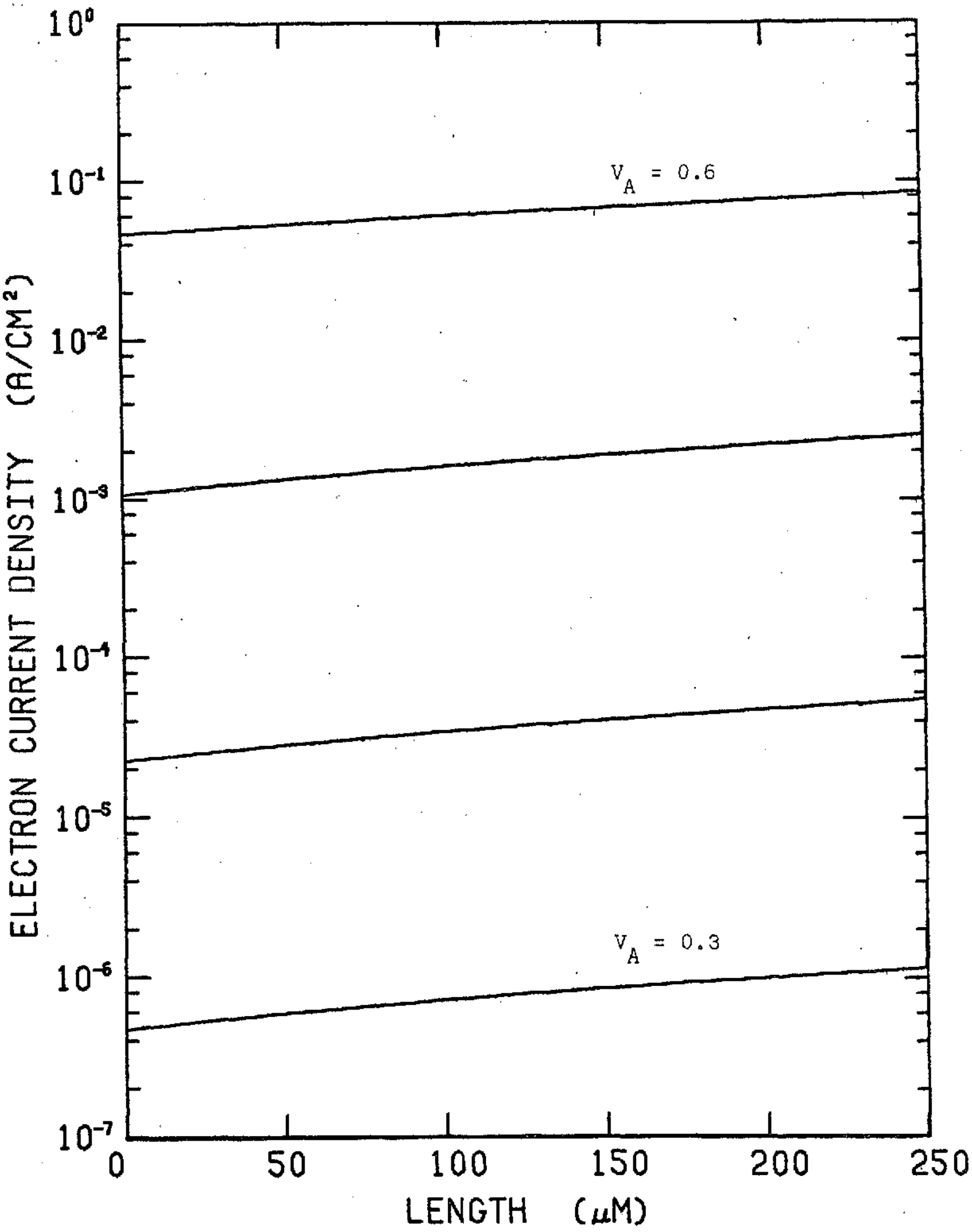

Figure 7a. Electron Current density variation throughout the entire device (no illumination).

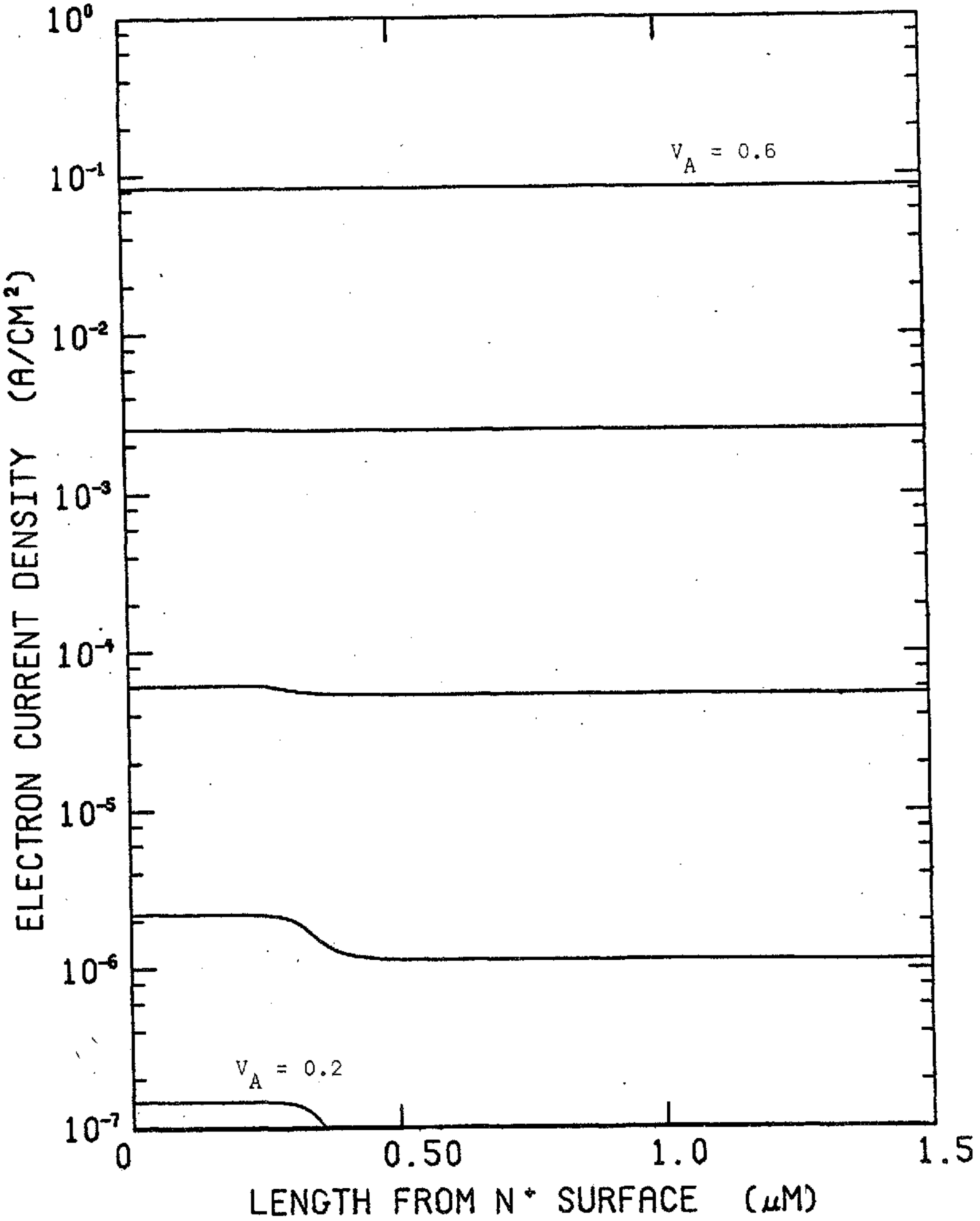

Figure 7b. Electron current density variation about the n^+-p junction (no illumination).

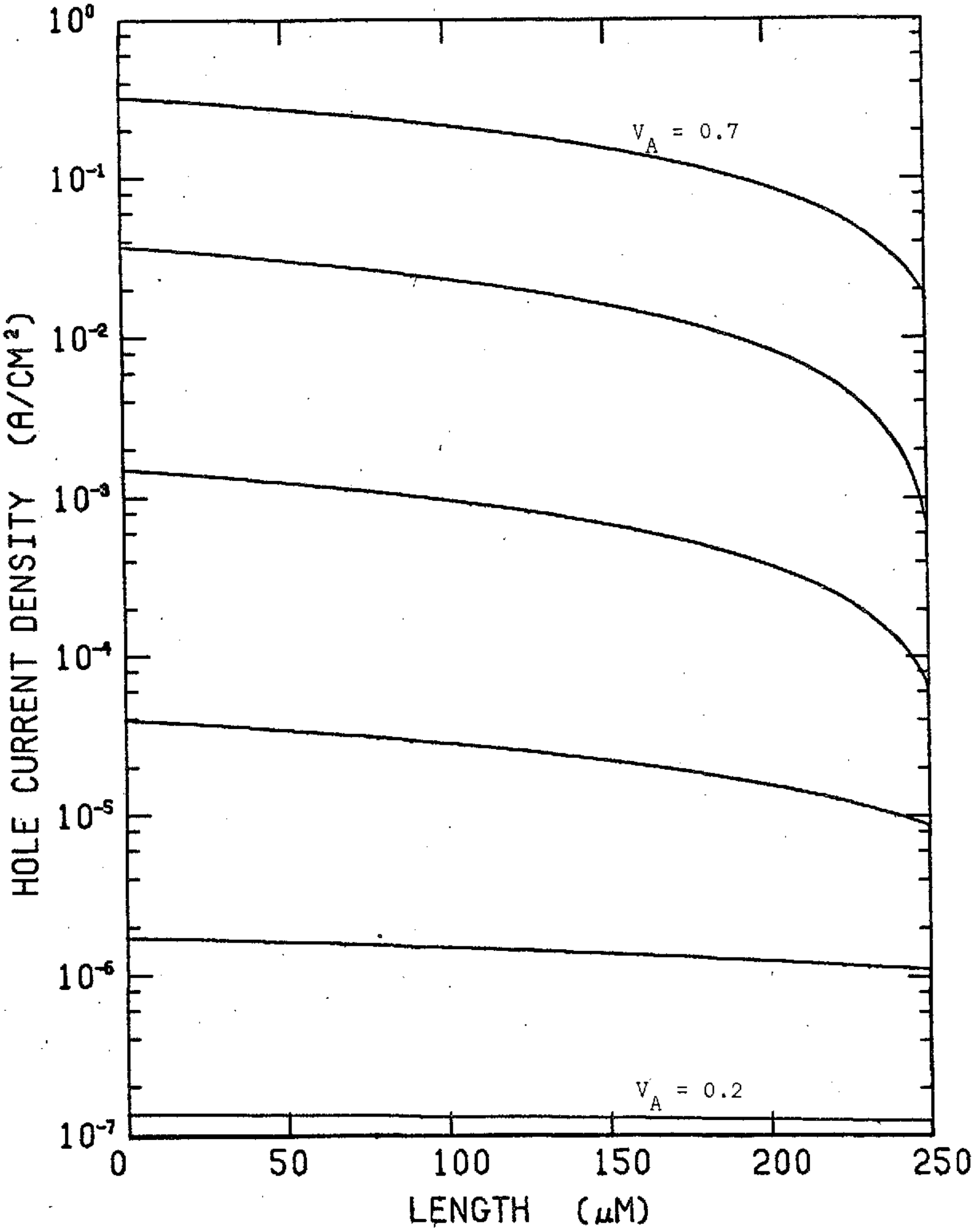

Figure 8a. Hole current density variation throughout the entire device (no illumination).

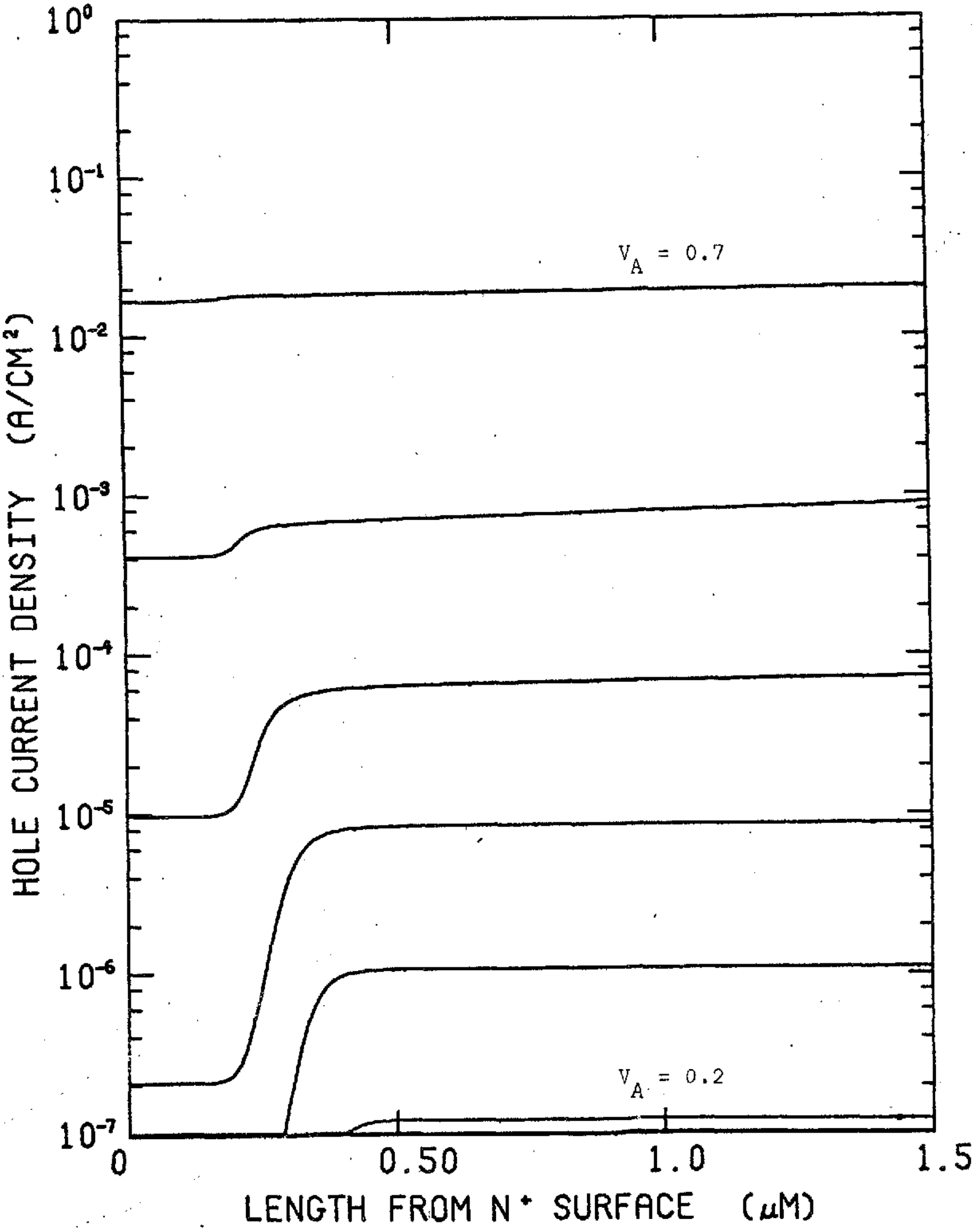

Figure 8b. Hole current density variation about the high-low junction (no illumination).

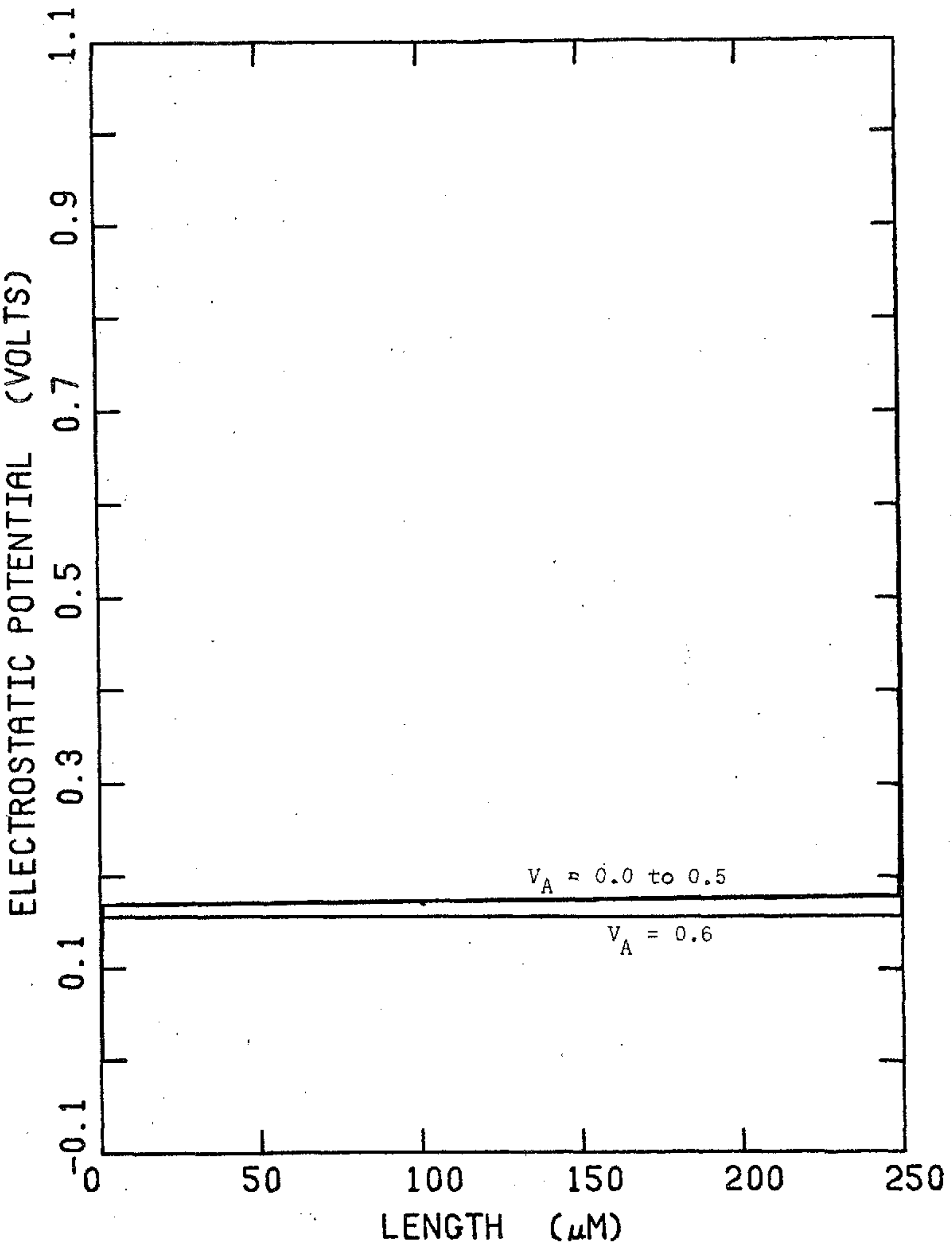

Figure 9a. Electrostatic potential variation throughout the entire device (AM0 illumination).

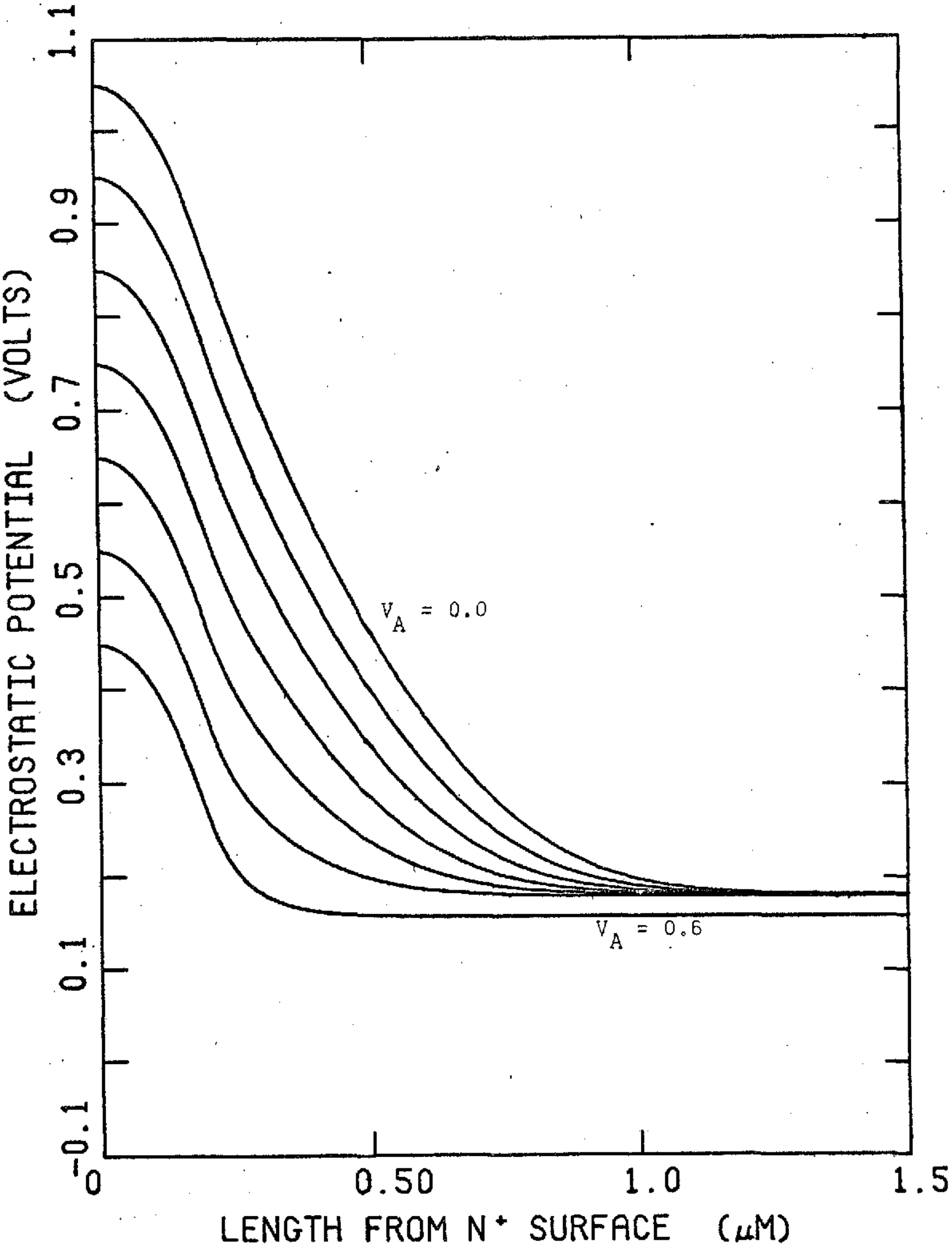

Figure 9b. Electrostatic potential variation about the p-n^+ junction (AM0 illumination).

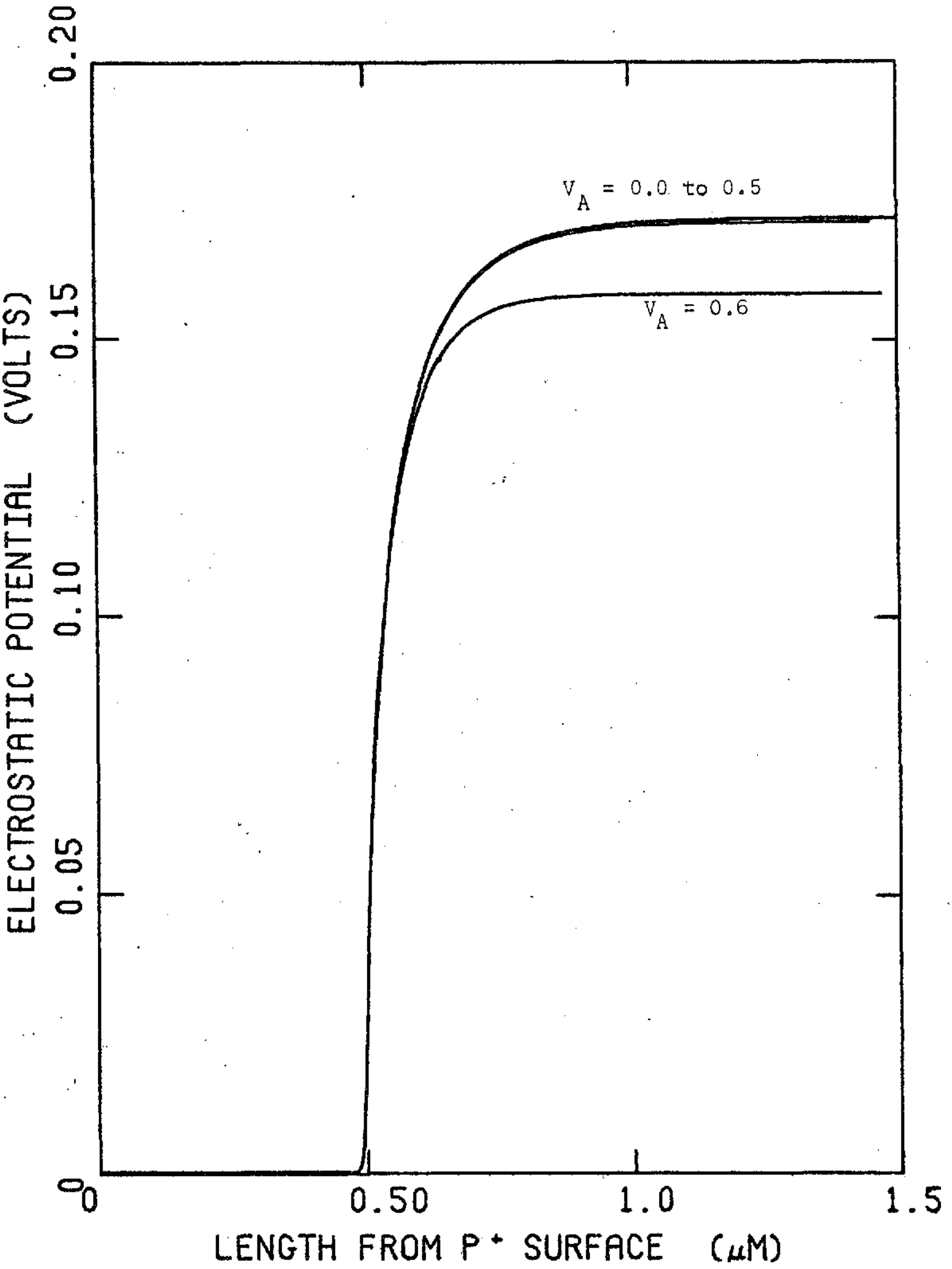

Figure 9c. Electrostatic potential variation about the high-low junction (AM0 illumination).

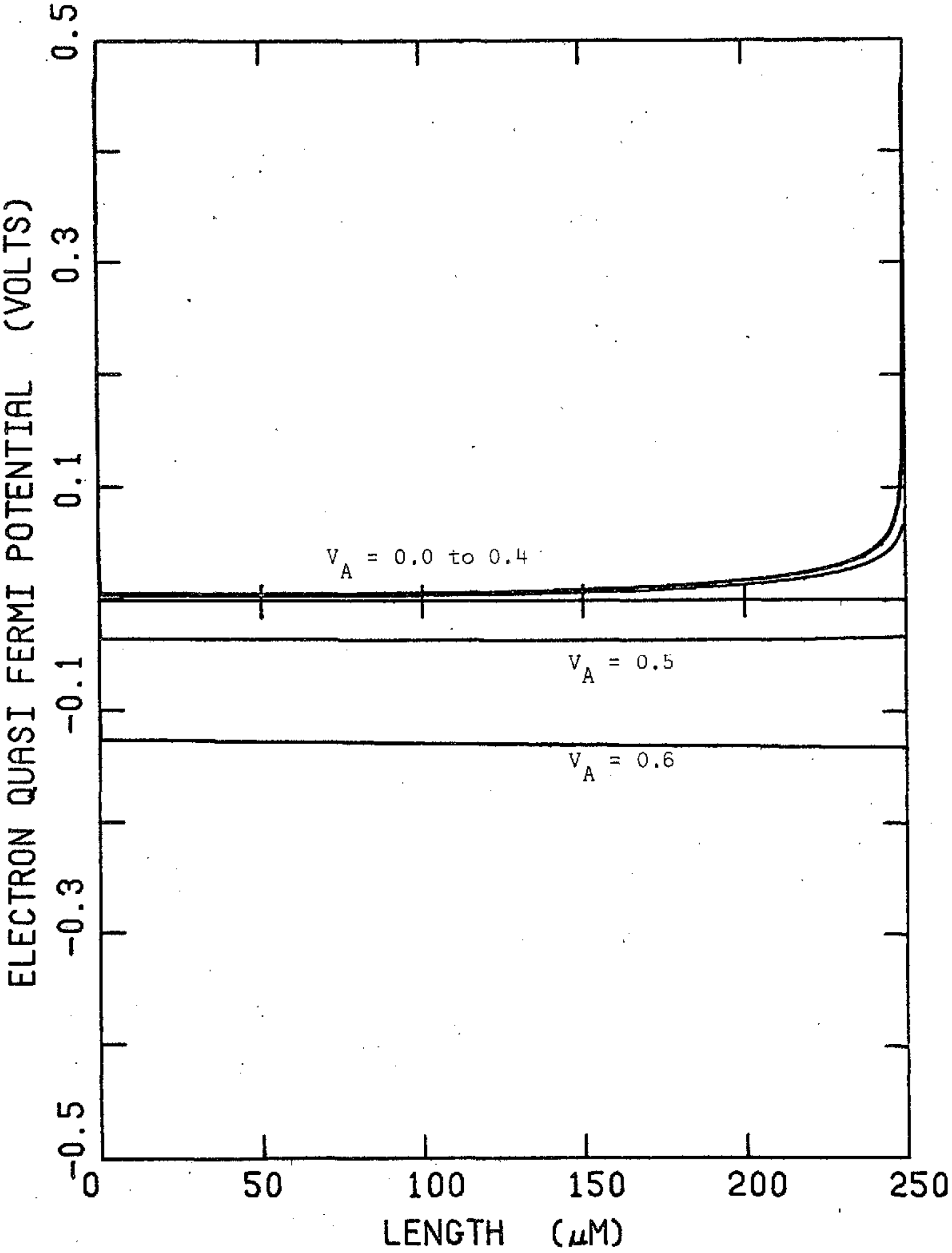

Figure 10a. Electron Quasi-Fermi potential variation throughout the entire device (AM0 illumination).

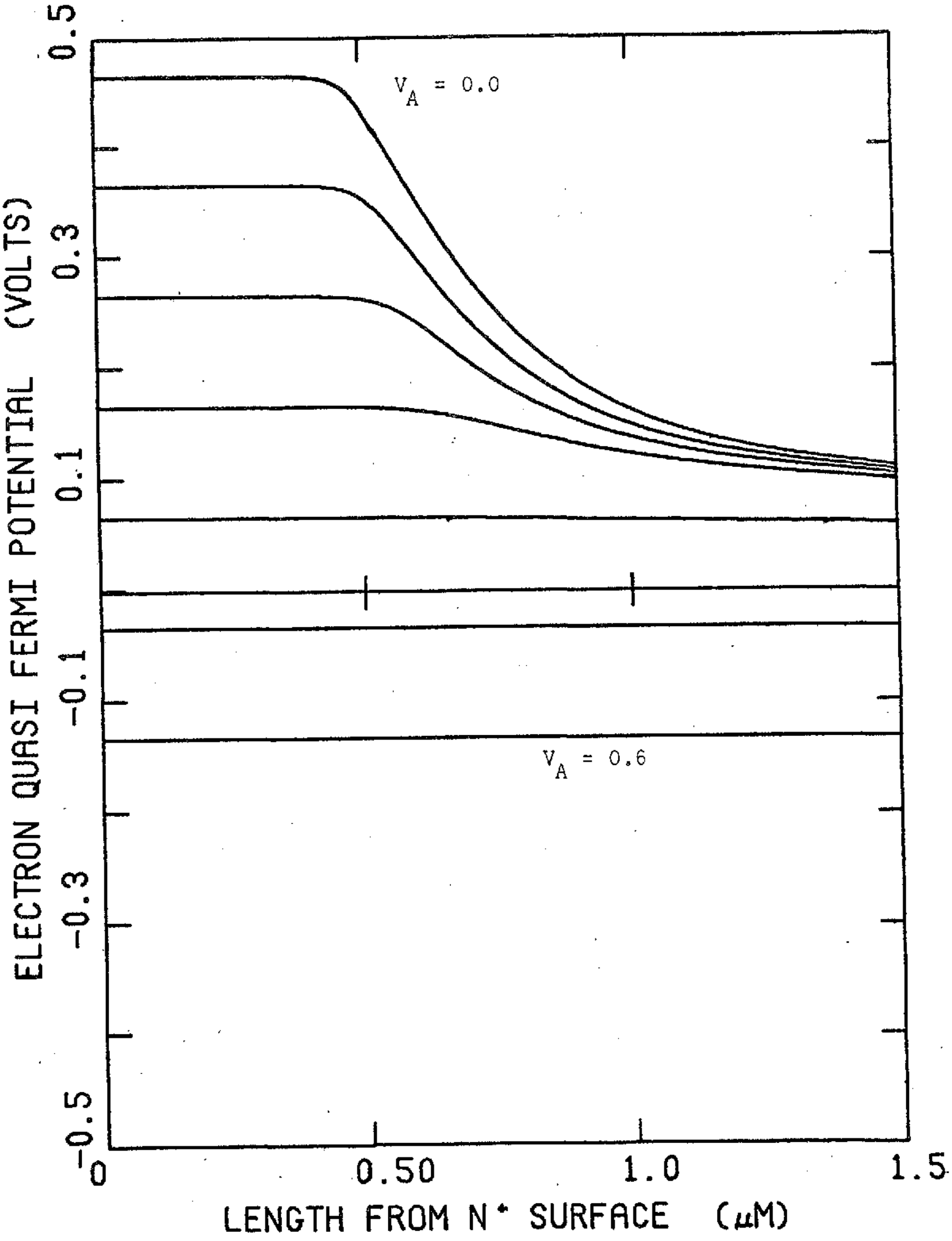

Figure 10b. Electron Quasi-Fermi potential variation about the p-n^+ junction (AM0 illumination).

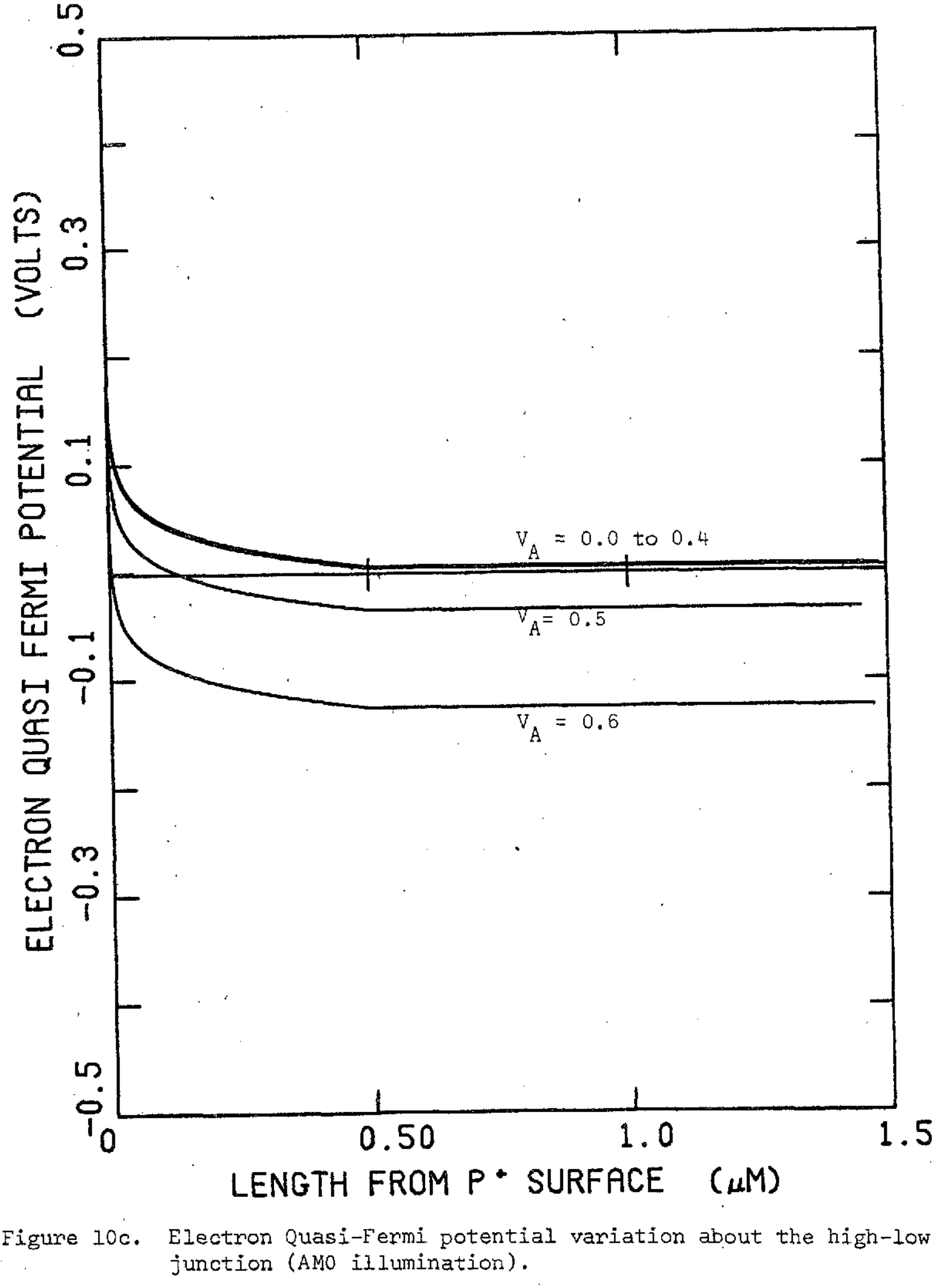

Figure 10c. Electron Quasi-Fermi potential variation about the high-low junction (AM0 illumination).

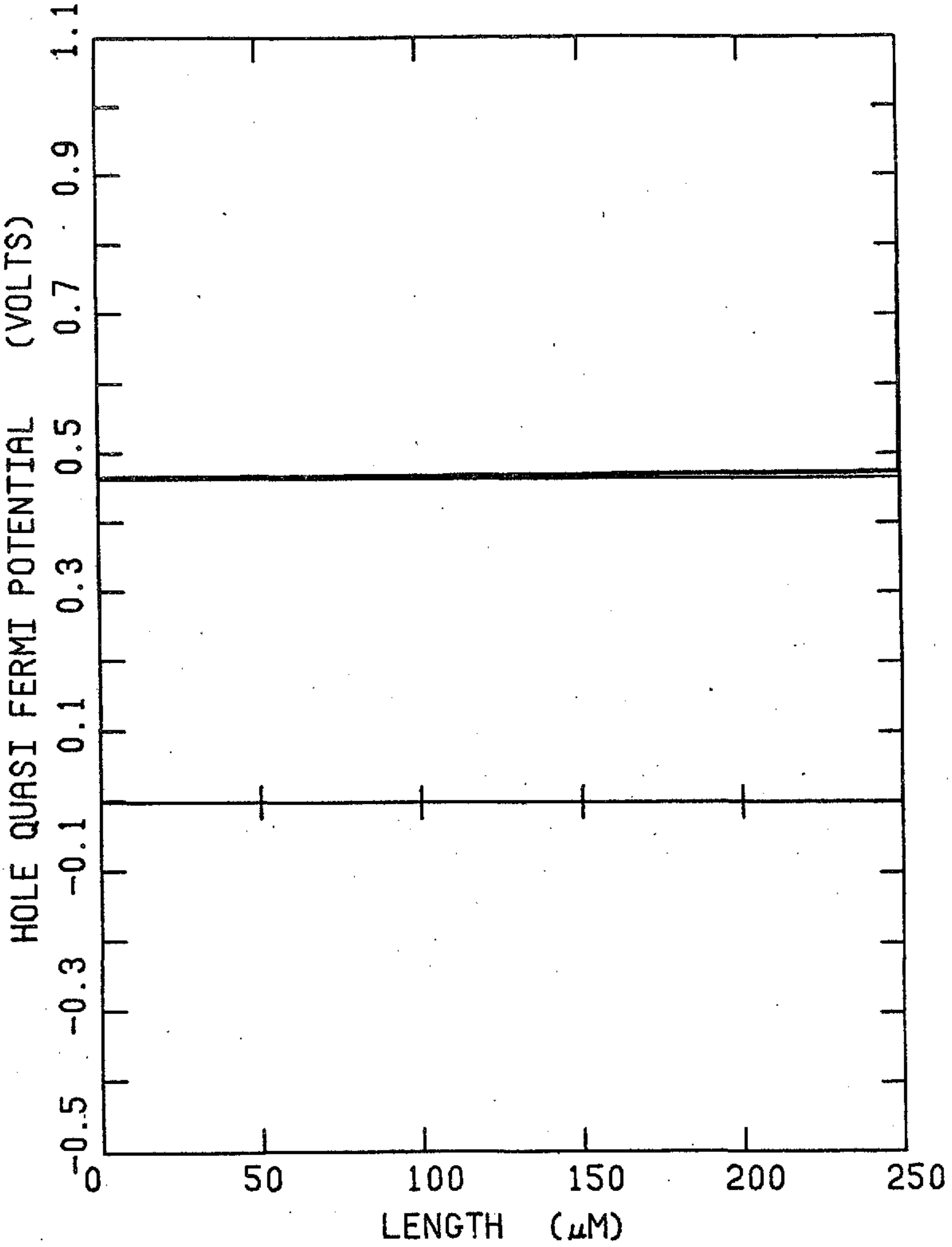

Figure 11a. Hole Quasi-Fermi potential variation throughout the entire device (AM0 illumination).

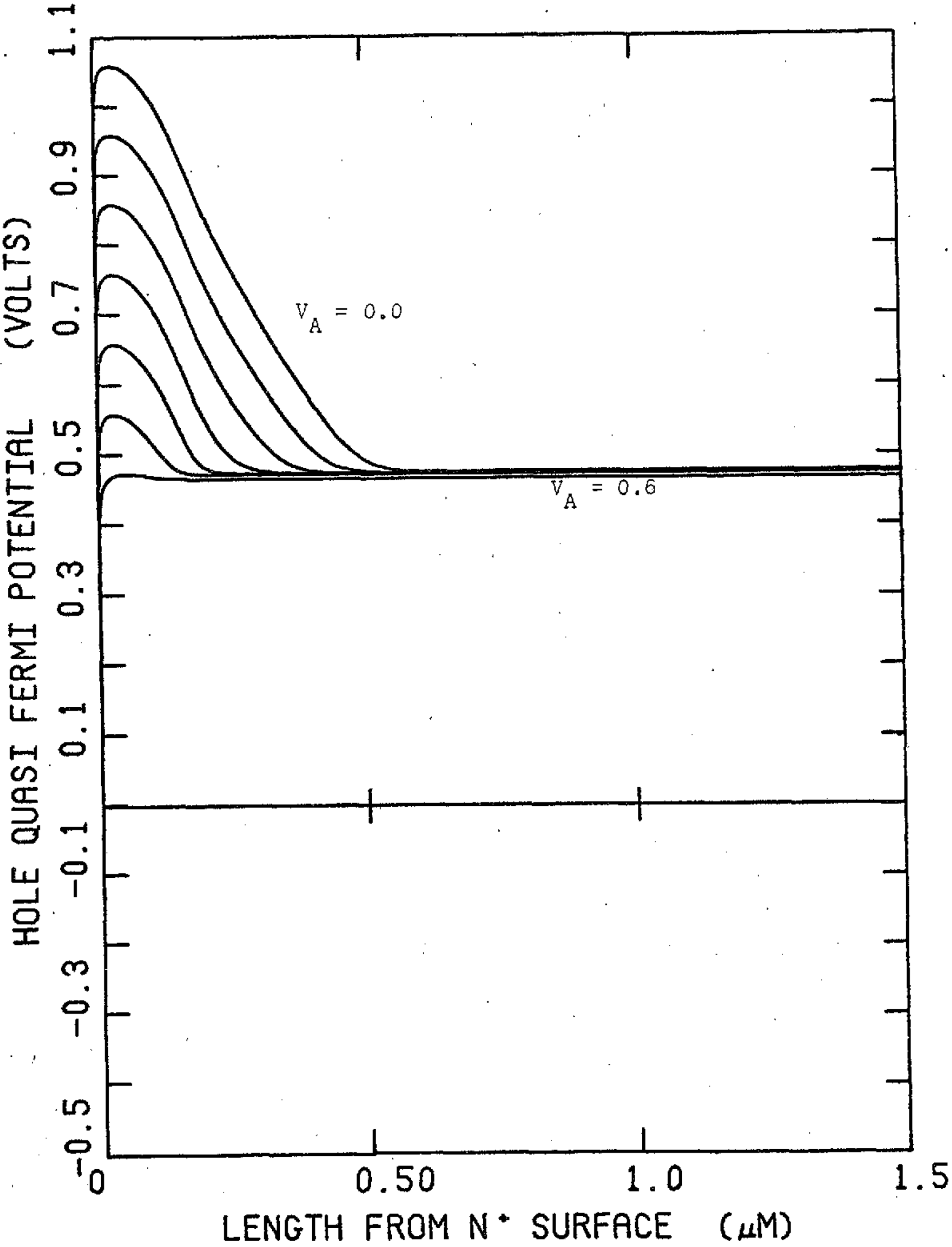

Figure 11b. Hole Quasi-Fermi Potential variation about the p-n$^+$ junction (AM0 illumination).

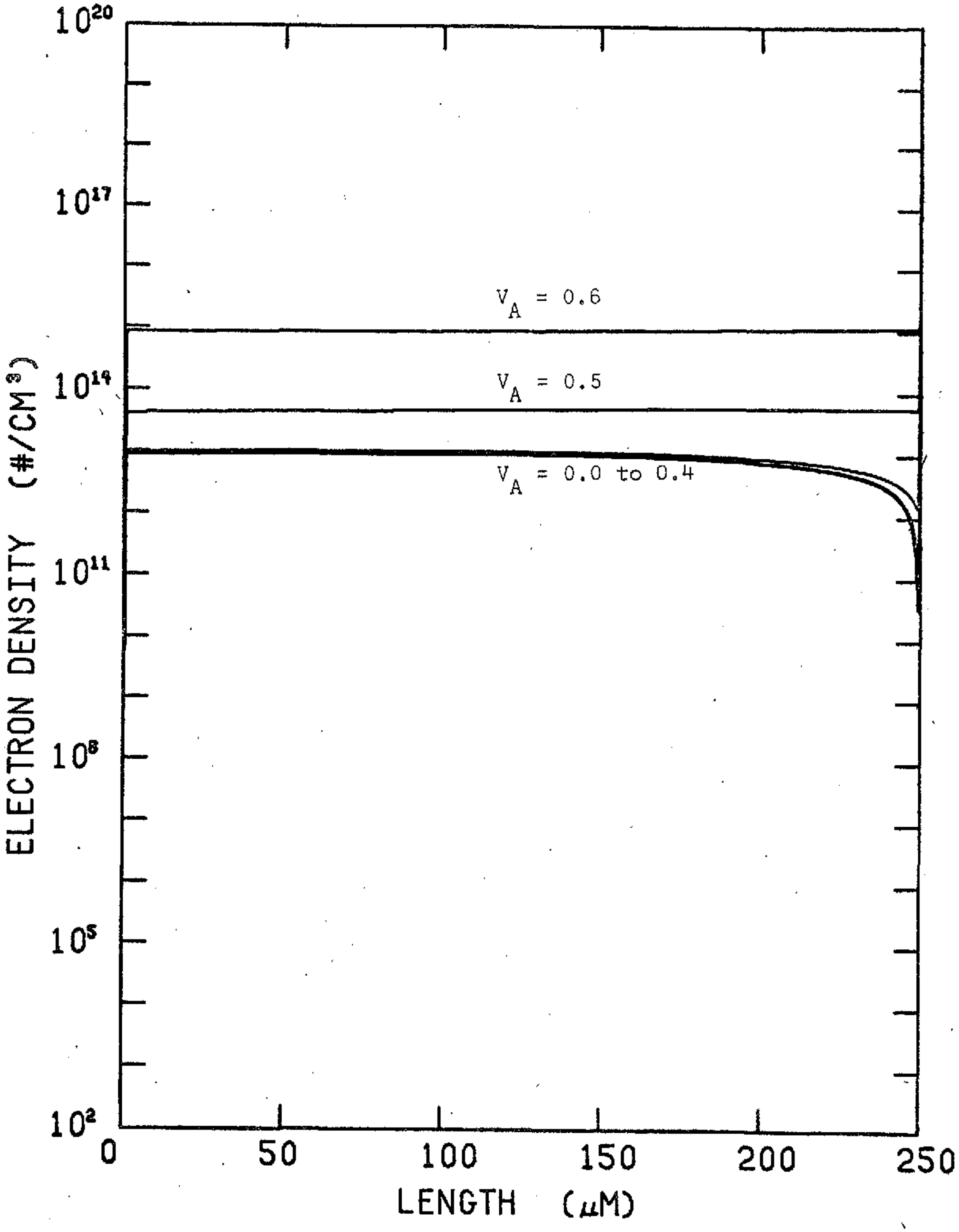

Figure 12a. Electron concentration throughout the entire device (AM0 illumination).

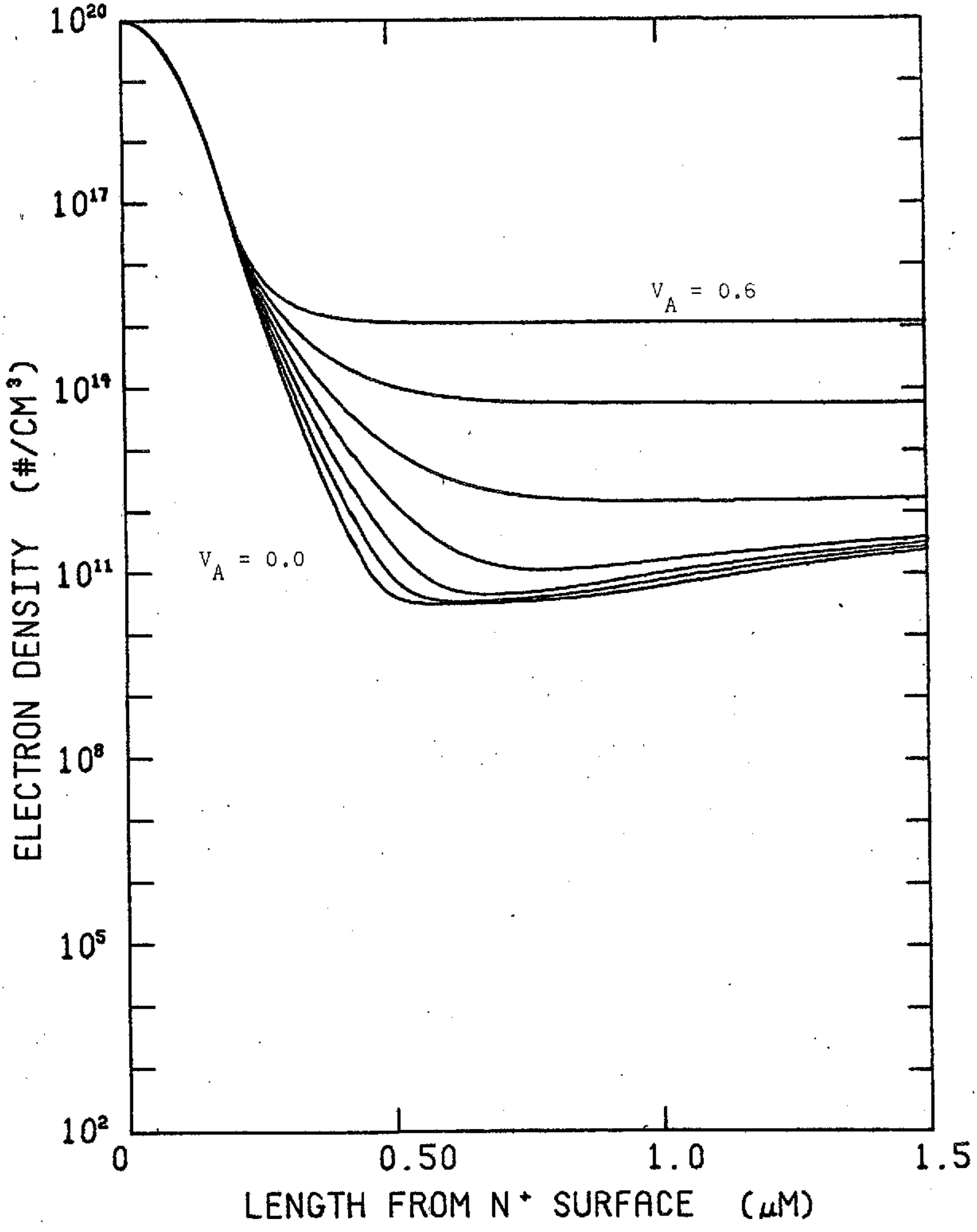

Figure 12b. Electron concentration about the n^+-p junction (AMO illumination).

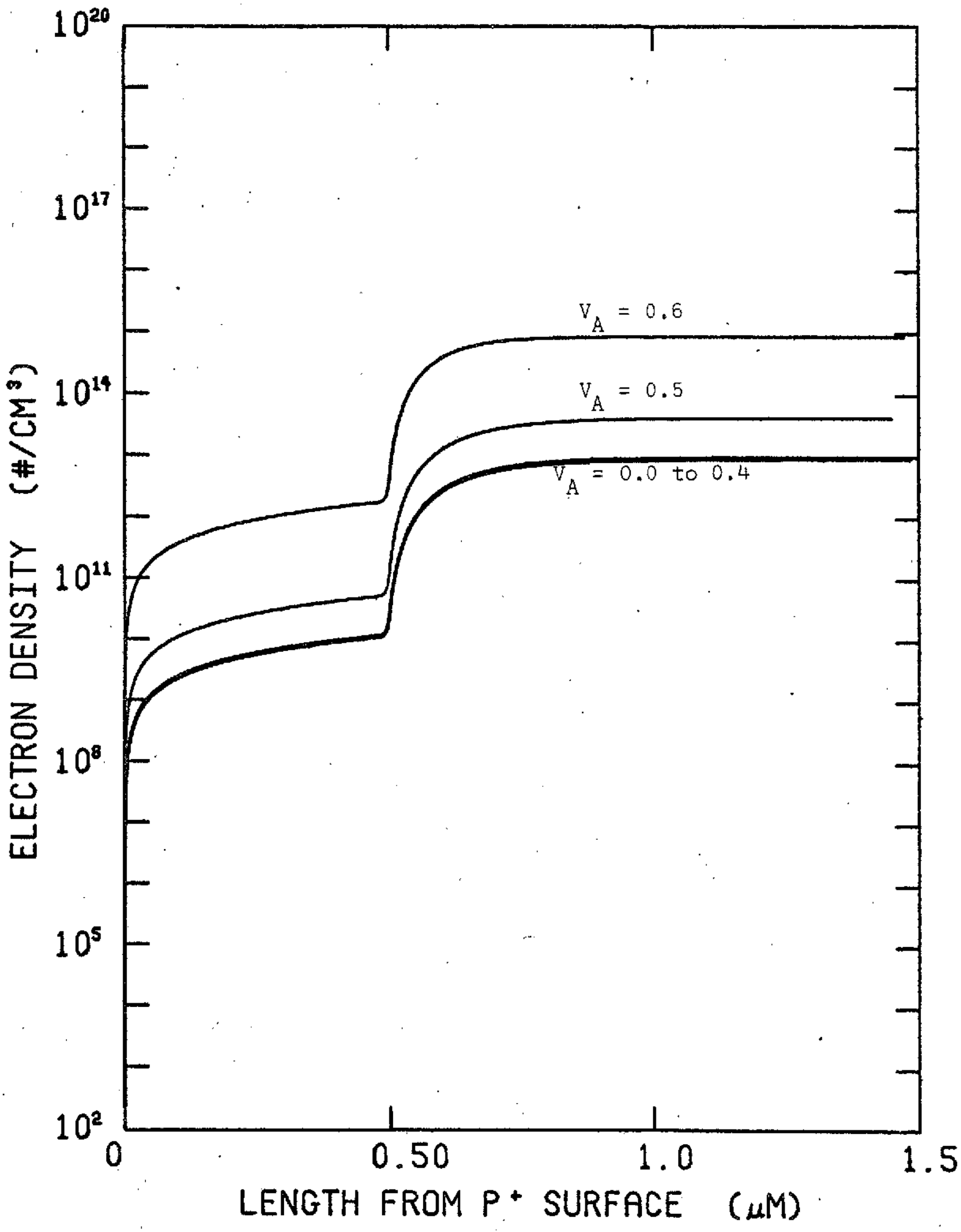

Figure 12c. Electron concentration about the high-low junction (AM0 illumination).

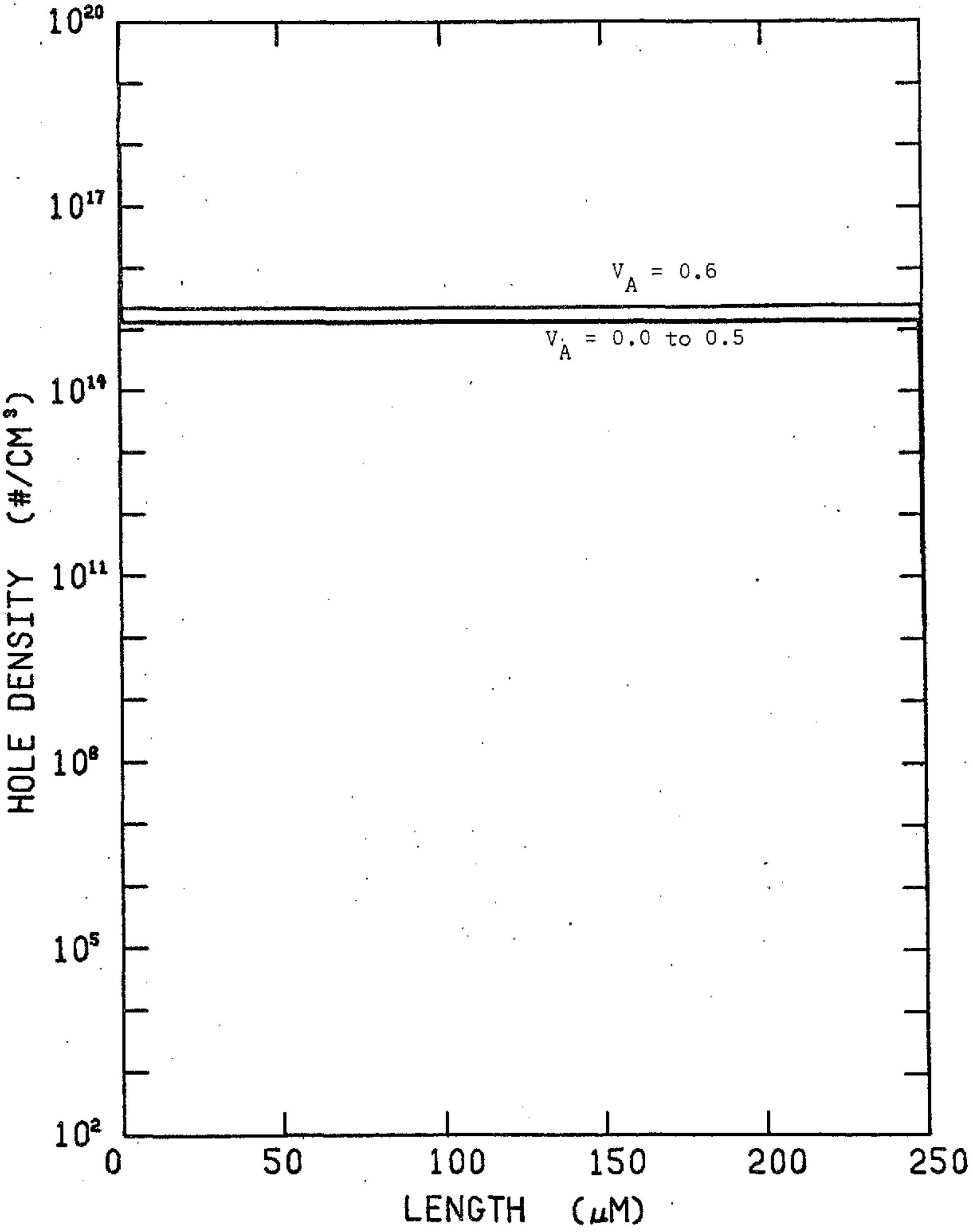

Figure 13a. Hole concentration throughout the entire device (AM0 illumination).

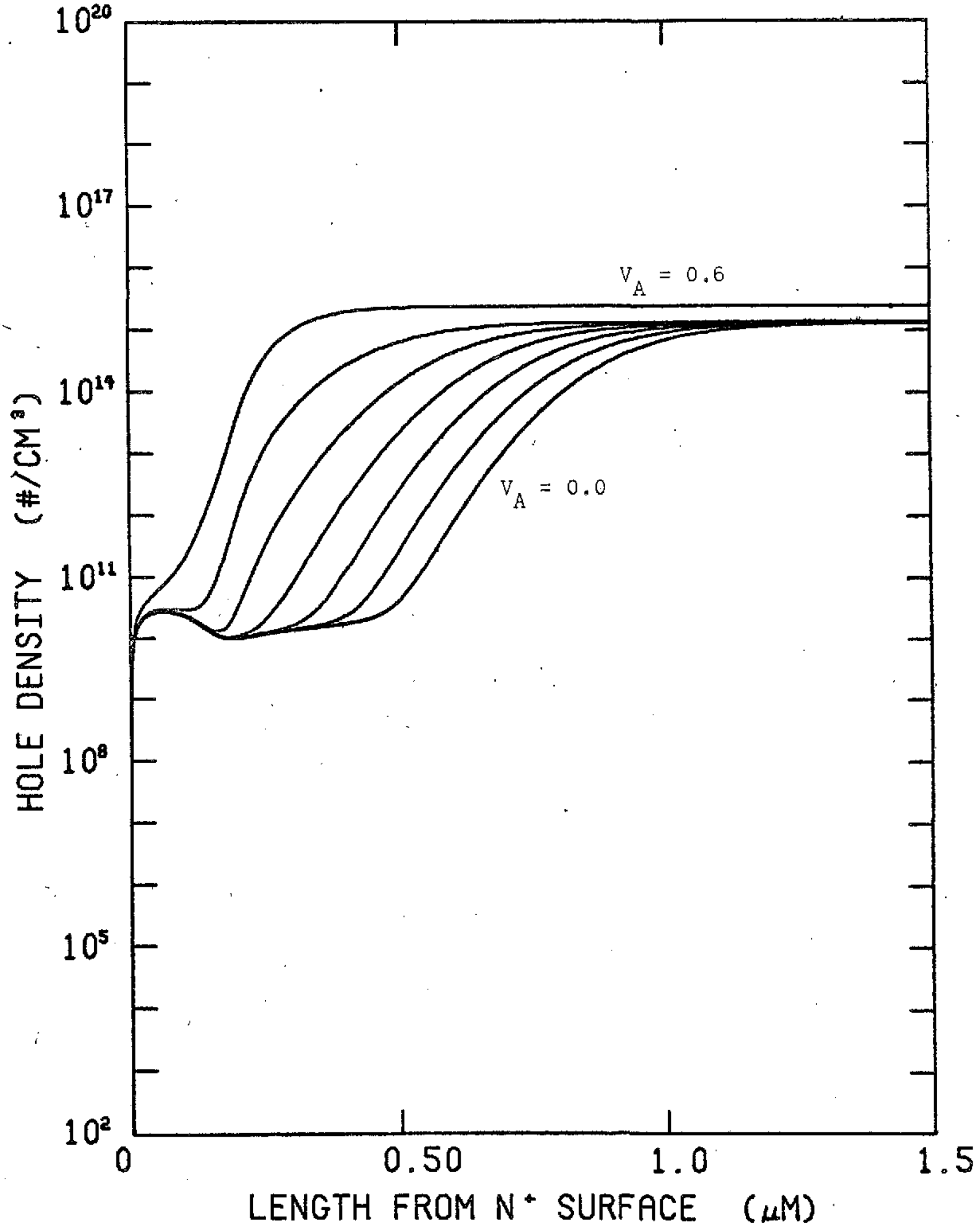

Figure 13b. Hole concentration about the n^+-p junction (AM0 illumination).

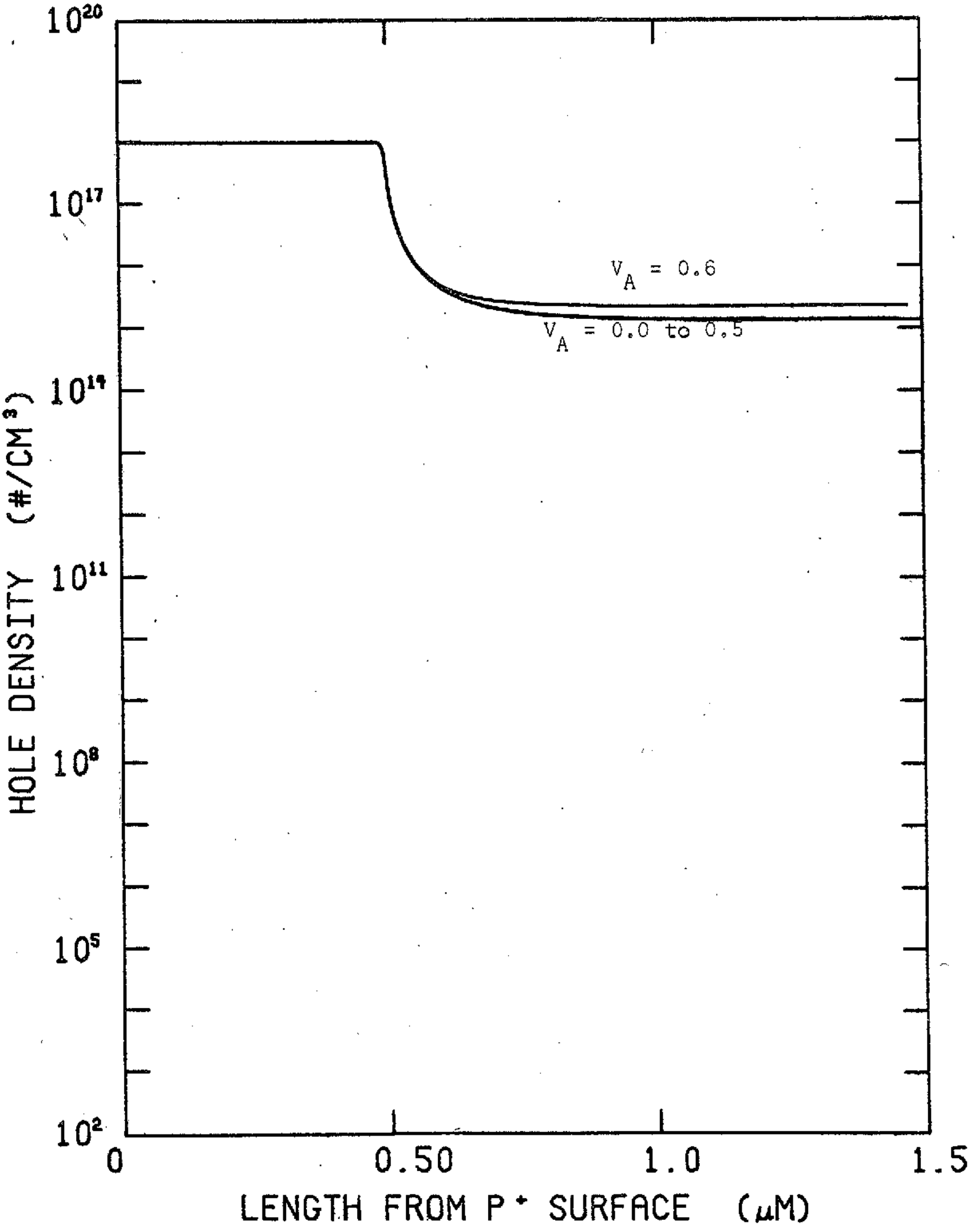

Figure 13c. Hole concentration about the high-low junction (AM0 illumination).

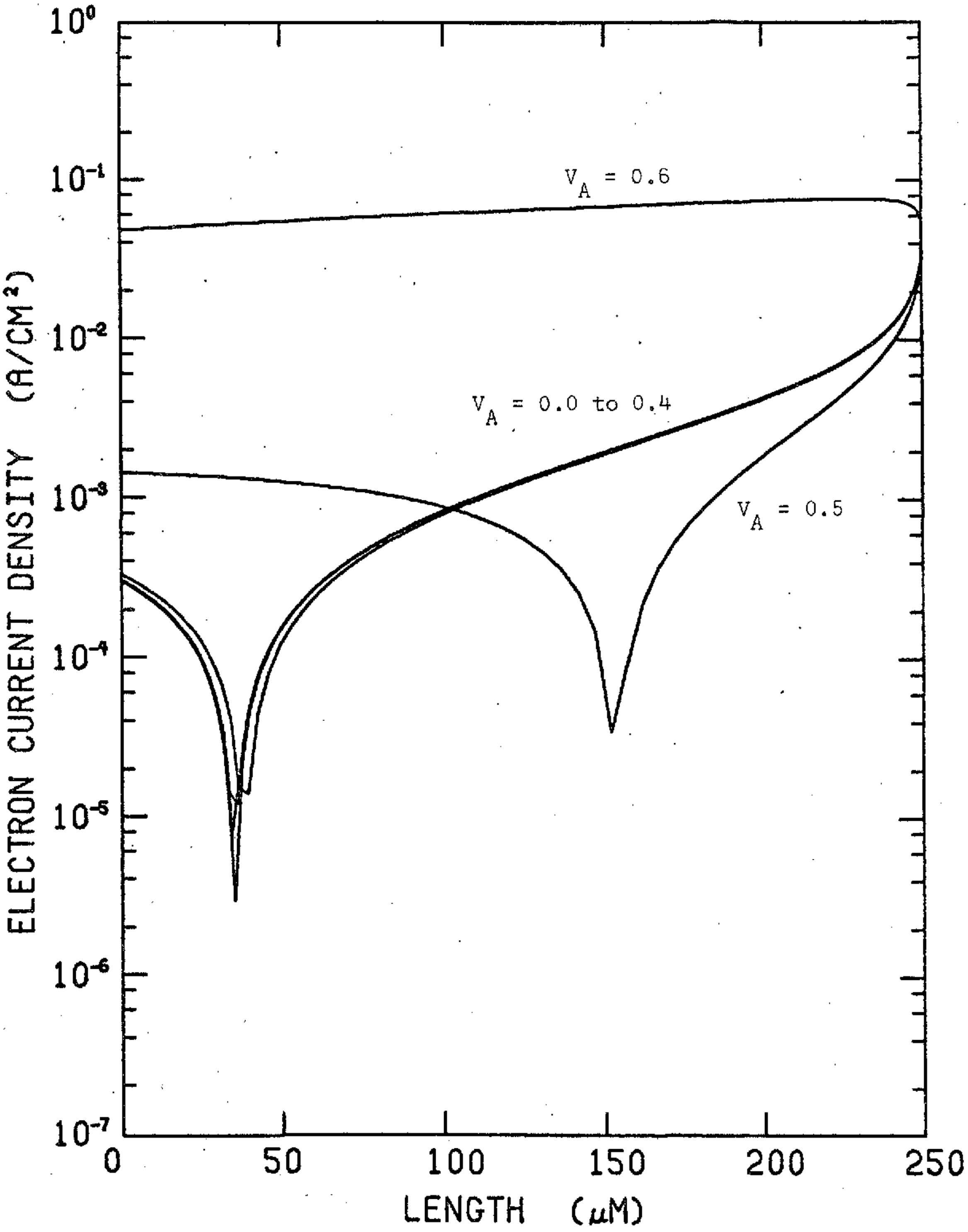

Figure 14a. Electron current density variation throughout the entire device (AM0 illumination).

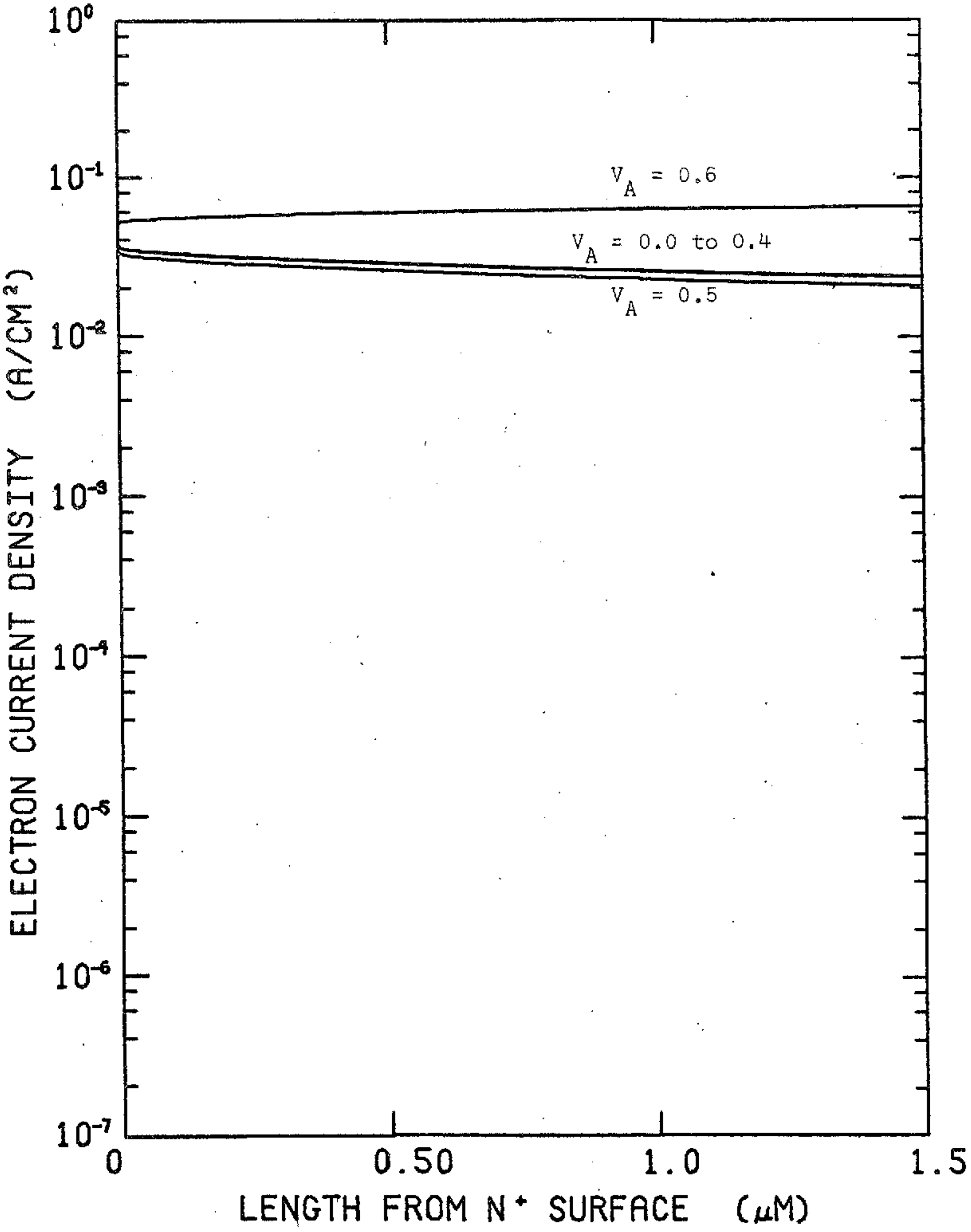

Figure 14b. Electron current density variation about the n^+-p junction (AM0 illumination).

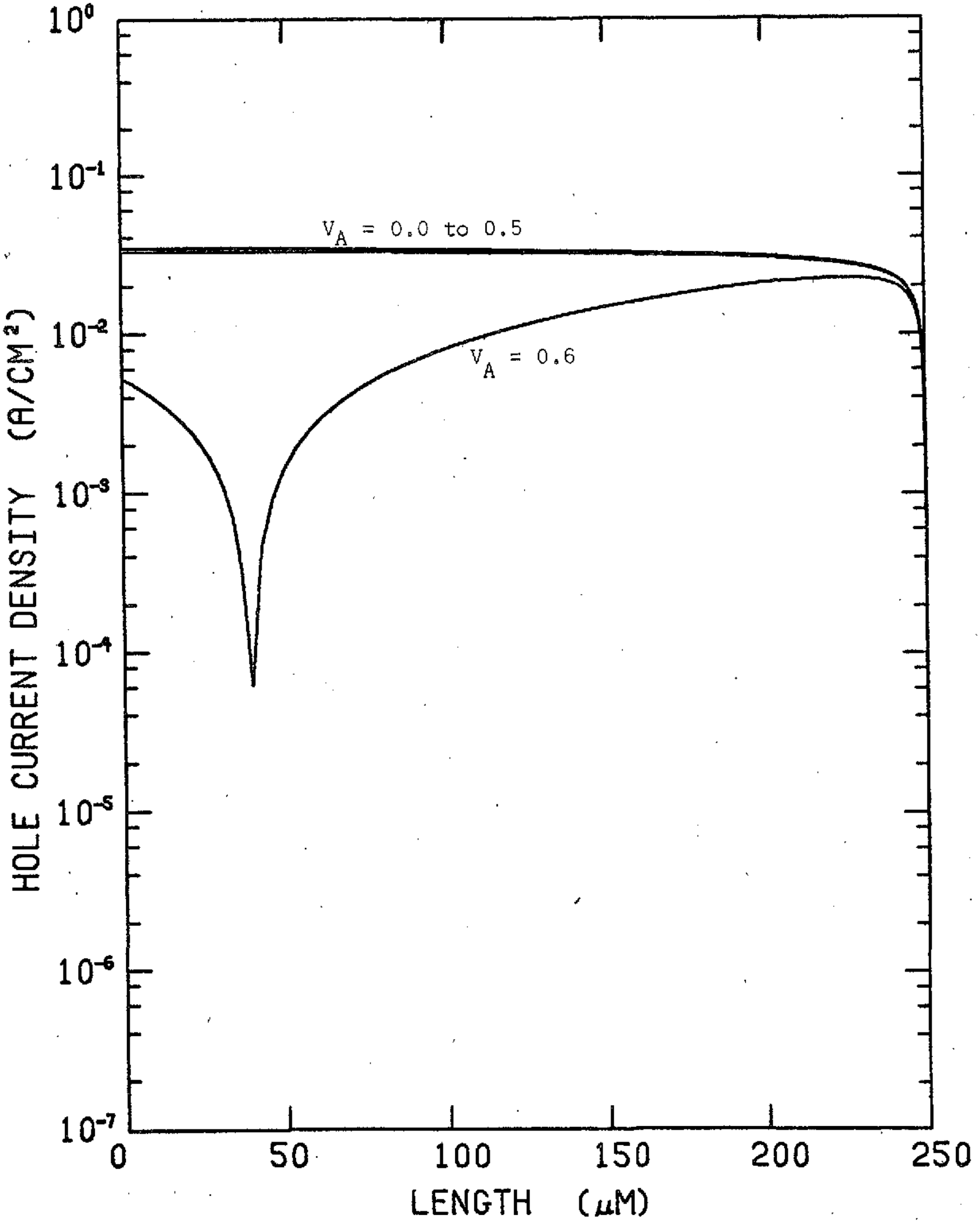

Figure 15a. Hole current density variation throughout the entire device (AM0 illumination).

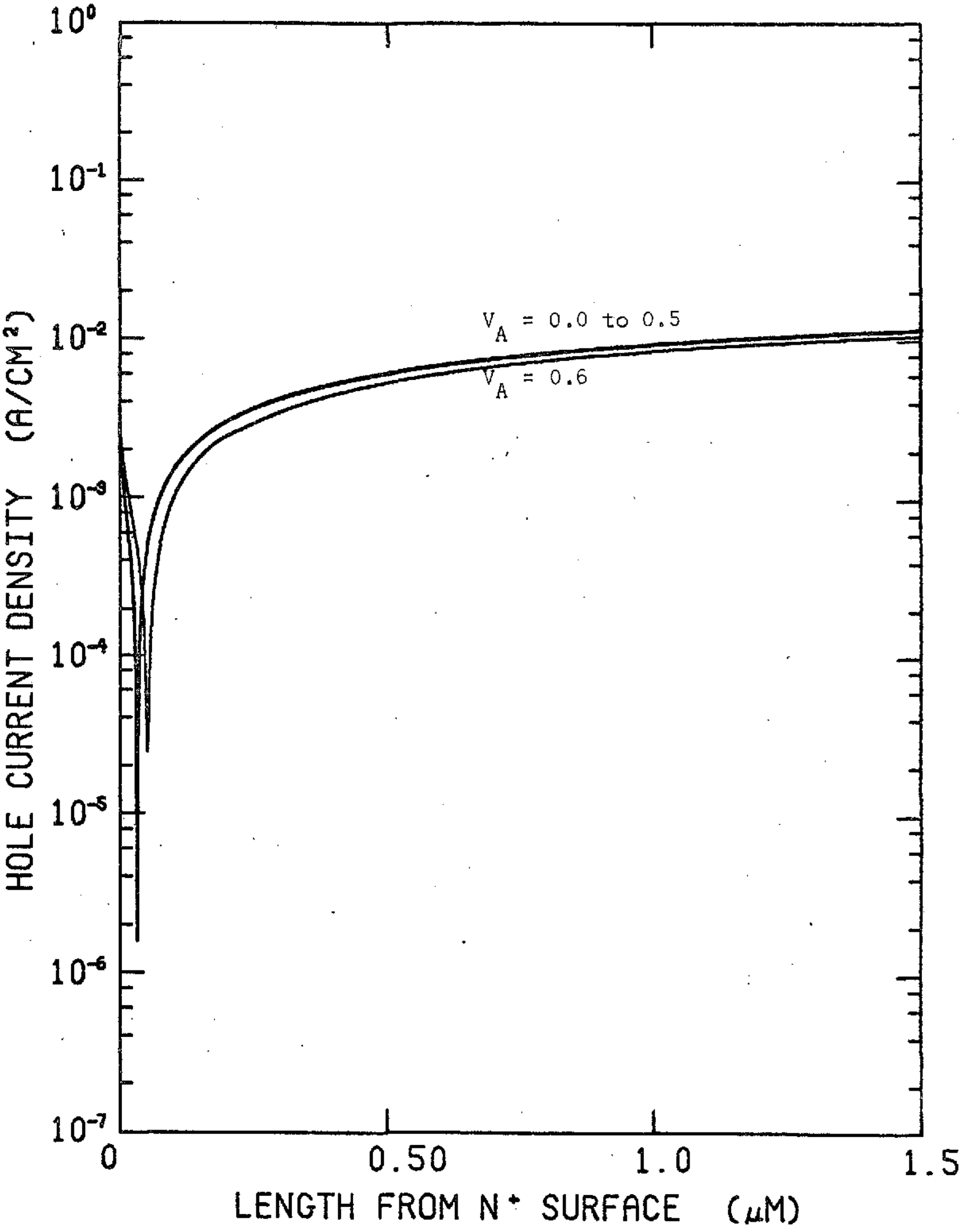

Figure 15b. Hole current density variation about the high-low junction (AM0 illumination).

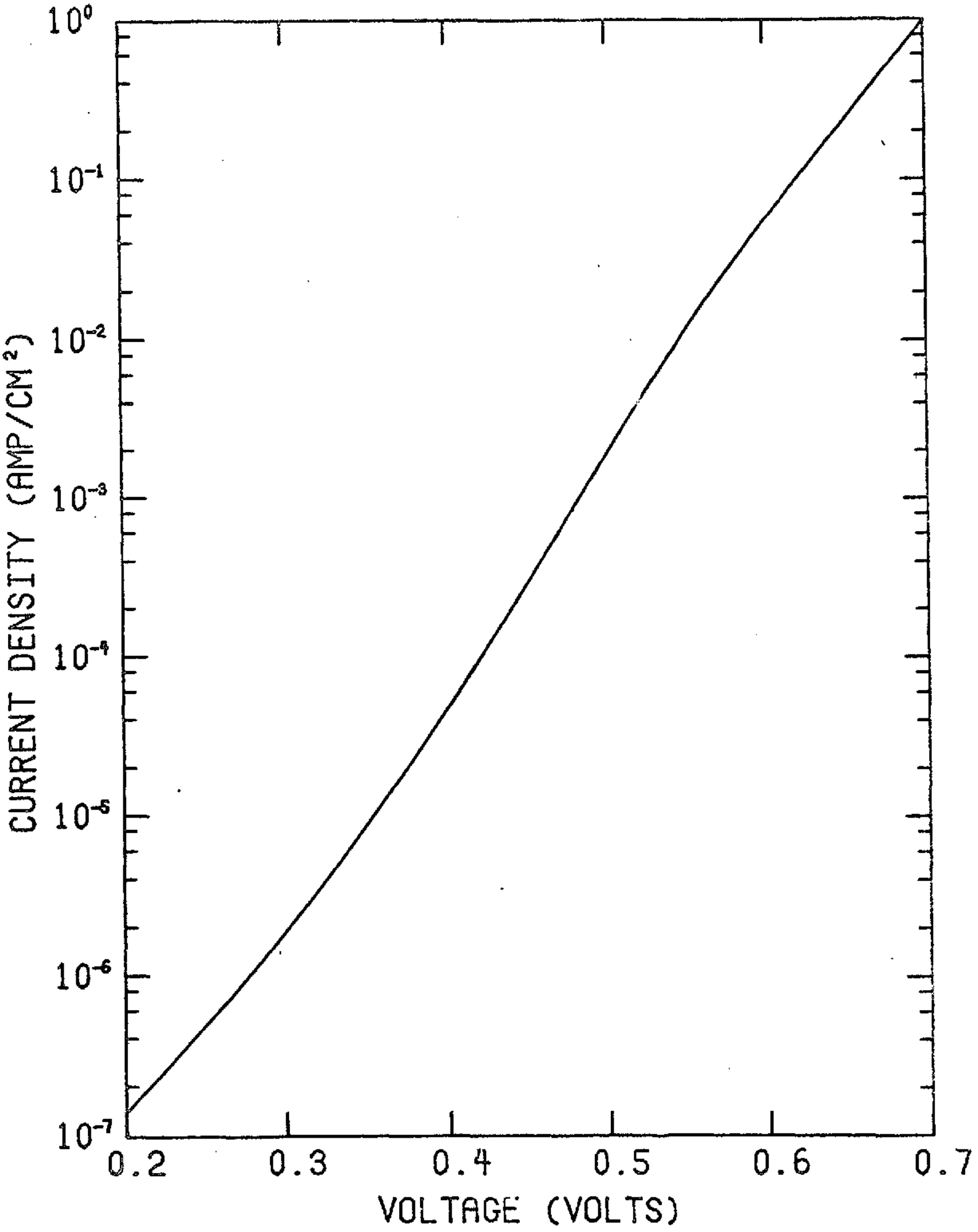

Figure 16. Terminal J-V characteristics of the n^+-p-p^+ solar cell under no illumination.

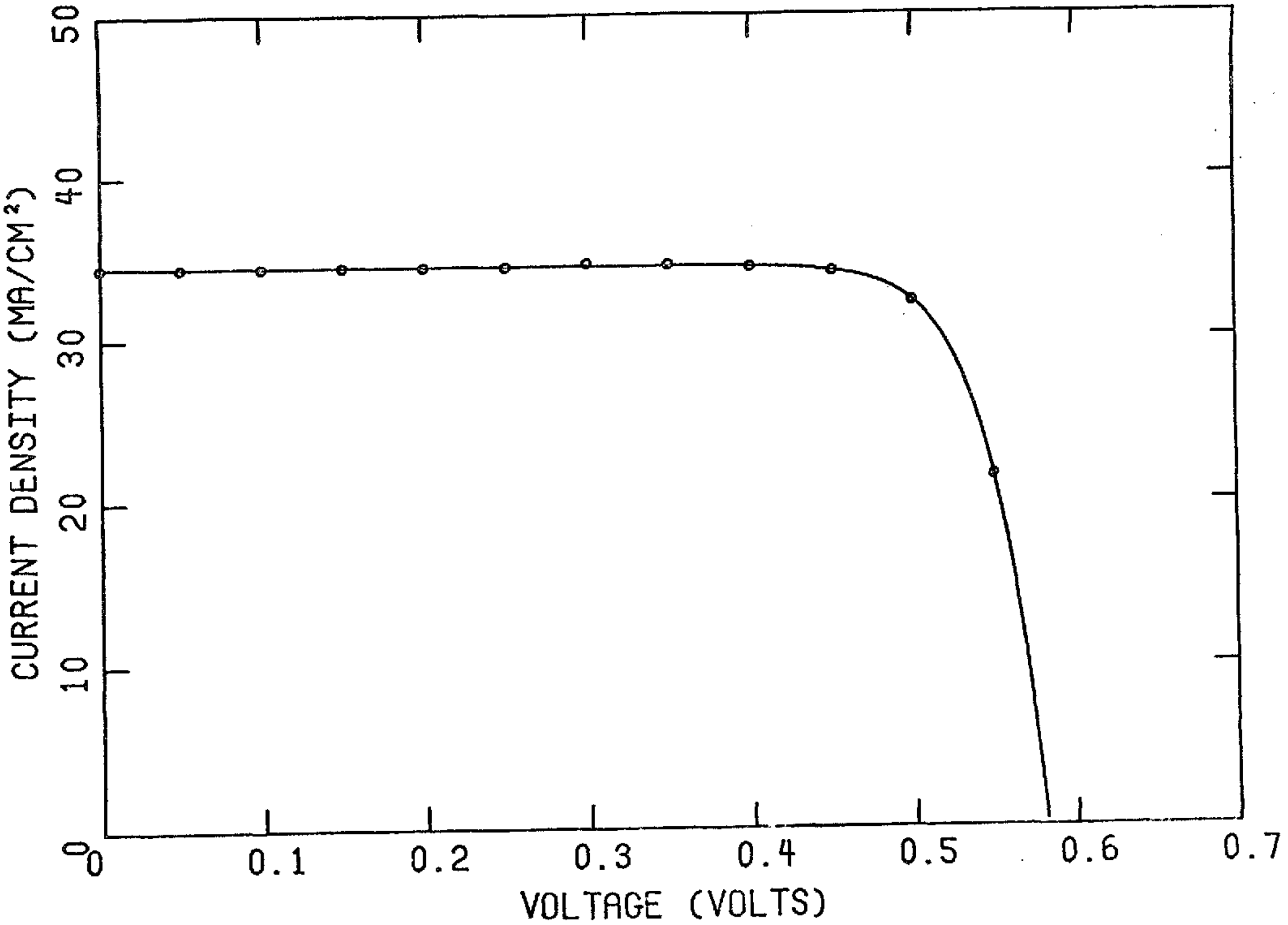

Figure 17. Terminal J-V characteristics of the n^+-p-p^+ solar cell under AM0 illumination.

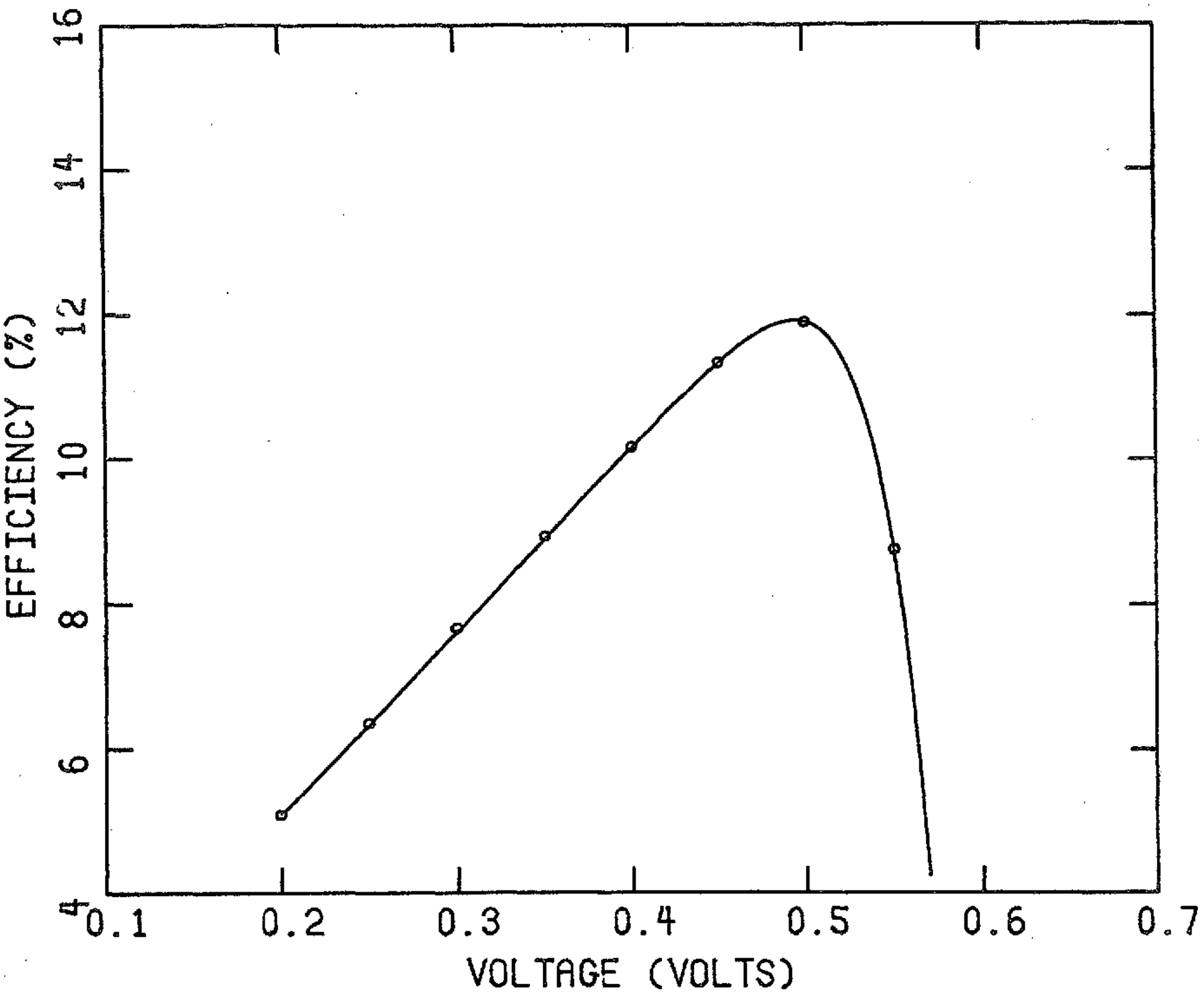

Figure 18. Efficiency characteristics of the n^+-p-p^+ solar cell (AMO illumination).

III. EFFECT OF HIGH-LOW JUNCTION ON SOLAR CELL PROPERTIES AND EFFICIENCY

In addition to developing a solar cell analysis program, one of the major efforts during this year's research has been the attempt to better understand the role of a p^+-p or high-low junction at the back surface of a solar cell. In general, the computer calculations have shown that the first order models for high-low junction behavior are very closely satisfied by the junctions studied in this work. A comparison of the numerical results with first order high-low junction equations is given in Appendix C.

The high-low junction has been found to act at low voltages primarily as a minority carrier reflecting back contact giving a small effective surface recombination velocity at the boundary of the p-p^+ junction. The curves of electron concentration in Figure 5 show the large change in electron concentration occurring at the high-low junction.

Several calculations have been made to explore the effect of a back surface high-low junction on overall efficiency. Figures 19, 20 and 21 show one series of modifications of the back p^+ contact. Curves are shown for three devices: (a) ohmic back contact, (b) 0.5 μM thick back p^+ region and (c) 5 μM thick back p^+ region. Other parameters for the devices are as given in Table I. Figure 19 shows a very significant decrease in the current density at a constant voltage for the devices with p^+ back contacts. The decrease in current is due to the decreased flow of injected electrons to the back ohmic contact. The 5 μM p^+ device shows only a slight improvement over the 0.5 μM device.

The 5 μM and 0.5 μM devices have back boundary effective surface recombination velocities of 1.1 cm/sec and 204 cm/sec respectively. The value for the 0.5 μM device is already so low that it acts almost as an ideal minority carrier reflecting back contact.

The current density vs voltage characteristics for the three devices are shown in Figure 20. The ohmic back contact device is seen to have a reduced short circuit current and a reduced open circuit voltage. The reduced short circuit current arises from the loss of optically generated carriers at the back contact. The reduced open circuit voltage arises from the combined effects of a smaller photocurrent and a larger forward diode current as indicated in Figure 19. The efficiency curves of Figure 21 illustrate the improved efficiency of the high-low junction solar cell. There is little change in peak efficiency between the 0.5 μM and 5 μM cells.

Calculations similar to those described above were also made for 250 μM thick devices with 10 μsec minority carrier lifetimes in the p-region. These calculations showed a considerably smaller difference in peak efficiency between the high-low junction cells and ohmic back contact cells. For 10 μsec devices, the efficiency of the high-low junction device was only about 0.5% above that of the ohmic contact device. These results are to be expected on theoretical grounds. For a 10 μsec lifetime, the diffusion length in the p-layer is about 180 μM which is less than the 250 μM thickness. On the other hand for a lifetime of 100 μsec, the diffusion length is about 580 μM or slightly more than twice the cell thickness. As the cell thickness becomes large compared with a diffusion length, there can be little interaction between the minority carriers and the high-low junction and the behavior of the p^+ device must approach that of the ohmic back contact device for small diffusion lengths.

The voltage change across a high-low junction based upon simple theoretical arguments is related to the carrier densities from Eq. (2) as

$$V_{hl} = \frac{kT}{q} \ln \left[\frac{N_{p^+}}{N_p}/(1 + n_p/N_p)\right] \quad (4)$$

$$= V_{hlo} - \frac{kT}{q} \ln (1 + n_p/N_p), \quad (5)$$

where V_{hlo} is the equilibrium high-low junction potential. Equation 5 predicts a reduction in the high-low junction voltage due to the electron concentration in the p-region, n_p. Limiting cases of Eq. (5) are

$$V_{hl} \approx \begin{cases} V_{hlo} - \frac{kT}{q} \frac{n_p}{N_p} & n_p << N_p \\ V_{hlo} - \frac{kT}{q} \ln \left(\frac{n_p}{N_p}\right) & n_p >> N_p \end{cases} \quad (6)$$

Significant changes in high-low junction potential require that n_p be on the order of N_p. These simple relationships have been found to be satisfied very closely in the computer calculations. The detailed device calculations discussed in Section II show the high-low junction potential remaining essentially constant until high injection ($n_p > N_p$) occurs in the p-region.

In summary, the computer calculations have verified and been in good agreement with first order models for high-low junction behavior in the presence of excess minority carriers. Below high injection in the p-region, the high-low junction acts basically as a minority carrier reflecting boundary. Above high injection a part of the terminal voltage appears across the high-low junction. For the 100 μsec lifetime, 250 μM thick cells studied, the open circuit voltage condition occurs very near the high injection condition. For solar cells with longer lifetimes or higher p-type resistivities the importance of the high-low junction is greatly enhanced. Such a condition is discussed in the next section.

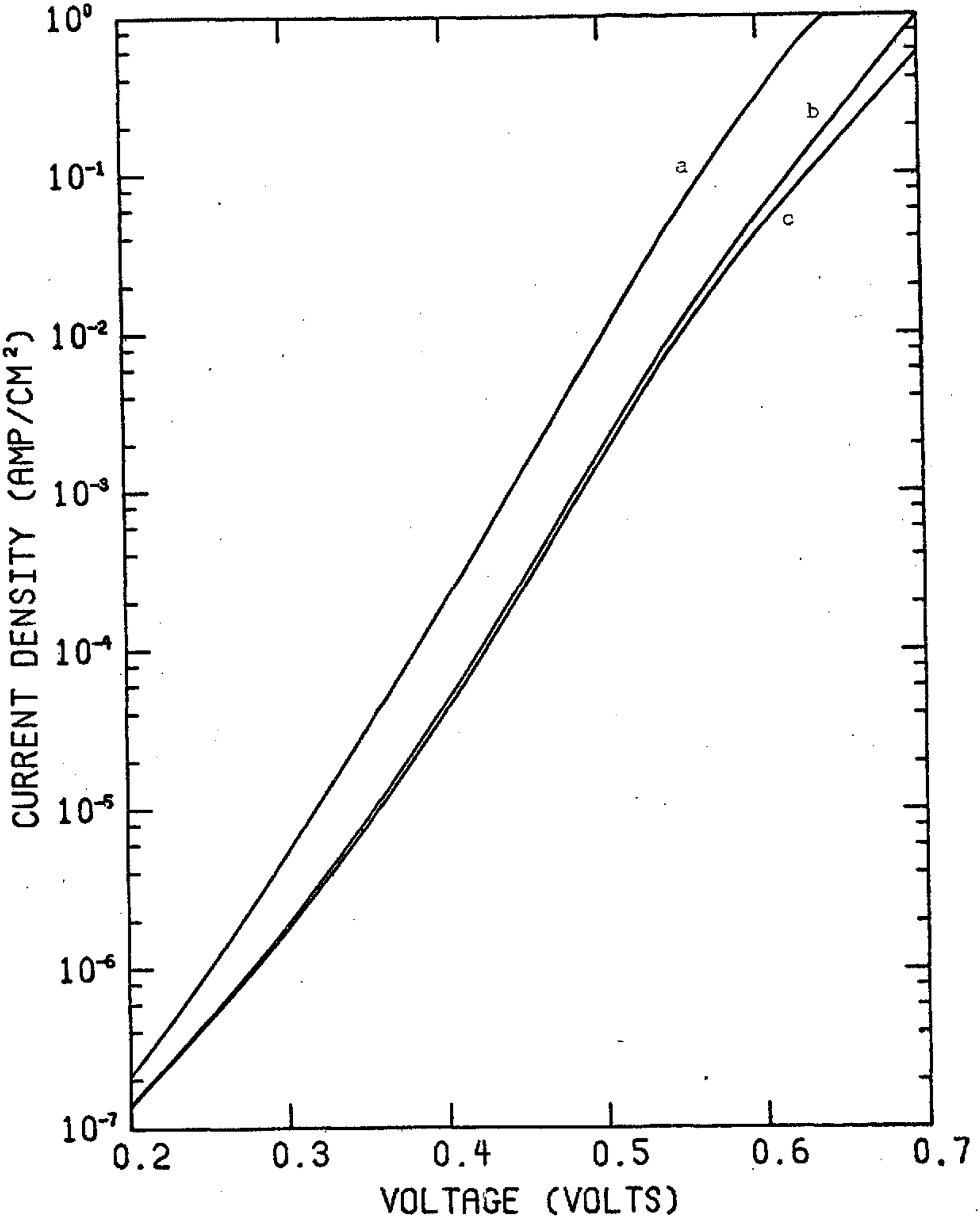

Figure 19. Terminal J-V characteristics for (a) n^+-p with ohmic back contact, (b) n^+-p-p^+ with 0.5 µM p^+ region, and (c) n^+-p-p^+ with 5 µM p^+ region (no illumination).

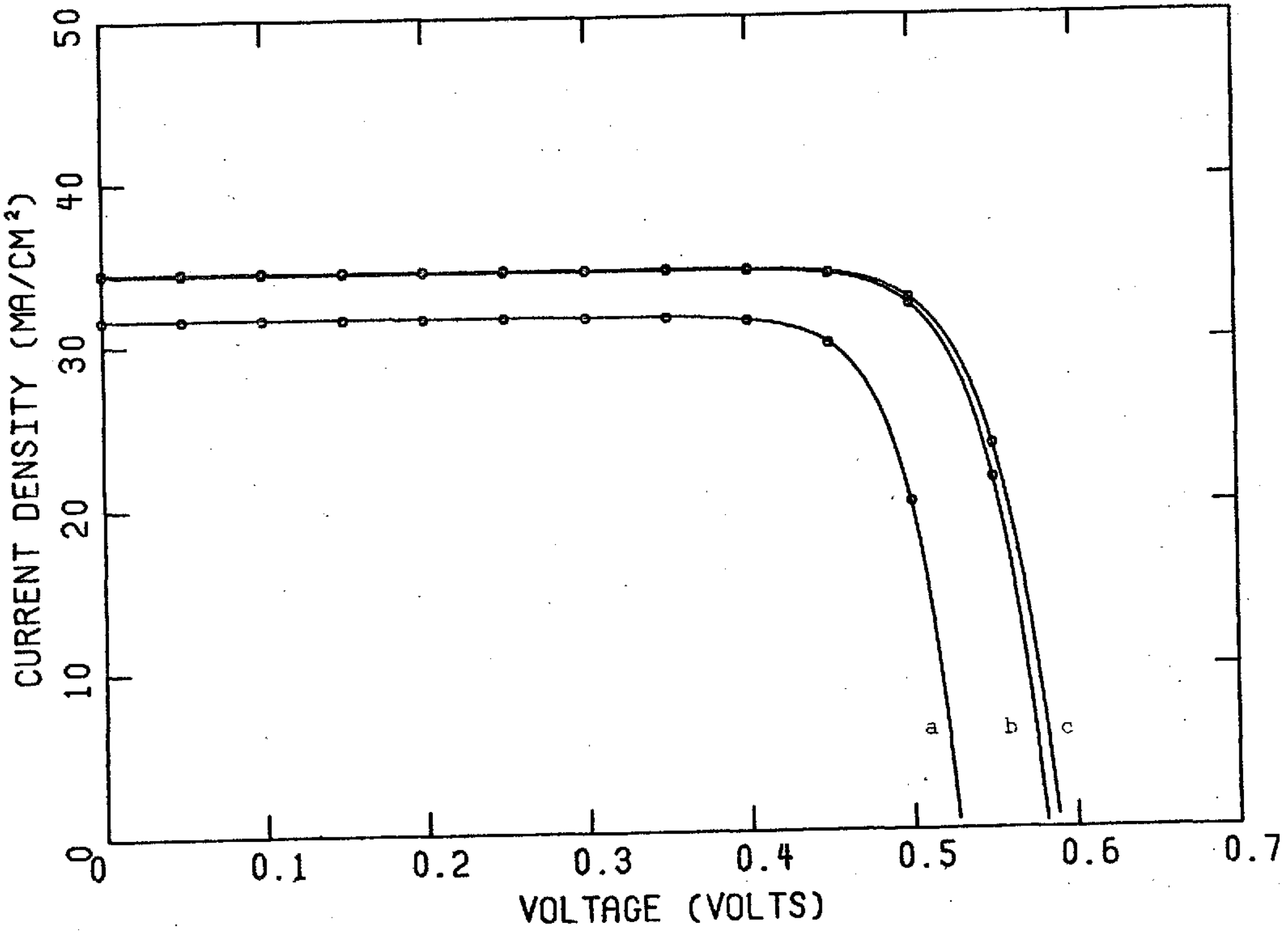

Figure 20. Terminal J-V characteristics for devices shown in Figure 19 for AM0 illumination.

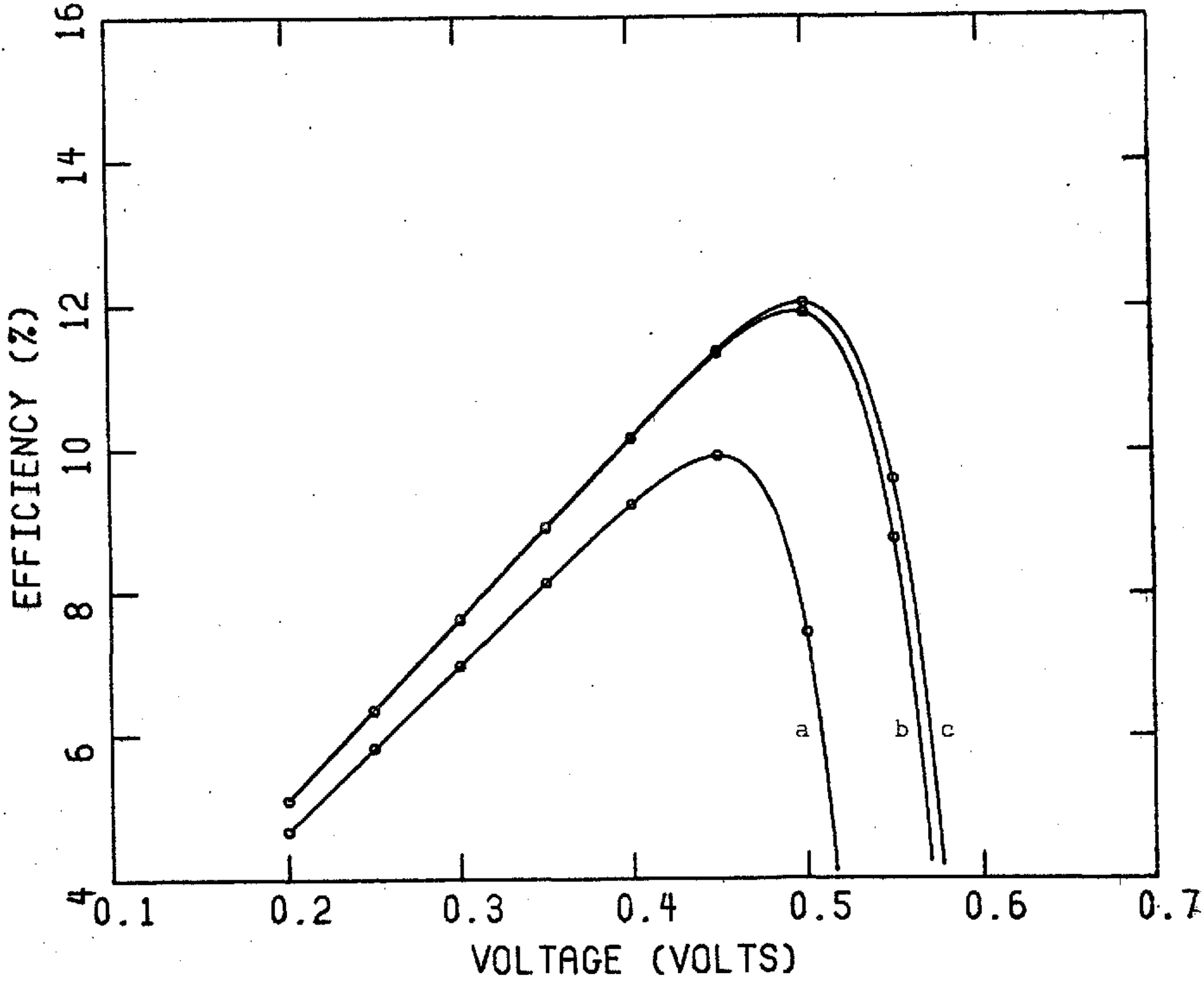

Figure 21. Efficiency characteristics of the (a) n^+-p, (b) n^+-p-p^+ with 0.5 μM p^+ region, and (c) n^+-p-p^+ with 5 μM p^+ region (AM0 illumination).

IV. LIMITED STUDY OF THE EFFECTS OF PARAMETER VARIATIONS ON SOLAR CELL EFFICIENCIES

This section discusses some calculations performed varying various parameters in order to study their influence on solar cell properties and efficiencies. The previous section has discussed the effects of varying the back contact properties of n^+-p-p^+ cells. The present section discusses three other types of parameter variations: (1) Lifetime variations, (2) Cell thickness variations, and (3) Cell resistivity and lifetime variations. As mentioned previously, all the results presented in this section were performed using an optical generation rate which is slightly (about 10%) too large for a bare silicon surface. This should not effect the general comparisons presented in this section but the short circuit currents shown are estimated to be too large. The calculated curves thus lie above 10% above the expected response for bare surface cells and about 30% below the response for cells with optimum antireflecting coatings. The calculations presented in this section are for bare surface silicon cells with the basic material parameters of Table I. Deviations from these basic parameters are discussed in each subsection.

1. Lifetime Comparison

The effect of p-region lifetime on the properties of the n^+-p-p^+ cell was studied for values ranging from 1 μsec to 100 μsec. The calculated terminal properties of cells are shown in Figures 22, 23, and 24. Complete data is shown for 10 μsec and 100 μsec lifetimes while partial data is shown in Figures 23 and 24 for a 1 μsec lifetime. The peak efficiency is seen to range from about 7% to about 12% for lifetime variations from 1 μsec to 100 μsec. The increased efficiency at long lifetimes results from (1) an increased short circuit current due to an increased carrier collection efficiency and (2) a reduced forward current density at long lifetimes due to decreased recombination of carriers in the p-type region.

Minority carrier lifetime is one of the major device parameters determining the efficiency of solar cells. It is also one of the least accurately known of the parameters used in the solar cell calculations. In general it is known that lifetime tends to decrease as the doping density is increased but the exact physical processes leading to such a decrease are not known. In order to set realistic bounds on solar cell efficiency, bounds on the lifetime at various doping densities must be established.

The minority carrier lifetime in the n^+-region used in the calculations is 0.1 μsec. This value of lifetime corresponds to a diffusion length of about 10 μM which is considerably larger than the thickness of the n^+-region. The electric field in the n^+-region due to the diffusion profile further increases the effective diffusion length for minority carrier collection at the p-n^+ junction. To obtain a diffusion length on the order of the n^+-region thickness would require a lifetime below 1 nsec, perhaps 0.1 nsec. Only for such low lifetime values is lifetime in the n^+-region expected to be an important device parameter. Computer calculations, however, need to be made to verify these conclusions.

2. Cell Thickness Comparison

Computer calculations were made varying the cell thickness to investigate the importance of this parameter on solar cell efficiency. Terminal characteristics are shown in Figures 25, 26, and 27 for n^+-p-p^+

cells with thicknesses of 100 μM, 200 μM and 250 μM. Figure 25 shows a slight decrease in current density as the cell thickness decreases. This is to be expected because of the reduced recombination of carriers in the p-region as thickness decreases. The short circuit current is seen to decrease in Figure 26 as the cell thickness decreases because of the reduced total carrier generation rate in the thinner cells. The reduced forward current density with thinner cells tends to increase cell efficiency while the reduced short circuit current tends to decrease the efficiency. The result of these two effects is a peak efficiency as shown in Figure 27 which does not depend very strongly on cell thickness. There is only a slight decrease in efficiency as the cell thickness is reduced from 250 μM to 100 μM.

The above conclusions hold only for n^+-p-p^+ type solar cells with the minority carrier reflecting back p-p^+ junction. For conventional n^+-p cells the efficiency decreases much faster as the cell thickness is reduced below a diffusion length. The decreased efficiency in conventional cells results from an increasing normal forward current density with decreasing thickness due to carrier flow to the back ohmic contact.

3. Cell Resistivity and Lifetime Variations

This section reports on one computer calculation which was made by varying the cell resistivity and lifetime. A calculation was made for the 250 μM thick n^+-p-p^+ cell with a p-region resistivity of 2000 Ω·cm and a lifetime of 1000 μsec. This choice of resistivity and lifetime was selected in order to enhance the importance of the back high-low junction. The values selected are approaching the highest resistivity and lifetime values which can be commercially obtained with bulk unprocessed silicon. It is recognized that these values may very well represent values which cannot presently be achieved in processed solar cells because of lifetime degradation during solar cell fabrication steps. The calculations were performed mainly to illustrate the importance of the high-low junction in high-resistivity silicon.

A comparison of the high resistivity, long lifetime device with a 10 Ω·cm, 100 μsec device is shown in Figures 28, 29, and 30. The J-V characteristic of Figure 28 has several interesting features. Because of the high resistivity of the 2000 Ω·cm cell, high injection occurs around 0.3 volt. This transition can be seen as a change in slope of the upper J-V characteristic at around 0.3 volt in Figure 28. The J-V characteristics for the two devices cross at about 0.45 volt with the 2000 Ω·cm cell having a lower current density than the 10 Ω·cm device for large voltages. The lower curve for the 2000 Ω·cm cell results from high injection effects and the approximate exp(qV/2kT) dependence at high injection where changes in the high-low junction potential are occurring. The 2000 Ω·cm cell also shows a slope change around 0.55 volt back toward an exp(qV/kT) variation of current density. This arises because of current leakage through the back high-low junction and recombination at the back ohmic contact. Potential and electron carrier density plots for this device at various voltage levels are shown in Appendix C.

Current density curves and efficiency curves under illumination are shown in Figures 29 and 30 respectively. Both devices have approximately the same short circuit current but the 2000 Ω·cm cell has a slightly larger open circuit voltage, resulting from the lower current density curve of Figure 28. The predicted efficiency of the 2000 Ω·cm cell is slightly larger as indicated in Figure 30.

The above calculations illustrate the importance of the high-low junction in high resistivity, long lifetime solar cells. Without accounting for the high injection effects at the high-low junction and the accompanying reduction in high-low junction potential, one would expect the 2000 Ω·cm cell to have a lower efficiency than the 10 Ω·cm cell. This would certainly be true if the current continued to depend on voltage as exp(qV/kT) as is observed at low voltages. However, the high injection effects combined with the high-low junction produces an exp(qV/2kT) dependence which leads to the reduced forward diode current and the increased efficiency.

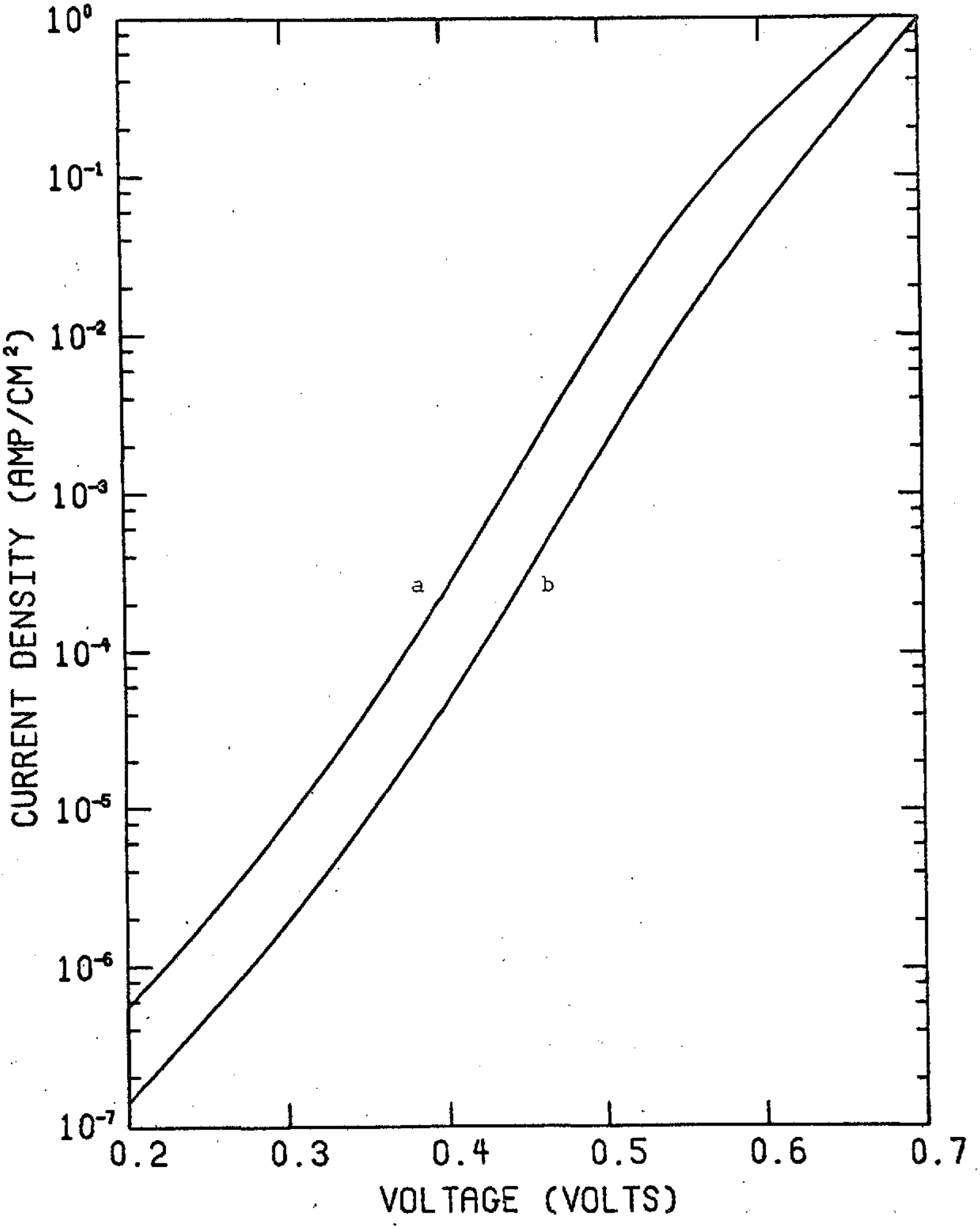

Figure 22. Terminal J-V characteristics for devices with a p-region minority carrier lifetime of (a) 10 μsec, (b) 100 μsec (no illumination).

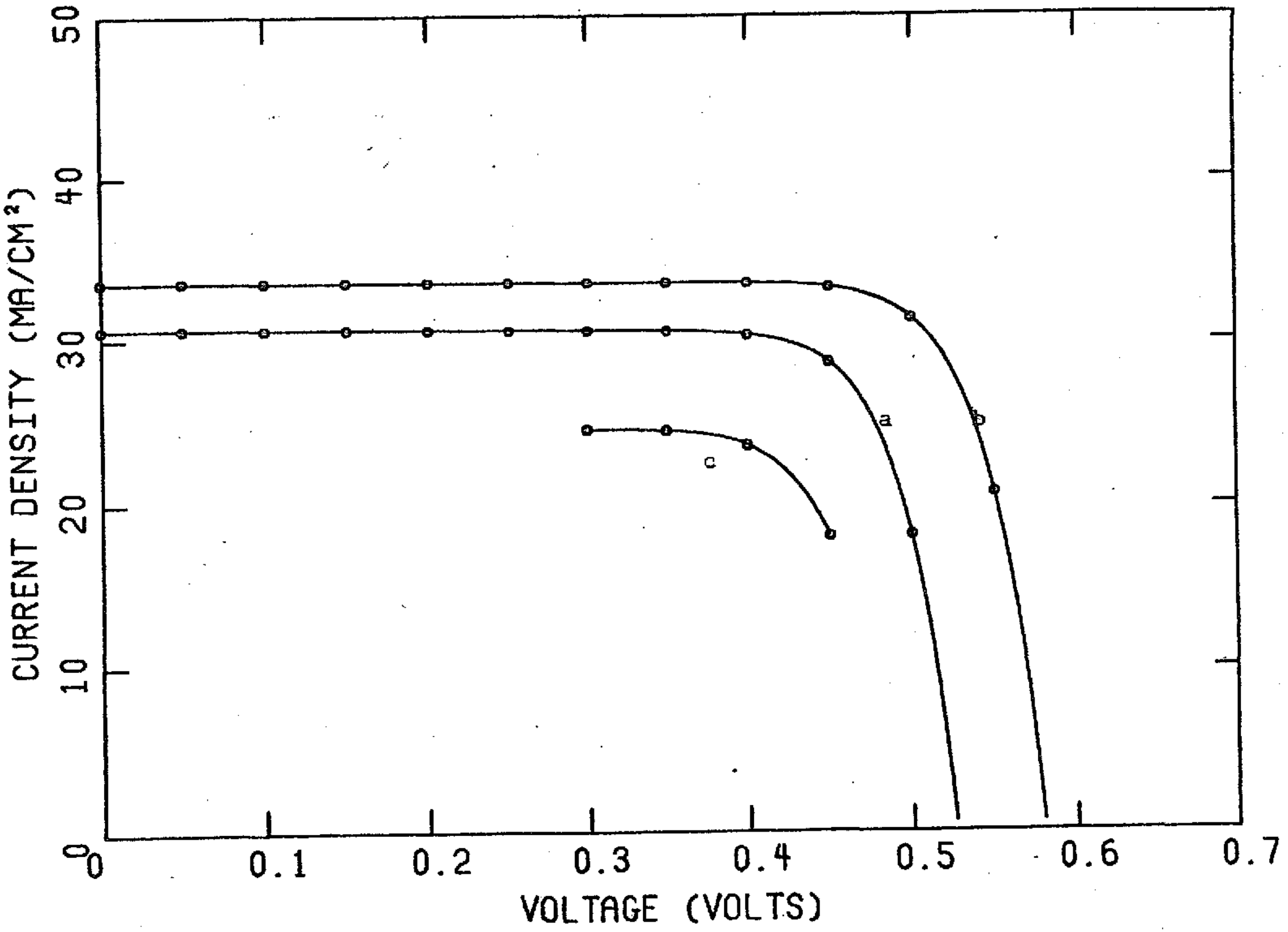

Figure 23. Terminal J-V characteristics for devices with a p-region minority carrier lifetime of (a) 10 μsec (b) 100 μsec and (c) 1 μsec (AM0 illumination).

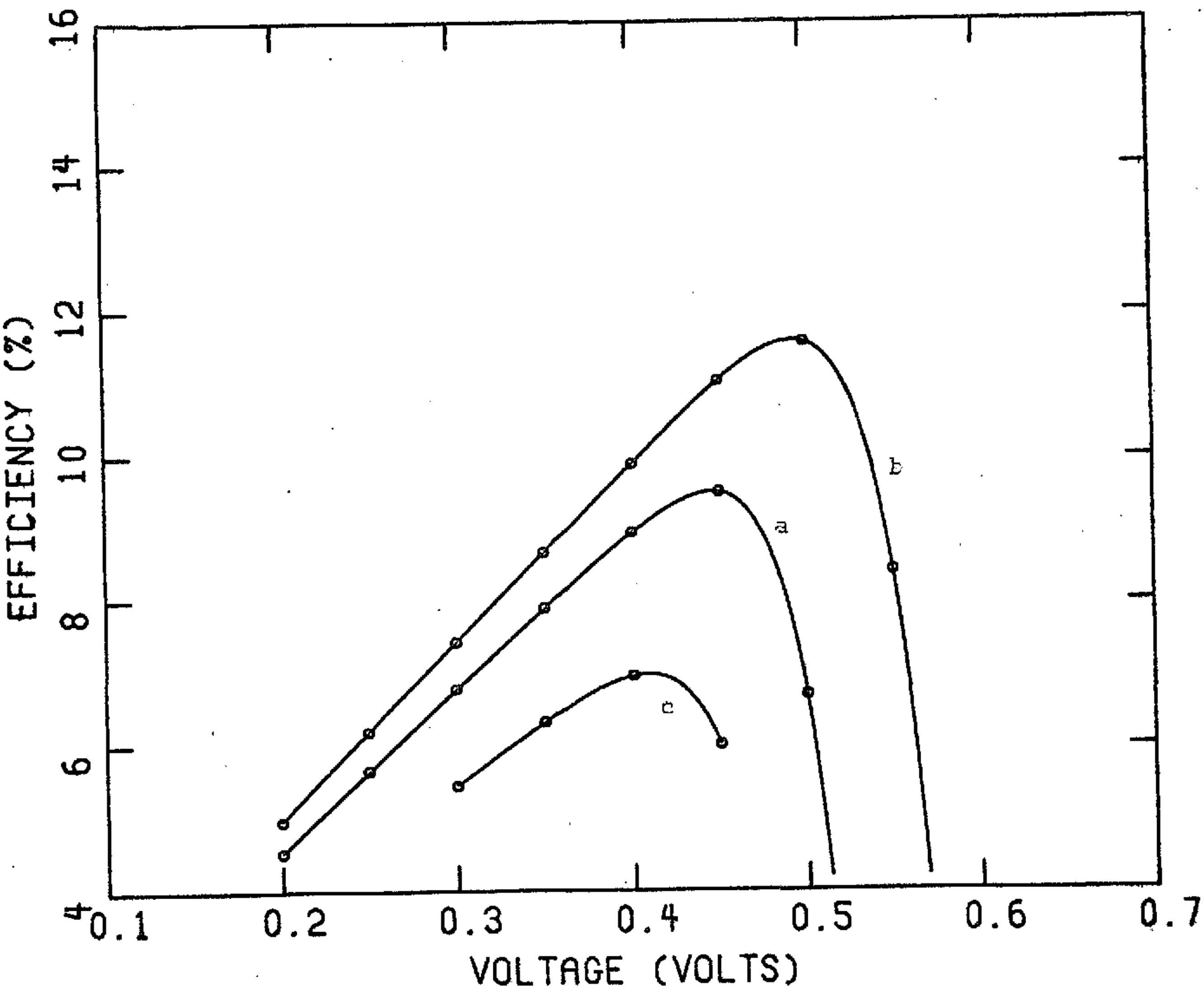

Figure 24. Efficiency characteristics for devices with a p-region minority carrier lifetime of (a) 10 μsec, (b) 100 μsec, (c) 1 μsec.

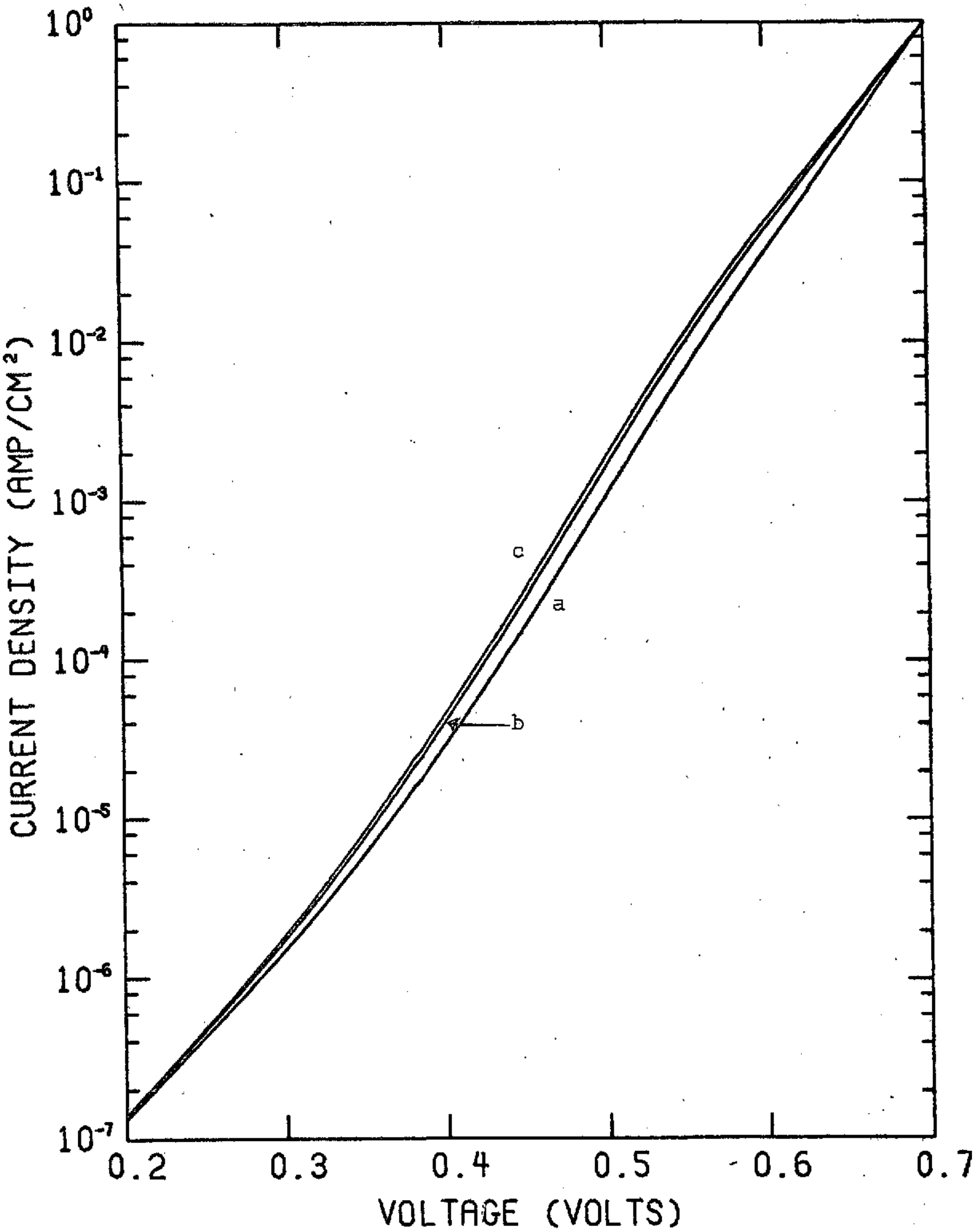

Figure 25. Terminal J-V characteristics for solar cells with various thicknesses(a) 100 μM, (b) 200 μM, and (c) 250 μM (no illumination).

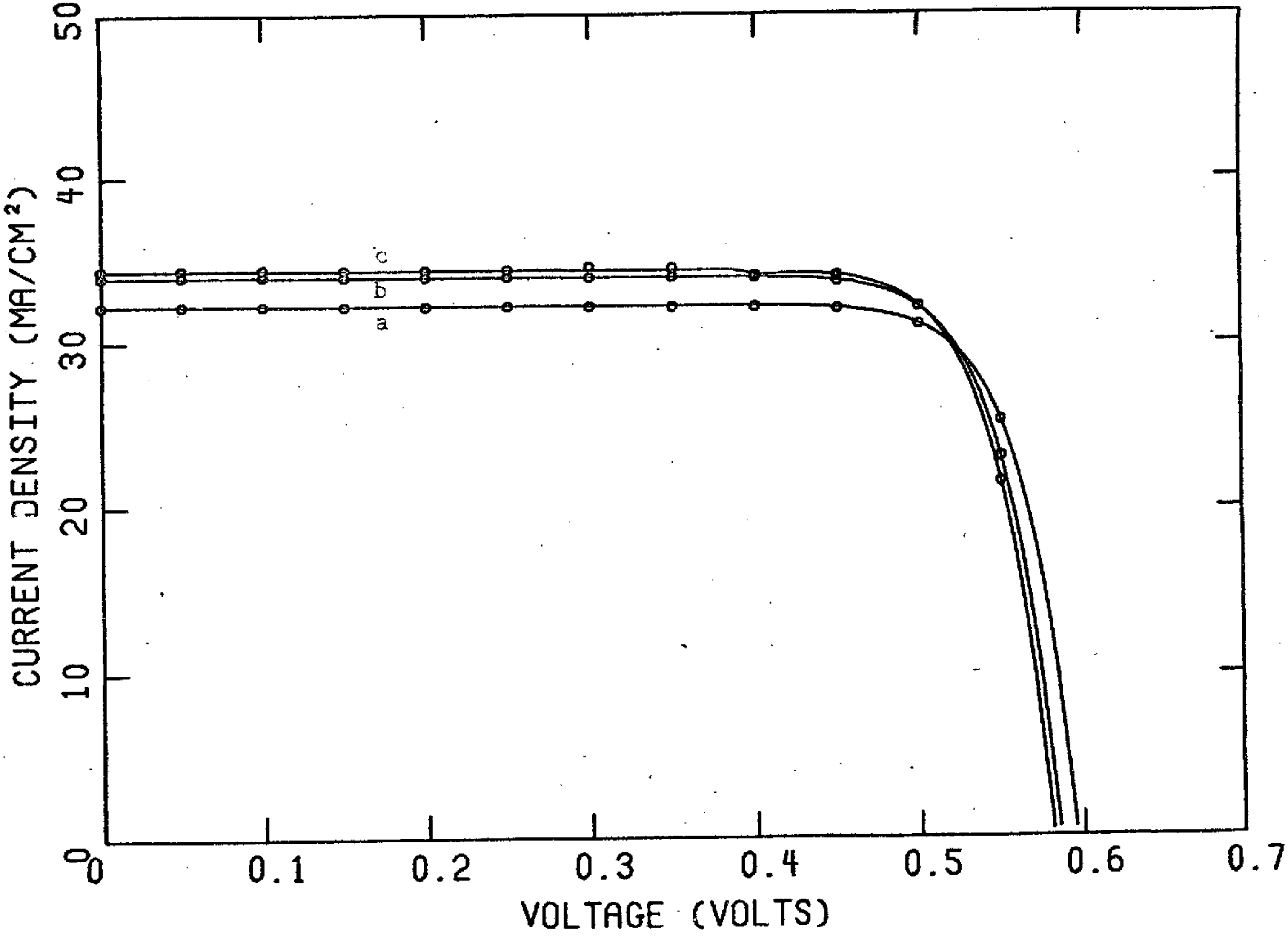

Figure 26. Terminal J-V characteristics for the devices in Figure 25 for AMO illumination.

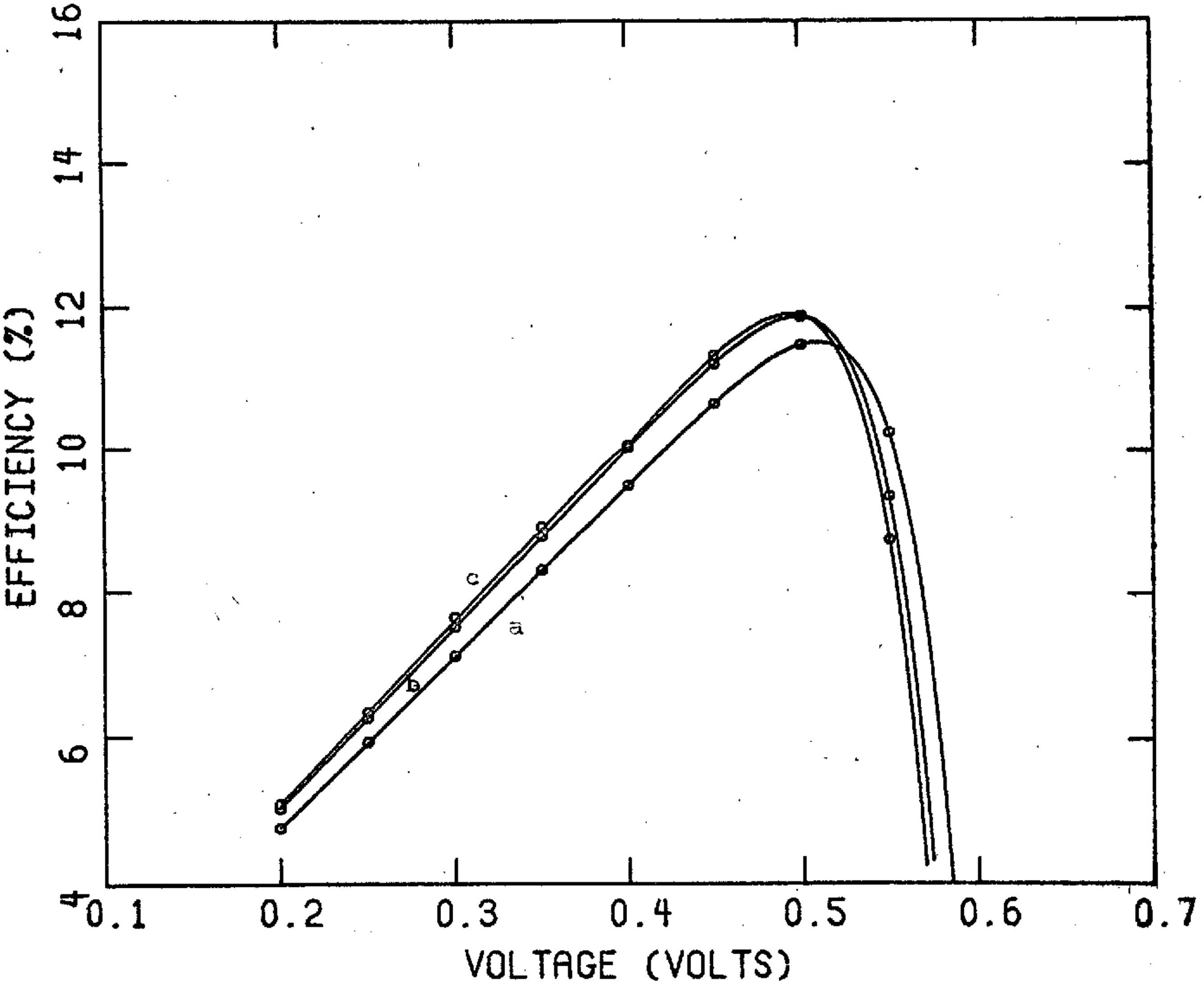

Figure 27. Efficiency characteristics for (a) 100 μM, (b) 200 μM, and (c) 250 μM thick solar cells (AMO illumination).

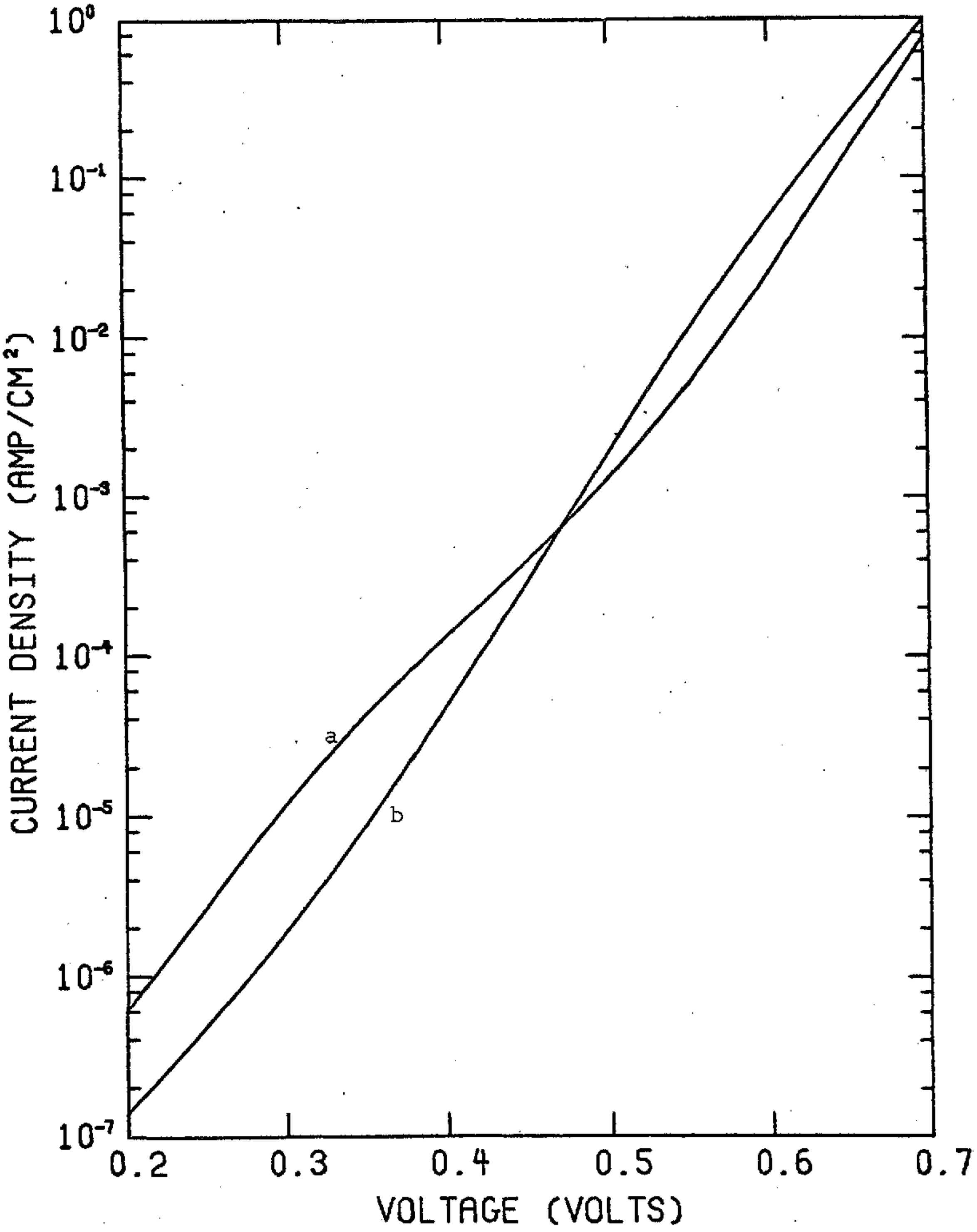

Figure 28. Terminal J-V characteristics for (a) 2000 Ω·cm, 1000 μsec p-region, (b) 10 Ω·cm, 100 μsec p-region (no illumination).

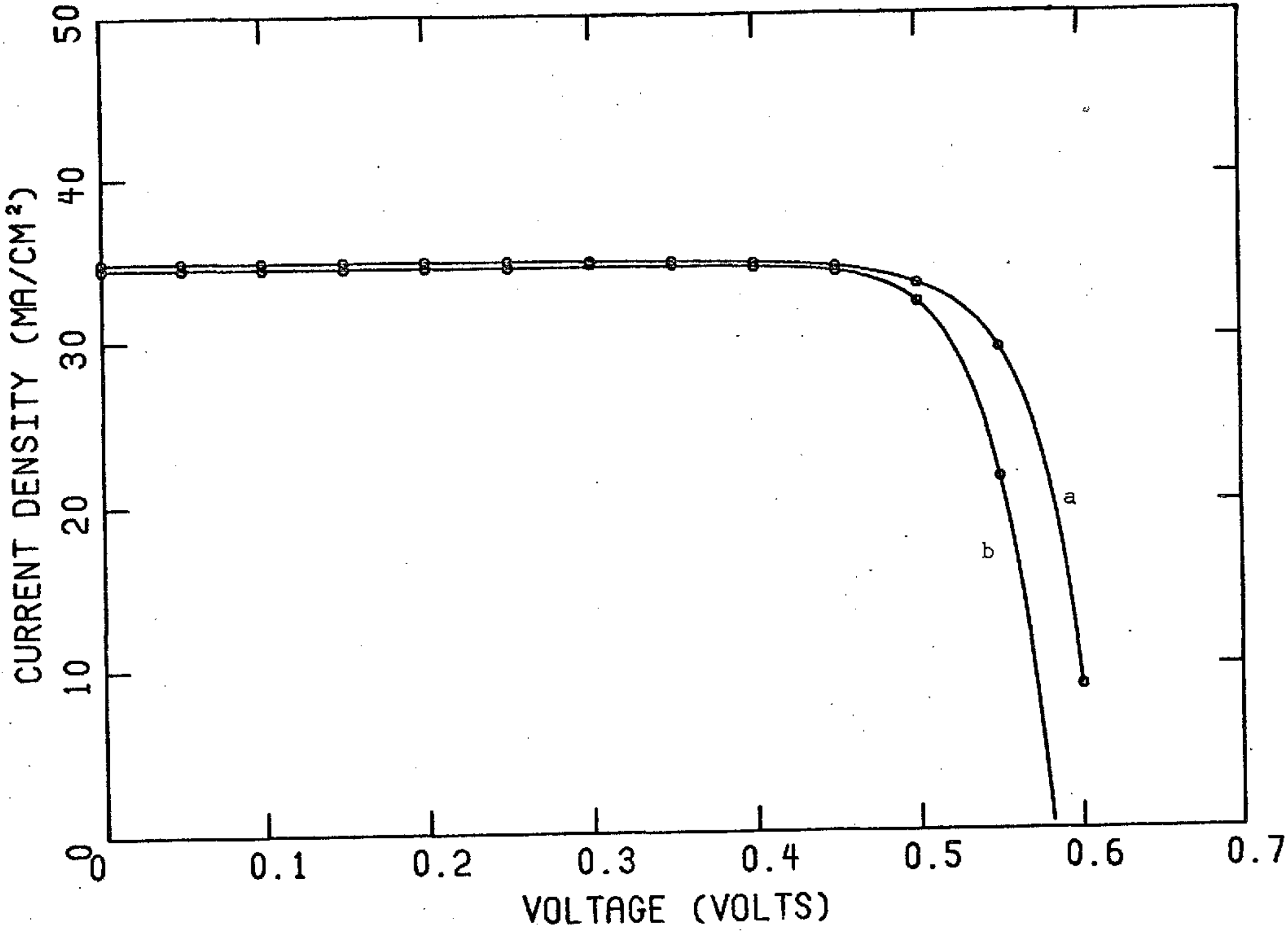

Figure 29. Terminal characteristics for the devices in Figure 28 for AM0 illumination.

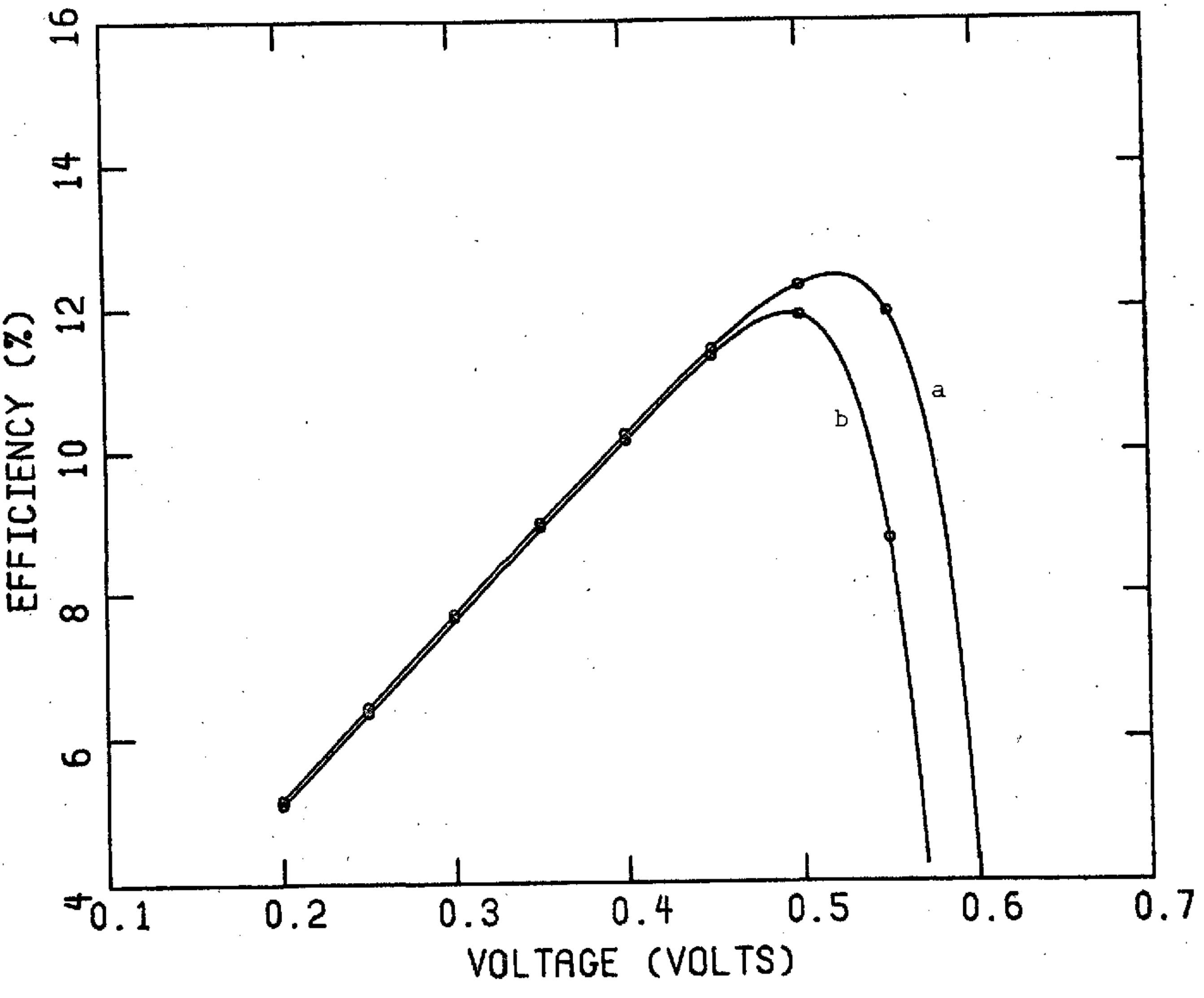

Figure 30. Efficiency characteristics for (a) 2000 Ω·cm, 1000 μsec p-region, (b) 10 Ω·cm, 100 μsec p-region (AM0 illumination).

V. SURFACE RECOMBINATION

Calculations have been initiated which include the effect of a finite surface recombination velocity at the irradiated surface. With this finite term the current at the surface may be expressed as follows (normalized form):

$$J_p\Big|_{surface} = (p-p_o)S = \frac{p}{\gamma_p}\;\frac{d\phi_p}{dx}\Big|_{surface}, \tag{7}$$

where S is the surface recombination velocity. Following the procedure illustrated in Appendix A, the variables ϕ_p, ϕ_p', and ψ may be expressed in the form

$$\phi_{p(i+1)} = \phi_{p(i)} + \delta\phi_{p(i)}, \tag{8}$$

where the subscript "i" refers to the iteration step. Applying this form to the independent variables in equation (7) one may obtain an expression for the correction to ϕ_p at the surface $(\delta\phi_{p(IL)})_i$ in terms of the values of ϕ_p, ϕ_p', and ψ at the prior iteration step. Included in this expression is the term $\delta\phi_p'$ which can be expressed in terms of $\delta\phi_{p(IL)}$ and $\delta\phi_{p(IL-1)}$. By utilizing the "C" coefficients of Appendix A plus the fact that $\delta\psi_{(IL)} = 0$, $\delta\phi_{p(IL-1)}$ may be expressed in terms of $\delta\phi_{p(IL)}$ thus yielding the final explicit expression for $\delta\phi_{p(IL)}$. The correction to ϕ_n is formed by invoking charge neutrality at the surface. This method provides an ongoing correction process as the device bias is stepped. The inclusion of this correction in fact reduces convergence difficulties at the surface since the carrier concentrations at the surface do not need to return to equilibrium conditions. As can be seen from Figures 4(b) and 11(b), an infinite S demanded a large change in ϕ_p over an extremely small distance near the surface.

A surface recombination velocity of 10^3 cm/sec was selected as a reasonable value and the cell described in the prior sections illustrated a terminal J-V characteristic (no illumination) which was within 1% of the prior results. However, the hole current at the n^+ surface was reduced at least two orders of magnitude. Although no calculations have as yet been performed under AM0 illumination it can be expected that the short circuit current may be increased by as much as 2 mA/cm^2. This estimate can be based on the consideration that the present hole current lost to recombination at the surface is about 2.2 mA/cm^2 (Figure 15(b)) and a two order magnitude decrease of this component will add directly to the overall short circuit current.

VI. SUMMARY

This report has summarized the work accomplished to date on the theoretical analysis of solar cell current-voltage characteristics and efficiencies. The study is only partially complete at the present time. The major accomplishments which have so far been achieved are: (1) The development of a general analysis program for n^+-p and n^+-p-p^+ solar cells, (2) The incorporation of optical generation into the analysis with the capability of including antireflecting surface layers into the model, (3) An initial series of solar cell calculations exploring the effects of various device parameters on solar cell properties, and (4) The incorporation of finite surface recombination effects into the model. The calculations which have been performed illustrate the usefulness and versatility of the analysis techniques for studying solar cells.

A major effort in the initial calculations has been to understand the influence of a back p^+-p, high-low junction on solar cell properties. The theoretical calculations indicate that below high injection the high-low junction acts predominantly as a minority carrier reflecting boundary preventing injected carriers or optically generated carriers from reaching the back ohmic contact and recombining. The net effect on solar cell operation is a reduction in normal forward bias current over n^+-p cells and an increase in short circuit current. The back high-low junction was found to have little influence on the terminal properties or on efficiency when the minority carrier diffusion length is less than the cell thickness. When the cell resistivity is high enough to cause high injection at open circuit voltage conditions, a voltage decrease across the high-low junction was found to be a significant factor in determining the cell efficiency. To observe a significant change in high-low junction potential under AMO illumination was found to require a resistivity of about 10 Ω·cm or larger.

Research is continuing in several areas with the present analysis program and future plans include the extension of the program to include other physical effects. The analysis is continuing into the effects of various parameter variations on efficiency with corrections being made for the slightly incorrect optical generation rate used in the early calculations. Calculations also need to be made exploring the differences, if any, when antireflecting coatings are present. The influence of various p-region resistivities on efficiency needs to be thoroughly explored since different resistivity material may lead to higher open circuit voltages and increased efficiencies. In this connection, however, it is very important to also vary the minority carrier lifetime or diffusion length in a realistic manner with resistivity variations. Considerable thought must be given to the establishment of some upper and lower bounds on lifetime as a function of resistivity in order to fully explore this area.

New effects which are to be included in the analysis program are: (1) Heavy doping or degeneracy effects in the n^+-region and (2) Two dimensional effects due to the geometry of the top solar cell contacts, The inclusion of these effects are needed to accurately describe solar cells. Heavy doping in the n^+-region is expected to be important in determining the optical absorption in the n^+-region and the loss of carriers to recombination at the surface of the n^+-region. The two dimensional properties are important in determining the effective series resistance of the cell and in determining the curve (fill) factor.

In summary, the work is proceeding at present approximately on schedule. No major problems are evident at present which would prevent a successful development of a general computer analysis program for solar cells.

Appendix A: A Numerical Method for the Analysis of Semiconductor p-n Junction Devices

J. R. Hauser, P. M. Dunbar, and E. D. Graham[†]

Electrical Engineering Department
North Carolina State University
Raleigh, North Carolina 27607

[†] Present address: Sandia Laboratories, Albuquerque, New Mexico.

ABSTRACT

A numerical technique, utilizing the computer, is developed to obtain solutions to the one-dimensional semiconductor device equations. These equations form a set of three, second order, nonlinear, coupled differential equations. Quasilinearization is used to convert these equations to a set of coupled linear equations. Iteration techniques are then employed to obtain numerical solutions which converge to the solutions of the original set of equations. These techniques have been applied to conventional n^+-n-p^+ diodes as well as to shallow diffused structures of the p^+-p-n^+ type. Some of these results are presented illustrating this analytical method.

I. INTRODUCTION

Since the origin of semiconductor device theory in the late 1940's, numerous attempts at solving the semiconductor device equations have come forth. However, purely analytical methods have yielded closed-form solutions only for very simplified cases, and only over limited operating ranges. Various numerical methods for the determination of device characteristics have been presented in the literature with the better ones evolving from the work of Gummel [1]. The present work provides accurate solutions of the device equations by means of a recently developed quasilinearization process and iterative procedures. To utilize these techniques the one dimensional semiconductor device equations are normalized (as De Mari [2] and others have done) and reduced to a set of three coupled, non-linear partial differential equations. Solution of these equations for a given device structure, doping profile, and recombination model yields the desired device characteristics for either a static or transient response. The chief advantage of the numerical methods presented here over previously developed schemes lies in the rapid convergence of the iterations afforded by the quasi-linearization technique.

A considerable amount of work has previously been performed on computer techniques for the solution of the semiconductor device equations (Reference [3] presents a review of most of this work). Much of this work however, has been restricted to the case of zero recombination-generation. For the majority of devices this is not a good approximation. Subsequently, one of the major objectives of the present work has been the development of analysis techniques which are applicable to the general case of non-zero generation-recombination. This general case leaves one with three second order differential equations as opposed to the two first order and one second order differential equations resulting from the zero generation-recombination model. This type of generalization adds another level of difficulty to the problem of convergence in a numerical technique [4]. Numerical solutions to the general case have also been reported by Fulkerson and Naussbaum [5]; however, their work deals with a particular device and is applicable to a rather restricted voltage range. In the present paper, the methods are applicable to a wide range of device structures, doping profiles, recombination models, external generation mechanisms, and applied voltages.

In the analysis of semiconductor devices, the terminal current-voltage characteristics are usually of major interest. The terminal characteristics, however, are determined by the details of the electron and hole densities and electric field throughout the bulk of the device as well as any time dependence of these quantities. Thus before the terminal characteristics can be obtained, the electron and hole densities as well as electric potential must be known throughout the device. Straightforward means exist for relating the terminal properties to the bulk carrier densities and potential.

The basic semiconductor device equations are very nonlinear and this leads to difficulties in device analysis. Even though these basic equations are easily formulated, they are not easily solved even with computer techniques. Some of the difficulties in obtaining solutions arise from the very rapid changes which occur in carrier densities near a p-n junction. For example, across a p-n junction depletion region the carrier densities may change by more than ten orders of magnitude and this may occur over a distance of only 10^{-4}cm. The total dimensions of a semiconductor device may, however, be several hundred (or more) times the 10^{-4}cm dimension. Thus the major changes in carrier densities and potential occur over distances which are usually small compared with the total device dimensions. When viewed on a distance scale which spans the dimensions of the entire device, the changes in carrier densities often appear as steps occurring at the interfaces between p and n regions. These very abrupt changes in properties at junction interfaces are very clearly shown in the computed curves in this paper.

The very rapid changes in carrier densities and potential near interfaces provide the basis for most analytical approaches to device analysis. They make possible the approximate division of a semiconductor into space charge regions and electrically neutral (or nearly electrically neutral) regions. By using simplifying approximations to the device equations in the various regions of a device, reasonably good, first order, analytical approximations can be obtained to the terminal properties of semiconductor devices. The abrupt changes in the character of the device equations near interfaces which make possible the usual device approximations, give rise in exact numerical solutions to some of the major difficulties in solving the device equations. These problems are discussed in more detail in Section III on numerical techniques.

II. SEMICONDUCTOR DEVICE EQUATIONS

The analysis of semiconductor devices is based upon the following set of equations (for one-dimension only):

$$\frac{\partial E}{\partial x} = \frac{q}{\varepsilon}\,[p - n + N(x)], \tag{1}$$

$$E = -\frac{\partial \psi}{\partial x}, \tag{2}$$

$$J_n = q\mu_n nE + qD_n \frac{\partial n}{\partial x}, \tag{3}$$

$$J_p = q\mu_p pE - qD_p \frac{\partial p}{\partial x}, \tag{4}$$

$$\frac{\partial n}{\partial t} = U + G_e + \frac{1}{q}\frac{\partial J_n}{\partial x}, \tag{5}$$

$$\frac{\partial p}{\partial t} = U + G_e - \frac{1}{q}\frac{\partial J_p}{\partial x}. \tag{6}$$

These equations have general three dimensional forms; however, in this work only the one dimensional case has been considered. In the above equations q is the electronic charge, ε is the dielectric permittivity and the other terms are defined in Table 1. The net ionized impurity doping is represented by N(x) and can be a complicated function of x, changing from a positive to a negative value as an n-p interface is crossed. The first two equations (Eqs. (1) and (2)) are Poisson's equation and the defining relationship between electrostatic potential ψ and electric field E. Equations (3) and (4) are current density equations while Eqs. (5) and (6) are continuity equations for electrons and holes. Internal recombination or generation of electron-hole pairs due to thermal processes is represented by U, while electron-hole pair generation due to external sources such as incident light is represented by the term G_e.

As in most computer techniques it is convenient to work in a set of normalized dimensionless variables. In the remainder of this work, except for explicitly indicated points, the variables will be taken as quantities normalized by the factors in Table 1. Utilizing this normalization and the interrelationship between mobility and diffusion constants, the device equations may be rewritten as follows:

$$\frac{d^2\psi}{dx^2} = n - p + N, \tag{7}$$

$$J_n = \mu_n \left(n \frac{\partial\psi}{\partial x} - \frac{\partial n}{\partial x}\right), \tag{8}$$

$$J_p = \mu_p \left(p \frac{\partial\psi}{\partial x} + \frac{\partial p}{\partial x}\right), \tag{9}$$

$$\frac{\partial n}{\partial t} = - U - G_e - \frac{\partial J_n}{\partial x}, \tag{10}$$

$$\frac{\partial p}{\partial t} = - U - G_e + \frac{\partial J_p}{\partial x}. \tag{11}$$

Through an appropriate choice of three independent variables, Eqs. (7-11) can be reduced to a set of three coupled equations in three variables. There are several possible choices for these independent variables. For example ψ, n, and p form one possible set. These variables are the ones normally used in device analysis programs [3]. The approach taken in this work, however, has been to introduce electron and hole quasi-Fermi levels, ϕ_n and ϕ_p, and take these, plus the electrostatic potential, ψ, as the three independent variables. The normalized quasi-Fermi levels are related to the carrier concentrations as

$$n = \exp(\psi - \phi_n), \tag{12}$$

and

$$p = \exp(\phi_p - \psi). \tag{13}$$

This approach yields three variables with approximately the same magnitude of variation across a device simplifying the scaling of the numerical techniques.

In terms of these three variables ψ, ϕ_n, and ϕ_p the semiconductor device equations (Eqs. (7)-(13)) can be written as

$$\frac{\partial^2\psi(x,t)}{\partial x^2} = \exp\,[\psi-\phi_n] - \exp\,[\phi_p-\psi] - N(x), \tag{14}$$

$$[\frac{\partial\psi}{\partial t} - \frac{\partial\phi_n}{\partial t}]\,\gamma_n(x,t) - \frac{\partial^2\phi_n}{\partial x^2} = -\,\gamma_n(x,t)G_e(x,t)\,\exp\,(\phi_n-\psi) + \frac{\partial\phi_n}{\partial x}\,[\frac{\partial\psi}{\partial x} - \frac{\partial\phi_n}{\partial x} - \frac{1}{\gamma_n}\frac{\partial\gamma_n}{\partial x}] - \gamma_n(x,t)U(x,t), \tag{15}$$

and

$$[\frac{\partial\phi_p}{\partial t} - \frac{\partial\psi}{\partial t}]\,\gamma_p(x,t) - \frac{\partial^2\phi_p}{\partial x^2} = \gamma_p(x,t)G_e(x,t)\exp(\psi-\phi_p) + \frac{\partial\phi_p}{\partial x}\,[\frac{\partial\phi_p}{\partial x} - \frac{\partial\psi}{\partial x} - \frac{1}{\gamma_p}\frac{\partial\gamma_p}{\partial x}] - \gamma_p(x,t)U(x,t). \tag{16}$$

The quantities γ_n and γ_p are the reciprocal (normalized) mobilities.

The nonlinearity of these equations is further compounded by the choice of recombination model, character of external generation, and the inclusion of field and doping dependent mobilities, *i.e.* γ_n and γ_p are functions of $N(x)$ and $\partial\psi/\partial x$. For recombination, the single level Shockly-Read-Hall model has been used. In normalized form this model results in the following net recombination rate:

$$U = \frac{\exp[\phi_p-\phi_n] - 1}{\tau_{po}[\exp(\psi-\phi_n)-n_1] + \tau_{no}[\exp(\phi_p-\psi)-p_1]} \tag{17}$$

where τ_{po}, τ_{no}, n_1 and p_1 are constants depending on the location and density of recombination levels. This has been found to be a good approximation to recombination in Ge and Si. For most of the numerical calculations, the recombination level has been assumed to exist at the center of the energy band gap so that $n_1=p_1=1$. This has been done for convenience only and the general expressions are valid for any values of n_1 and p_1.

The mobility dependence was modeled by empirical expressions taken from Gwyn, et al. [6] which are of the form

$$\mu_n^{-1} = \mu_{no}^{-1} [1 + C_1N/(N+C_2) + C_3E^2 {\frac{E+C_4}{E+C_5}}^{1/2}] , \qquad (18)$$

$$\mu_p^{-1} = \mu_{po}^{-1} [1 + K_1N/(N+K_2) + K_3E^2 {\frac{E+K_4}{E+K_5}}^{1/2}] , \qquad (19)$$

Normalized values of the parameters in the mobility expressions are given in Table II. These expressions have been found to accurately describe both the doping and field dependence of mobility in silicon. Somewhat similar expressions would also be used with other semiconductors with different constants.

An external generation term G_e could be developed for various applications; however, the mechanism studied in this work has been that of generation due to the full spectrum solar irradiance. This semi-empirical model for G_e was based on published data of absorption coefficients, index of refraction, and spectral irradiance. The modeling of this term has been developed in work presently underway; however, the resulting normalized term can be expressed as follows:

$$G_e(x) = \frac{L_D^2}{D_o n_i} \int T(\lambda)N_{ph}(\lambda)\eta(\lambda)\alpha(\lambda)\exp[-\alpha(\lambda)x]d\lambda . \qquad (20)$$

Data showing the typical dependence for silicon of $G_e(x)$ upon distance is shown in Fig. 1 for solar irradiation which is present at the earth but outside the earth's atmosphere (so called air mass zero, AMO, condition). For other conditions such as absorption of light at the earth's surface (AM1) or for other semiconductors, G_e will be a somewhat different function of x. Only for monochromatic light incident on a semiconductor is $G_e(x)$ a simple function of distance which is easily expressed in functional form. In general, $G_e(x)$ is a rapidly decreasing function of distance from the irradiated surface, and its value is normally only known as a table of values.

III. NUMERICAL TECHNIQUES

The solution of the semiconductor device equations has been reduced in Section II to the solution of three coupled nonlinear equations (Eqs. (14)-(16)). The known values of ψ, ϕ_n and ϕ_p are at the boundaries of the semiconductor device. Thus, the mathematical problem reduces to the solution of a rather complicated nonlinear two-point boundary-value problem. Although there are several techniques available for solving linear differential equations of the two point boundary value type, no such general techniques exist for nonlinear equations. Solutions of these problems generally require some type of iterative technique whereby the solution is approached in a series of steps. The present work utilizes the quasilinearization technique whereby the system of nonlinear equations is converted into a system of linear equations [7-9]. An iterative technique is then used to obtain the exact solution. The general principle behind this approach is expanded in Appendix A.

As an illustrative example, the solution methods have been applied to the n^+-n-p^+ (and p^+-p-n^+) structure shown in Fig. 2. Since the electrostatic potential (ψ) is arbitrary to within a constant, it may be taken as zero at x = 0. Its value at x = L is then the built-in voltage plus the applied terminal voltage. The boundary conditions of the quasi-Fermi levels ϕ_n and ϕ_p are then determined from the defining Eqs. (12) and (13) and the values of the carrier concentrations, n and p, at the boundaries. If ohmic contacts are assumed at both end points, the carrier concentrations are fixed at their equilibrium values which are independent of the applied voltage. This leads to the condition that ϕ_n and ϕ_p are both constant at x = 0 and increase at x = L directly with the applied terminal voltage. The restriction of ohmic contacts at $x = 0$ and $x = L$ may be loosened to allow for a finite surface recombination velocity at this end point. However, to more clearly illustrate the analysis technique, ohmic contacts will be assumed.

To proceed with the technique, the coupled device equations can be written in the following functional form:

$$\frac{\partial^2 \psi(x,t)}{\partial x^2} = F_1(\psi, \phi_n, \phi_p), \tag{21}$$

$$\left[\frac{\partial \psi}{\partial t} - \frac{\partial \phi_n}{\partial t}\right]\gamma_n(x,t) - \frac{\partial^2 \phi_n(x,t)}{\partial x^2} = F_2(\psi,\ \phi_n,\ \phi_p,\ \psi',\ \phi_n'), \tag{22}$$

$$\left[\frac{\partial \phi_p}{\partial t} - \frac{\partial \psi}{\partial t}\right]\gamma_p(x,t) - \frac{\partial^2 \phi_p(x,t)}{\partial x^2} = F_3(\psi,\ \phi_n,\ \phi_p,\ \psi',\ \phi_p'). \tag{23}$$

The functions F_1, F_2, and F_3 correspond to the right hand sides of Eqs. (14), (15), and (16) respectively.

In the quasilinearization technique (as discussed in Appendix A) the nonlinear differential equations, instead of being solved directly, are solved recursively by a series of linear differential equations. The linear equations to be solved are obtained from the first order terms of a Taylor's series expansion of the nonlinear part of the original differential equation (terms F_1, F_2, and F_3 above). This technique is a generalized Newton-Raphson formula for functional equations [7-9]. In order to illustrate the quasilinearization technique as applied to the semiconductor device equations, Eq. (22) is considered as a typical equation.

Applying the quasilinearization technique to Eq. (22) gives

$$
\begin{aligned}
&[\frac{\partial\psi_{m+1}}{\partial t} - \frac{\partial\phi_{n,m+1}}{\partial t}]\gamma_n - \frac{\partial^2\phi_{n,m+1}}{\partial x^2} = F_2|_m \\
&+ \frac{\partial F_2}{\partial\psi}|_m(\psi_{m+1}-\psi_m) + \frac{\partial F_2}{\partial\phi_n}|_m(\phi_{n,m+1}-\phi_{n,m}) \\
&+ \frac{\partial F_2}{\partial\phi_p}|_m(\phi_{p,m+1} - \phi_{p,m}) + \frac{\partial F_2}{\partial\psi'}|_m(\psi'_{m+1} - \psi'_m) \\
&\quad + \frac{\partial F_2}{\partial\phi_n'}|_m(\phi'_{n,m+1} - \phi'_{n,m}), \qquad (24)
\end{aligned}
$$

where the subscripts m and m+1 indicate the m and m+1 iteration steps. Approximate solutions to ψ_m, $\phi_{n,m}$, and $\phi_{p,m}$ are assumed known in order to generate the solution at the m+1 iteration step. The partial derivative terms of F_2 such as $\partial F_2/\partial\phi_n|_m$ are also assumed known since they are evaluated using ψ_m, $\phi_{n,m}$, and $\phi_{p,m}$. Also ψ' and ϕ_n' represent first derivatives with respect to distance. Equations similar to Eq. (24) can easily be obtained for the other two equations (Eqs. (21) and (23)).

By the above technique the three device equations are converted into three linear differential equations. Starting with some initial approximation to ψ, ϕ_n, and ϕ_p at iteration step m = 1 the functions ψ_1, $\phi_{n,1}$, and $\phi_{p,1}$ are known and ψ_2, $\phi_{n,2}$, and $\phi_{p,2}$ are calculated. These new solutions are used to generate a better solution set with the process continuing until the solutions converge within some specified degree of accuracy. In solving the linear differential equations in an iterative manner, it has been found convenient to express the equations in terms of correction terms at the m'th iteration step as

$$\begin{aligned} \delta\psi_m &= \psi_{m+1} - \psi_m, \\ \delta\phi_{n,m} &= \phi_{n,m+1} - \phi_{n,m}, \qquad (25) \\ \delta\phi_{p,m} &= \phi_{p,m+1} - \phi_{p,m}. \end{aligned}$$

Since the solution is numerical, discrete points in space and time must be used at which the values of ψ, ϕ_n, and ϕ_p are calculated. These points are identified as i,k; where i is an integer specifying the x-coordinate and k is an integer specifying the time coordinate. Applying these definitions to Eq. (24), it may be rewritten as

$$\begin{aligned} &[\frac{\partial\delta\psi}{\partial t}\Big|_{m,i,k} - \frac{\partial\delta\phi_n}{\partial t}\Big|_{m,i,k}]\gamma_{n_{m,i,k}} - \frac{\partial^2\delta\phi_n}{\partial x^2}\Big|_{m,i,k} = \{F_2\Big|_{m,i,k} + \\ &\gamma_n\frac{\partial\phi_n}{\partial t}\Big|_{m,i,k} - \gamma_n\frac{\partial\psi}{\partial t}\Big|_{m,i,k} + \frac{\partial^2\phi_n}{\partial x^2}\Big|_{m,i,k}\} + \frac{\partial F_2}{\partial\psi}\Big|_{m,i,k}\delta\psi_{m,i,k} \\ &\quad + \frac{\partial F_2}{\partial\phi_n}\Big|_{m,i,k}\delta\phi_{n_{m,i,k}} + \frac{\partial F_2}{\partial\phi_p}\Big|_{m,i,k}\delta\phi_{p_{m,i,k}} + \qquad (26) \\ &\quad \frac{\partial F_2}{\partial\psi'}\Big|_{m,i,k}\delta\psi'_{m,i,k} + \frac{\partial F_2}{\partial\phi'_n}\Big|_{m,i,k}\delta\phi'_{n_{m,i,k}} \end{aligned}$$

Similar differential equations may be obtained for $\delta\psi$ and $\delta\phi_p$. The solution to these equations give the corrections to ψ, ϕ_n and ϕ_p at each iteration step.

The system of differential equations has been solved by the finite difference approach using approximations of the Crank-Nicolson type [10] for the time dependent case and of the three point difference type for the time independent case. Following the use of finite differences to approximate the derivatives, a set of three coupled finite difference equations results, which are of the form,

$$\delta\psi_{i-1} = A^i_{11}\,\delta\psi_i + A^i_{12}\,\delta\phi_{n_i} + A^i_{13}\,\delta\phi_{p_i} + A^i_{14} + B^i_{11}\delta\psi_{i+1}, \tag{27}$$

$$\begin{aligned}\delta\phi_{n_{i-1}} = A^i_{21}\,\delta\psi_i + A^i_{22}\,\delta\phi_{n_i} + A^i_{23}\,\delta\phi_{p_i} + A^i_{24} + \\ B^i_{21}\,\delta\psi_{i+1} + B^i_{22}\,\delta\phi_{n_{i+1}}\ ,\end{aligned} \tag{28}$$

and

$$\begin{aligned}\delta\phi_{p_{i-1}} = A^i_{31}\,\delta\psi_i + A^i_{32}\,\delta\phi_{n_i} + A^i_{33}\,\delta\phi_{p_i} + A^i_{34} + \\ B^i_{31}\,\delta\psi_{i+1} + B^i_{33}\,\delta\phi_{p_{i+1}}\ .\end{aligned} \tag{29}$$

The m and k subscripts indicating the iteration step and the time step have been omitted for clarity since it is understood that the correction terms are being evaluated for the same time and iteration step. The A^i_{jk} and B^i_{jk} coefficients are complex functions of position and of the potentials (ψ, ϕ_n, and ϕ_p) at previous time steps and previous iteration steps. The above equations relate the corrections to ψ, ϕ_n, and ϕ_p at spatial point i to the corrections at spatial points i-1 and i+1. The A and B coefficients are slightly different for the time dependent and time independent cases. Exact expressions for the time independent case are given in Appendix B. Expressions have also been derived for the time dependent case [11].

The application of the above equations to a p-n junction is straightforward in principle. However, there are several difficulties which must be overcome before solutions which converge can be obtained. One of the most important of these problems concerns the selection of spatial points at which ψ, ϕ_n, and ϕ_p are calculated. In a p-n junction at low forward bias, most of the changes in ψ, ϕ_n and ϕ_p occur over very small distances, either within the depletion region or for small distances on either side of the depletion region. To achieve accuracy in the numerical calculations, any changes in ψ, ϕ_n, or ϕ_p from one spatial point to another spatial point must be small. This requires that very small steps be employed within space charge regions. On the other hand outside these regions the quantities change much less rapidly and efficient utilization of computer time requires that much larger step sizes be employed. It is necessary then to use a very nonuniform spatial step distribution. Because of this difficulty Fulkerson and Nussbaum [5] in their numerical calculations on a p-n junction divided the device into three regions and used the Debye length as a spatial normalization constant within the depletion region and the diffusion length as a spatial normalization constant outside the depletion region. The approach used in the present work has been to use the same normalized equations throughout, but to generate a nonuniform spatial step distribution.

The generated spatial step size distribution is such that small step sizes are taken within regions of space where ψ, ϕ_n, or ϕ_p are changing rapidly and larger step sizes are taken when these functions change slowly with position. This step size selection process is similar to that developed by De Mari [2]. Since some of the final results (i.e. J_n and J_p) depend upon an integration of the exponential functions of ψ, ϕ_n, and ϕ_p, the criteria on step size is selected so as to maintain a constant relative error within similar numerical integrations. The relative error is defined as the fractional difference between a trapezoidal and a parabolic numerical integration of exponential functions of these variables, and can be set to some convenient value. This in turn can be related to the step size through the radius of curvature of the exponential function [2,11]. At the initialization of an analysis, first order approximations are used for ψ, ϕ_n, and ϕ_p within space charge regions while final data at a prior voltage increment is used in subsequent voltage steps. This allows the step selection to adjust automatically to the changing situation as the applied voltage is incremented. The step selection has been found to be one of the crucial factors in obtaining proper convergence. This becomes particularly apparent in very shallow diffused devices such as solar cells, since the potentials vary through a considerable range within very narrow regions. On the other hand there are basic computer limitations due to round off errors on the minimum size of a step. Thus a proper balance of step size and number of steps in a particular region must be maintained. For a typical device run, calculations can be normally made with 1000±15 steps across a device, with the normalized step sizes ranging from around 10^{-1} near the center of the device to around 10^{-15} near a surface of a shallow diffusion. Double precision is also used in the calculations to extend the range of allowed step sizes.

The coupled difference equations for ψ, ϕ_n and ϕ_p are tridiagonal matrices. A special technique has been developed for solving a tridiagonal matrix [9,12] and in the present work this technique has been extended to the solution of coupled tridiagonal matrices [11]. For given boundary conditions on ψ, ϕ_n, and ϕ_p the solution of the coupled difference equation is a straightforward procedure. In the present work the boundary conditions are $\delta\psi = \delta\phi_n = \delta\phi_p = 0$ at both boundaries of the device since the potentials do not change from one iteration step to the next.

With the aid of the flow diagram in Fig. 3, the general procedure for the analysis of a p-n junction such as shown in Fig. 2 can be summarized. First, information on the device structure such as region widths, doping levels, applied voltage, etc., is used to calculate first order approximations to the potential and quasi-Fermi levels throughout the device. For zero applied diode voltage, the quasi-Fermi levels are constant across the device and the first order approximation to ψ is obtained from standard abrupt junction or linear graded junction theory depending on whether the junction is abrupt or diffused [13]. For applied voltages larger than zero, the first order approximations are taken as the converged solutions at the previously calculated voltage point with the voltage increment linearly added to the previously calculated potentials. The initial approximations are used to develop a step distribution and to obtain values for the A and B coefficients formulated in Appendix B. With these coefficients the linear difference equations are used to calculate corrections to ψ, ϕ_n, and ϕ_p. These corrections are applied to the old values of ψ, ϕ_n, and ϕ_p and the net result continues in the iteration loop to form the basis for a new calculation of the A and B coefficients from which more accurate values of ψ, ϕ_n, and ϕ_p are obtained. The process is repeated until the largest correction on either ψ, ϕ_n, or ϕ_p is less than some previously set quantity (usually 10^{-4} in this work). When the largest correction at any point approaches zero the solutions satisfy the original semiconductor device equations. With ψ, ϕ_n, and ϕ_p known, the carrier and current densities can be evaluated.

The solution for any number of voltage values can be obtained in a single computer run. The number of iterations required at each voltage step is around five when the voltage is stepped in increments of 0.05 volts. A complete forward I-V characteristic can be obtained from 0.0 volts to 0.7 volts in .05 volt increments in about three minutes of total computer time on an IBM 360 computer. Successful runs have been made up to 2 volts applied forward bias; however, the major interest of the present work has been at voltages up to 0.7 volts.

A flow diagram for the time dependent calculations is shown in Fig. 4. The calculations for this case are carried out in a similar manner except that each calculation is for a different point in time. The time increments in the program are similar to the voltage increments in the time independent analysis program. Most of the work has been with the time independent program; however, sufficient calculations have been made to verify that the techniques can be successfully applied to time dependent problems.

IV. EXAMPLES OF COMPUTED RESULTS

The methods outlined in the previous sections have been applied to a wide range of abrupt junction n^+-n-p^+ structures with various doping densities and region widths. Some of the calculated results have been previously reported [14]. As illustrations of the results obtainable from the program, one series of those reported results will be reviewed and more recent work involving p^+-p-n^+ shallow diffused devices will be presented. These were selected in order to illustrate the versatility of these numerical methods over a rather wide range of diode structures.

Calculated data for two types of devices is included in this work. These are, first, an n^+-n-p^+ diode with a lightly doped n region and wide n^+ and p^+ regions. In this device the impurity doping ($N(x)$) is assumed to abruptly change values at the junction interfaces. Other pertinent data on the device is shown in Table III. For this n^+-n-p^+ device the center n region is about a minority carrier diffusion length in width while the n^+ and p^+ regions are considerably wider than a diffusion length. Calculated plots of potential and quasi-Fermi levels are shown in Figs. 5 and 6. The rapid changes in potential at the junction interfaces can be seen in Fig. 5, where the potential change appears as a step in the curves. Due to the scale of presentation the space charge regions appear as steps in the figures even though each region has a substantial number of computational points which can be retrieved <u>via</u> a numerical printout. Although the high injection region was reached as evidenced by the rise in majority concentration of the n type region seen in Fig. 7, the high bias condition was mostly dominated by series resistance as seen from the linear

√

increase of potential within the center region at 0.8 volt bias (Fig. 5). The carrier density curves shown in Fig. 7 are essentially as one would expect from diffusion model calculations. Details of the changes in carrier densities within the space charge regions can again not be seen due to the scale of representation, so this region corresponds to the essentially vertical steps in the carrier densities seen in the figure. The electron and hole quasi-Fermi levels as shown in Fig. 6 are essentially as one would expect from first order device models. As shown in the figure, the quasi-Fermi levels are essentially constant within the depletion region.

The calculated results for a shallow diffused p^+-p-n^+ device are illustrated in Figs. 8-12. The analysis of this device has been undertaken as part of a study of silicon solar cells which is presently in progress [15]. The dimensions and doping densities correspond closely to typical solar cell structures. This device has been studied both without and with optical generation of electron-hole pairs. The potential and quasi-Fermi level plots at various voltage levels for this device are shown in Figs. 8 and 10. Again the changes at the junction interfaces are very abrupt on these scales and appear essentially as vertical lines. The n^+ region is so narrow that no detail of this region can be seen in either Fig. 8 or 10. An expanded view of the potential variations with applied voltage around the p-n^+ junction is shown in Fig. 9. Below high injection in the center region, which occurs at around 0.6 volt, essentially all of the potential change with increased voltage occurs across the p-n^+ junction. For voltages above 0.6 volts approximately half of the increments in terminal voltage appear across the p^+-p junction, as predicted by first order models of diode behavior.

Electron and hole densities are shown in Fig. 11 for the entire device, and an expanded view at the p-n^+ junction is shown in Fig. 12. The boundary condition of an ohmic contact at the surface forces the surface values of p to be independent of applied bias. Expanded views are quite necessary in this device to see any variation of n and p at the p-n^+ junction interface.

This same device was analyzed with the inclusion of a generation rate due to solar irradiance. Fig. 13 illustrates the overall change in the carrier distributions and Fig. 14 expands this data about the n^+-p junction near the irradiated surface. These figures can be compared directly with Figs. 11 and 12. The inclusion of a generation term represents a rather heavy perturbation of the program but it was found quite easy to add the generation rate in steps to an already convergent solution at some high forward bias. After stepping in powers of 2 from Ge/128 to Ge/1 at the same forward bias, the voltage could then be incremented downward in the same fashion as before in order to obtain a full characteristic. Once the program converged with the full generation term, it incremented in voltage to the short circuit condition without any difficulty.

Although no results are shown in this paper, the programs also evaluate the terminal current density at a given voltage, and generates terminal I-V characteristics. The evaluation of current density is straightforward from the device equations after ψ, ϕ_n and ϕ_p are known.

V. SUMMARY

The technique of quasilinearization and the numerical techniques discussed herein have been found to be a very good approach to semiconductor device analysis. The techniques have been found to lead to rapidly converging solutions under a wide variety of physical conditions. These cover the range of devices which are narrow compared to the minority carrier diffusion length to devices which are very wide compared to the minority carrier diffusion length. The approach is also able to very easily handle high injection effects in p-n junctions, high-low junctions, and optical generation. The exact analysis is providing very useful information on the operation of solar cells. With the analysis program a much more complete understanding is possible of solar cell operation and especially of the interactions between p-n junctions and high-low junctions in solar cell structures [15].

The results reported herein are but a small sample of the computed results which have been obtained on semiconductor devices. The included results illustrate the application of the program to two physically very different diode structures. The analysis program is able to analyze both types of devices with only minor changes in input parameters.

VI. ACKNOWLEDGEMENTS

The authors would like to acknowledge the partial support of this work by the National Science Foundation through NSF Grant GK-13752 and the National Aeronautics and Space Administration through NASA grant NGR 34-002-195.

100

Table 1 Normalization table

Normalized Quantity	Description	Normalization Factor
x	position coordinate	L_D $(=\sqrt{\epsilon V_t/qn_i})$
t	time coordinate	L_D^2/D_o
τ_{no}, τ_{po}	lifetimes	L_D^2/D_o
ψ	electrostatic potential	V_t $(= kT/q)$
ϕ_n, ϕ_p	quasi-Fermi levels	V_t
V_A	applied (or terminal) voltage	V_t
E	electric field	V_t/L_D
n,p	carrier densities	n_i
N, N_D, N_A	net impurity, donor, and acceptor densities	n_i
J, J_n, J_p	total, electron, and hole current densities	$-qD_on_i/L_D$
D_n, D_p	carrier diffusion constants	D_o $(= 1\ \text{cm}^2/\text{sec})$
μ_n, μ_p	carrier mobilities	D_o/V_t
U	generation-recombination rate	D_on_i/L_D^2
G_e	external generation rate	D_on_i/L_D^2

/101/

Table II. Constants for mobility expressions (normalized values)

C_1	81	K_1	350
C_2	$2.16\text{x}10^8$	K_2	$7.0\text{x}10^8$
C_3	$1.76\text{x}10^{-6}$	K_3	$1.93\text{x}10^{-6}$
C_4	$1.70\text{x}10^4$	K_4	$1.76\text{x}10^4$
C_5	$1.25\text{x}10^4$	K_5	$1.18\text{x}10^4$
μ_{no}^{-1}	34.93	μ_{po}^{-1}	12.42

Table III. Data on two diode types studied

	n^+-n-p^+ Device	p^+-p-n^+ Device (Solar Cell)	
n^+ doping	$10^{18}/cm^3$	p^+ doping	$10^{18}/cm^3$
n doping	$2.5x10^{15}/cm^3$	p doping	$1.3x10^{15}/cm^3$
p^+ doping	$10^{18}/cm^3$	n^+ doping*	$10^{20}/cm^3$
n^+ width	250 μm	p^+ width	0.5 μm
n width	100 μm	p width	249.25 μm
p^+ width	250 μm	n^+ width	0.25 μm
τ_{po}	10^{-7} sec	τ_{po}	10^{-7} sec
τ_{no}	10^{-6} sec	τ_{no}	10^{-4} sec

*n^+ region is a Gaussian diffused region. The value of doping density is the density at the surface.

APPENDIX A

The quasilinearization or Newton-Raphson approach to nonlinear problems was first introduced by Bellman [9], extended by Kalaba [10] and applied to many engineering problems by Lee [11]. To illustrate the mechanics of the technique, consider the equation

$$L[X(t)] = g(X,t) \tag{A-1}$$

where L is a linear operator (partial or ordinary) operating on the desired function X(t) and g is some nonlinear function of X. Performing a Taylor series expansion of the nonlinear function about a given initial estimate $X_o(t)$, one obtains

$$L[X(t)] = g(X_o,t) + (X-X_o)\ g'(X_o,t) + \text{-----} \tag{A-2}$$

where the prime indicates differentiation with respect to X. Neglecting second and higher order terms of the expansion, Eq. (A-2) becomes

$$L[X(t)] = g(X_o,t) + (X-X_o)\ g'(X_o,t), \tag{A-3}$$

which is a linear equation which can be solved for $X(t) = X_1(t)$. Using this result to formulate

$$L[X_2(t)] = g(X_1,t) + (X_2-X_1)\ g'(X_1,t), \tag{A-4}$$

the iterative process can be continued until the desired solution X(t) is obtained. Of course, this procedure assumes convergence of the sequence of functions $\{X_m\}$. Although at first this seems to be a rather severe restriction, for many of the commonly occurring linear operators, the sequence does indeed converge. In fact, for all functions attempted by the authors, convergence was accomplished. It should also be noted that if convergence does occur, then this convergence is quadratic in nature [9,11]. That is, as convergence is approached, the maximum error (or correction) in a given iteration is proportional to the square of the maximum error of the previous iteration.

In summary, the quasilinearization technique is essentially a Taylor Series expansion (in function space) of the nonlinear portion about each of the individual functions making up the nonlinearity. The resulting linear equation is then solved in an iterative fashion subject to the boundary conditions imposed by physical considerations. As evidenced by the equations in the body of this paper, the quasilinearization technique is applicable to multi-dimensional and multi-functional nonlinear equations.

APPENDIX B

Expressions for the A and B Coefficients for the Time Independent Case.

$$A_{11}^{i} = \left[\frac{\alpha_{i+1}}{\alpha_i} + \frac{s_{i-1}}{2}\,(s_i+s_{i-1})\,\left.\frac{\partial F_1}{\partial \psi}\right|_i\right], \qquad \text{(B-1)}$$

$$A_{12}^{i} = \frac{s_{i-1}}{2}\,(s_i+s_{i-1})\,\left.\frac{\partial F_1}{\partial \phi_n}\right|_i , \qquad \text{(B-2)}$$

$$A_{13}^{i} = \frac{s_{i-1}}{2}\,(s_i+s_{i-1})\,\left.\frac{\partial F_1}{\partial \phi_p}\right|_i , \qquad \text{(B-3)}$$

$$A_{14}^{i} = \left[\frac{s_{i-1}}{2}\,(s_i+s_{i-1})(F_1-\psi'')_i\right], \qquad \text{(B-4)}$$

$$B_{11}^{i} = -1/\alpha_i , \qquad \text{(B-5)}$$

$$A_{21}^{i} = \left(\frac{s_i}{2+s_i\left.\frac{\partial F_2}{\partial \phi_n'}\right|_i}\right)\left\{\frac{s_i+s_{i-1}}{\alpha_i}\left.\frac{\partial F_2}{\partial \psi}\right|_i + \left(\frac{\alpha_{i-1}^2}{\alpha_i^2} - A_{11}^{i}\right)\left.\frac{\partial F_2}{\partial \psi'}\right|_i\right\}, \qquad \text{(B-6)}$$

$$A_{22}^{i} = \left(\frac{s_i}{2+s_i\left.\frac{\partial F_2}{\partial \phi_n'}\right|_i}\right)\left\{\frac{s_i+s_{i-1}}{\alpha_i}\left.\frac{\partial F_2}{\partial \phi_n}\right|_i + \frac{2(\alpha_i+1)}{s_i\alpha_i} + \right.$$

$$\left.\frac{\alpha_{i-1}^2}{\alpha_i^2}\left.\frac{\partial F_2}{\partial \phi_n'}\right|_i - A_{12}^{i}\left.\frac{\partial F_2}{\partial \psi'}\right|_i\right\}, \qquad \text{(B-7)}$$

$$A^{i}_{23} = \frac{s_i(s_i+s_{i-1})}{2 + s_i \left.\frac{\partial F_2}{\partial \phi'_n}\right|_i} \left\{ \left.\frac{\partial F_2}{\partial \phi_p}\right|_i - \frac{s_i}{2} \left.\frac{\partial F_1}{\partial \phi_p}\right|_i \left.\frac{\partial F_2}{\partial \psi'}\right|_i \right\} , \tag{B-8}$$

$$A^{i}_{24} = \frac{s_i(s_i+s_{i-1})}{2 + s_i \left.\frac{\partial F_2}{\partial \phi'_n}\right|_i} \left\{ [F_2-\phi''_n]_i - \frac{s_i}{2} [F_1-\psi''] \left.\frac{\partial F_2}{\partial \psi'}\right|_i \right\} , \tag{B-9}$$

$$B^{i}_{21} = [s_{i-1}(\frac{\alpha_{i+1}}{\alpha_i}) \left.\frac{\partial F_2}{\partial \psi'}\right|_i] \; / \; [2 + s_i \left.\frac{\partial F_2}{\partial \phi'_n}\right|_i] , \tag{B-10}$$

$$B^{i}_{22} = s_{i-1}[\frac{1}{\alpha_i} \left.\frac{\partial F_2}{\partial \phi'_n}\right|_i - \frac{2}{s_i}] \; / \; [2 + s_i \left.\frac{\partial F_2}{\partial \phi'_n}\right|_i] , \tag{B-11}$$

$$A^{i}_{31} = (\frac{s_i}{2 + s_i \left.\frac{\partial F_3}{\partial \phi'_p}\right|_i}) \left\{ \frac{s_i+s_{i-1}}{\alpha_i} \left.\frac{\partial F_3}{\partial \psi}\right|_i + \right.$$

$$\left. (\frac{\alpha_i^2-1}{\alpha_i^2}) \left.\frac{\partial F_3}{\partial \psi'}\right|_i - A^{i}_{11} \left.\frac{\partial F_3}{\partial \psi'}\right|_i \right\} , \tag{B-12}$$

$$A^{i}_{32} = (\frac{s_{i-1}(s_i+s_{i-1})}{2 + s_i \left.\frac{\partial F_3}{\partial \phi'_p}\right|_i}) \left\{ \left.\frac{\partial F_3}{\partial \phi_n}\right|_i - \frac{s_i}{2} \left.\frac{\partial F_1}{\partial \phi_n}\right|_i \left.\frac{\partial F_3}{\partial \psi'}\right|_i \right\} , \tag{B-13}$$

$$A^{i}_{33} = (\frac{s_i}{2 + s_i \left.\frac{\partial F_3}{\partial \phi'_p}\right|_i}) \left\{ \frac{s_i + s_{i-1}}{\alpha_i} \left.\frac{\partial F_3}{\partial \phi_p}\right|_i + \frac{2(\alpha_{i+1})}{\alpha_i s_i} + \right.$$

$$\left. (\frac{\alpha_{i-1}^2}{\alpha_i^2}) \left.\frac{\partial F_3}{\partial \phi'_p}\right|_i - A^{i}_{13} \left.\frac{\partial F_3}{\partial \psi}\right|_i \right\} , \tag{B-14}$$

$$A^{i}_{34} = \left(\frac{s_{i-1}(s_i+s_{i-1})}{2 + s_i \left.\frac{\partial F_3}{\partial \phi_p'}\right|_i}\right) \left\{ [F_3-\phi_p'']_i - \frac{s_i}{2}\,[F_1-\psi'']_i \left.\frac{\partial F_3}{\partial \psi'}\right|_i \right\} , \tag{B-15}$$

$$B^{i}_{31} = \left[s_{i-1}\left(\frac{\alpha_{i+1}}{\alpha_i}\right) \left.\frac{\partial F_3}{\partial \psi'}\right|_i \right] \Big/ \left[2 + s_i \left.\frac{\partial F_3}{\partial \phi_p'}\right|_i \right] , \tag{B-16}$$

$$B^{i}_{33} = \left[\frac{s_{i-1}}{2 + s_i \left.\frac{\partial F_3}{\partial \phi_p'}\right|_i}\right] \left[\frac{1}{\alpha_i} \left.\frac{\partial F_3}{\partial \phi_p'}\right|_i - \frac{2}{s_i}\right] . \tag{B-17}$$

In the above equations s_i is the magnitude of the step in going from x_i to x_{i+1} and α_i is the ratio of s_i to s_{i-1}. Expressions for the various partial derivatives of F_1, F_2, and F_3 are given in the following tables:

Table B.1 Partial derivatives of F_1

$$F_1(\psi,\ \phi_n,\ \phi_p) = \exp[\psi-\phi_n] - \exp[\phi_p-\psi] - N(x)$$

$$\frac{\partial F_1}{\partial \psi} = \exp[\psi-\phi_n] + \exp[\phi_p-\psi]$$

$$\frac{\partial F_1}{\partial \phi_n} = -\exp[\psi-\phi_n]$$

$$\frac{\partial F_1}{\partial \phi_p} = -\exp[\phi_p-\psi]$$

Table B.2 Partial derivatives of F_2

$$F_2(\psi,\phi_n,\phi_p,\psi',\phi_n') = \left[\frac{d\phi_n}{dx} + \frac{1}{\gamma_n}\frac{d\gamma_n}{dx} - \frac{d\psi}{dx}\right]\frac{d\phi_n}{dx} + \gamma_n(x)G_e(x)\exp(\phi_n-\psi)$$

$$+ \quad \gamma_n(x)\,\frac{\exp[\phi_n-\psi] - \exp[\phi_p-\psi]}{\tau_{po}[1+\exp(\psi-\phi_n)]+\tau_{no}[1+\exp(\phi_p-\psi)]}$$

$$\frac{\partial F_2}{\partial\psi} = \gamma_n(x)\,\frac{(\tau_{no}+\tau_{po})[\exp(\phi_p-\psi) - \exp(\phi_n-\psi)] + 2\tau_{po}[\exp(\phi_p-\phi_n)-1]}{\{\tau_{po}[1+\exp(\psi-\phi_n)] + \tau_{no}[1+\exp(\phi_p-\psi)]\}^2}$$

$$-\gamma_n(x)G_e(x)\exp(\phi_n-\psi)$$

$$\frac{\partial F_2}{\partial\phi_n} = \gamma_n(x)\,\frac{(\tau_{no} + \tau_{po})\exp(\phi_n-\psi) + \tau_{no}\exp(\phi_n+\phi_p-2\psi) + \tau_{po}[2-\exp(\phi_p-\phi_n)]}{\{\tau_{po}[1+\exp(\psi-\phi_n)] + \tau_{no}[1+\exp(\phi_p-\psi)]\}^2}$$

$$+\gamma_n(x)G_e(x)\exp(\phi_n-\psi)$$

$$\frac{\partial F_2}{\partial\phi_p} = -\,\gamma_n(x)\,\frac{(\tau_{no}+\tau_{po})\exp(\phi_p-\psi) + \tau_{po}\exp(\phi_p-\phi_n) + \tau_{no}\exp(\phi_n+\phi_p-2\psi)}{\{\tau_{po}[1+\exp(\psi-\phi_n)] + \tau_{no}[1+\exp(\phi_p-\psi)]\}^2}$$

$$\frac{\partial F_2}{\partial\psi'} = -\,\frac{d\phi_n(x)}{dx}$$

$$\frac{\partial F_2}{\partial\phi_n'} = \frac{1}{\gamma_n(x)}\,\frac{d\gamma_n(x)}{dx} + 2\,\frac{d\phi_n(x)}{dx} - \frac{d\psi(x)}{dx}$$

Table B.3 Partial derivatives of F_3

$$F_3(\psi,\phi_n,\phi_p,\psi',\phi_p') = \left[\frac{d\psi}{dx} + \frac{1}{\gamma_p}\frac{d\gamma_p}{dx} - \frac{d\phi_p}{dx}\right]\frac{d\phi_p}{dx} - \gamma_p(x)G_e(x)\exp(\psi-\phi_p)$$

$$+ \quad \gamma_p(x)\,\frac{\exp(\psi-\phi_n) - \exp(\psi-\phi_p)}{\tau_{po}[1+\exp(\psi-\phi_n)] + \tau_{no}[1+\exp(\phi_p-\psi)]}$$

$$\frac{\partial F_3}{\partial \psi} = \gamma_p(x)\,\frac{(\tau_{no}+\tau_{po})[\exp(\psi-\phi_n) - \exp(\psi-\phi_p)] + 2\tau_{no}[\exp(\phi_p-\phi_n)-1]}{\left\{\tau_{po}[1+\exp(\psi-\phi_n)] + \tau_{no}[1+\exp(\phi_p-\psi)]\right\}^2}$$

$$-\gamma_p(x)G_e(x)\exp(\psi-\phi_p)$$

$$\frac{\partial F_3}{\partial \phi_n} = -\gamma_p(x)\,\frac{(\tau_{no}+\tau_{po})\exp(\psi-\phi_n) + \tau_{no}\exp(\phi_p-\phi_n) + \tau_{po}\exp(2\psi-\phi_n-\phi_p)}{\left\{\tau_{po}[1+\exp(\psi-\phi_n)] + \tau_{no}[1+\exp(\phi_p-\psi)]\right\}^2}$$

$$\frac{\partial F_3}{\partial \phi_p} = \gamma_p(x)\,\frac{(\tau_{no}+\tau_{po})\exp(\psi-\phi_p) + \tau_{po}\exp(2\psi-\phi_n-\phi_p) + \tau_{no}[2-\exp(\phi_p-\phi_n)]}{\left\{\tau_{po}[1+\exp(\psi-\phi_n)] + \tau_{no}[1+\exp(\phi_p-\psi)]\right\}^2}$$

$$+\gamma_p(x)G_e(x)\exp(\psi-\phi_p)$$

$$\frac{\partial F_3}{\partial \psi'} = \frac{d\phi_p(x)}{dx}$$

$$\frac{\partial F_3}{\partial \phi_p'} = \frac{1}{\gamma_p}\;\frac{d\gamma_p(x)}{\gamma_p} + \frac{d\psi(x)}{dx} - 2\,\frac{d\phi_p(x)}{dx}$$

REFERENCES

1. H. K. Gummel, IEEE Trans. on ED, ED-11, 455 (1964).
2. A. De Mari, Ph.D. Thesis, California Institute of Technology (1967).
3. C. M. Lee, R. J. Lomax, and G. I. Haddad, IEEE Trans. on MTT, MTT-22 160 (1974).
4. M. S. Mock, Solid-State Electronics, 15, 1 (1972).
5. D. E. Fulkerson and A. Naussbaum, Solid State Electronics, 9, 709-719 (1966).
6. C. W. Gwyn, D. L. Scharfetter, and J. L. Wirth, IEEE Trans. on NS, NS-14, 153 (1967).
7. R. E. Bellman, Proc. Natn. Acad. Sci. U.S.A., 41, 743 (1955).
8. R. Kalaba, J. Math. Mech., 8, 519 (1959).
9. E. S. Lee, "Quasilinearization and Invarient Imbedding", Academic Press, New York (1968).
10. J. Crank and P. Nicolson, Proceedings of the Cambridge Philosophical Society, 43 (1), 50 (1947).
11. E. D. Graham, Ph.D. Thesis, N. C. State University, Raleigh, N. C., (1970).
12. G. H. Bruce, D. W. Peaceman, H. H. Rochford and J. D. Rice, Trans. AIME 198, 79 (1953).
13. S. M. Sze, "Physics of Semiconductor Devices", Wiley, 1969.
14. E. D. Graham and J. R. Hauser, Solid State Electronics, 15, 303-310 (1972).
15. Complete details of this work will be published elsewhere.

///

FIGURE CAPTIONS

Figure 1. Spatial dependence of electron-hole pair generation rate for full spectrum (AMO) irradiance on silicon.

Figure 2. The basic n^+-n-p^+ (or p^+-p-n^+) diode structure.

Figure 3. Flow diagram of semiconductor device analysis program (Time independent case).

Figure 4. Flow diagram of semiconductor device analysis program (Time dependent case).

Figure 5. Electrostatic potential variation in n^+-n-p^+ device.

Figure 6. Quasi-Fermi potential variation in n^+-n-p^+ device (measured above equilibrium value of -0.466v).

Figure 7. Hole and electron density variation in n^+-n-p^+ device.

Figure 8. Electrostatic potential variation in p^+-p-n^+ device.

Figure 9. Electrostatic potential variation about n^+-p junction.

Figure 10. Quasi-Fermi potential variation in p^+-p-n^+ device (measured below equilibrium value of 0.466v).

Figure 11. Hole and electron density variation in p^+-p-n^+ device.

Figure 12. Hole and electron density variation about n^+-p junction.

Figure 13. Hole and electron density variation in p^+-p-n^+ device under full spectral irradiance (Irradiated surface at x = 250 microns).

Figure 14. Hole and electron concentration about n^+-p junction near irradiated surface.

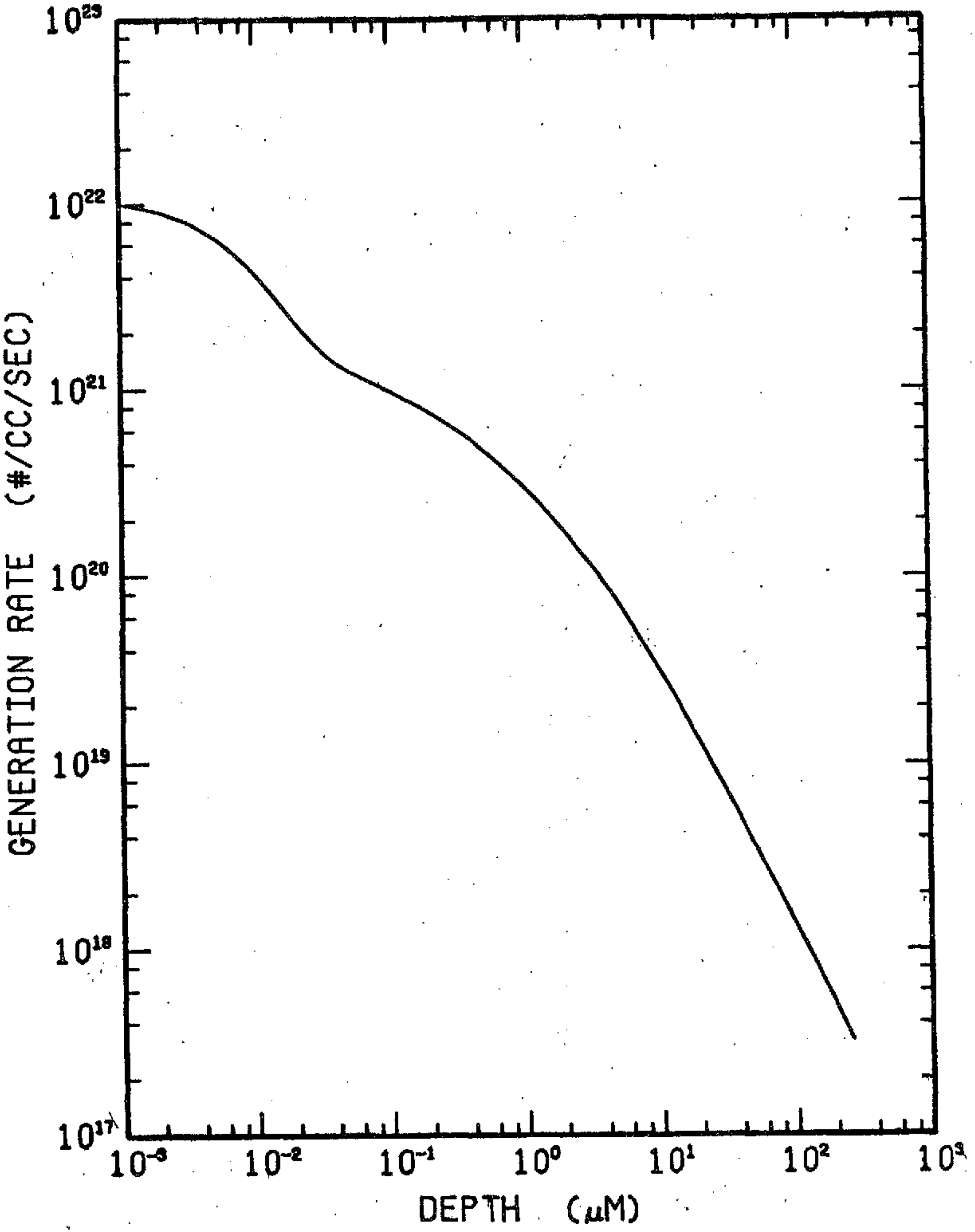

Figure 1. Spatial dependence of electron-hole pair generation rate for full spectrum (AMO) irradiance on silicon.

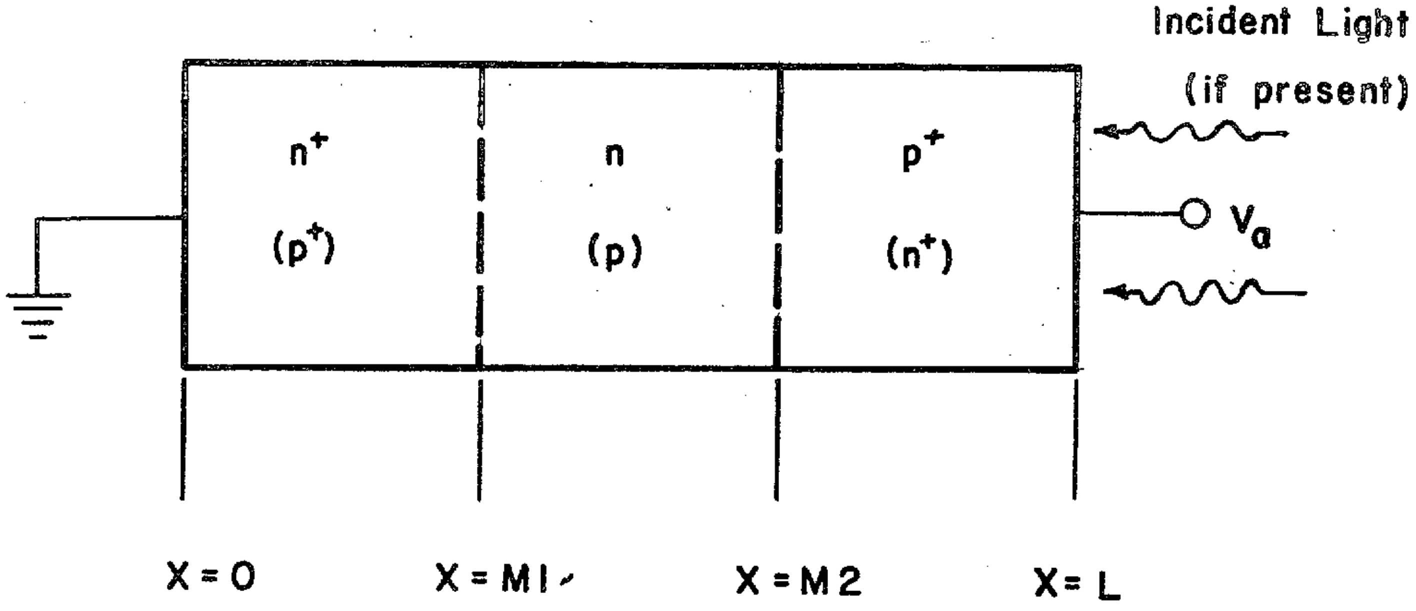

Figure 2. The basic n^+-n-p^+ (or p^+-p-n^+) diode structure.

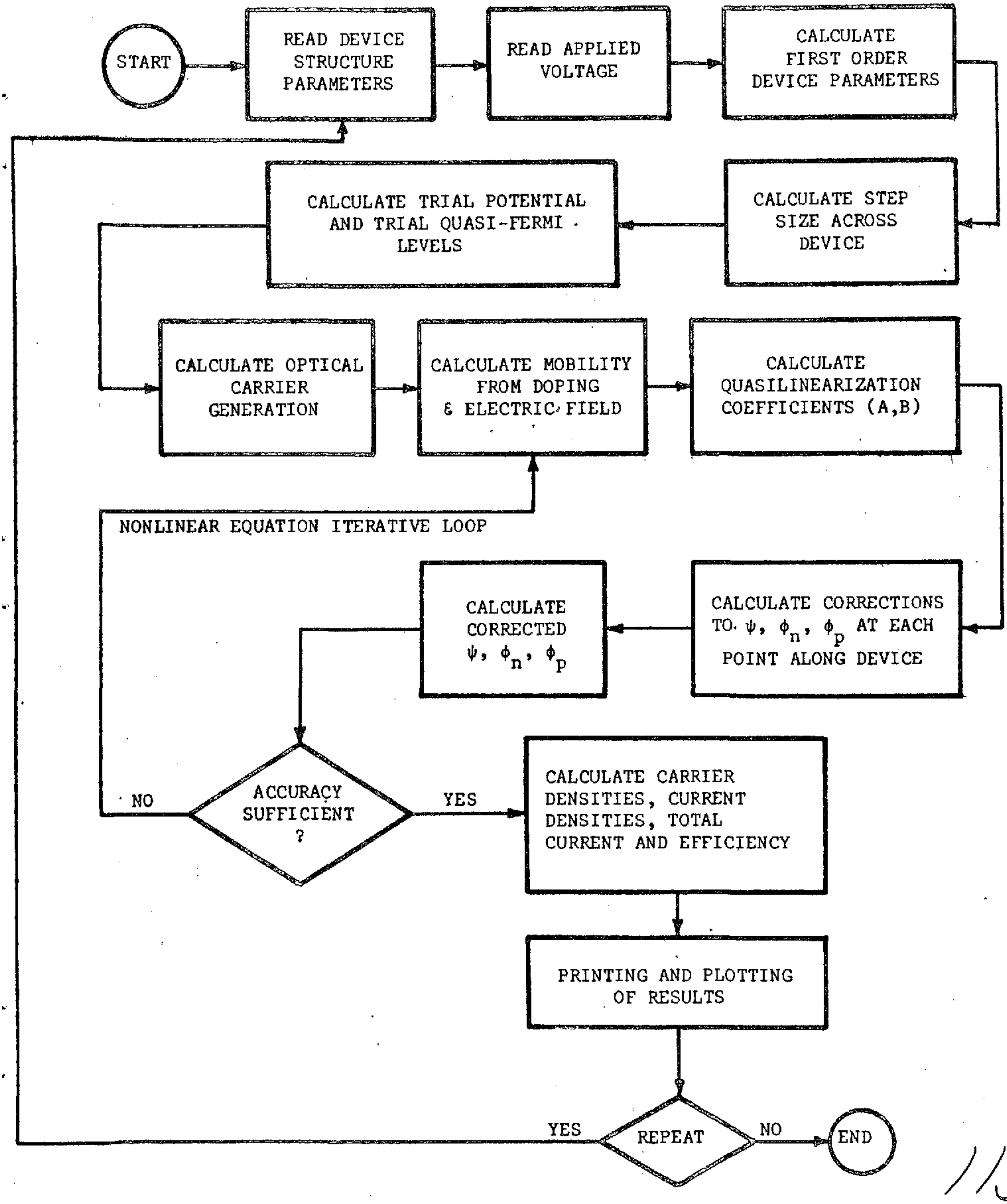

Figure 3. Flow diagram of semiconductor device analysis program (Time independent case).

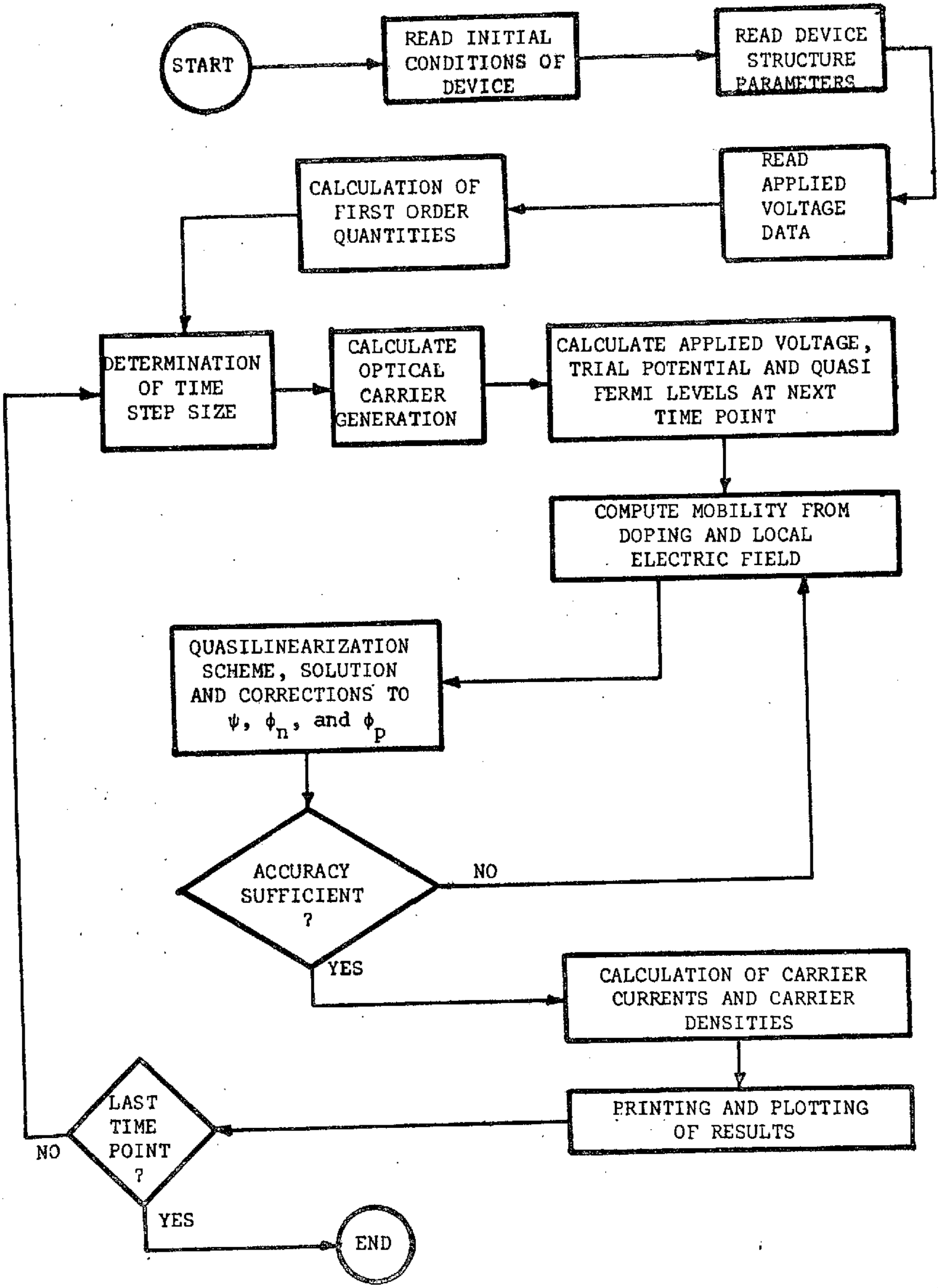

Figure 4. Flow diagram of semiconductor device analysis program (Time dependent case).

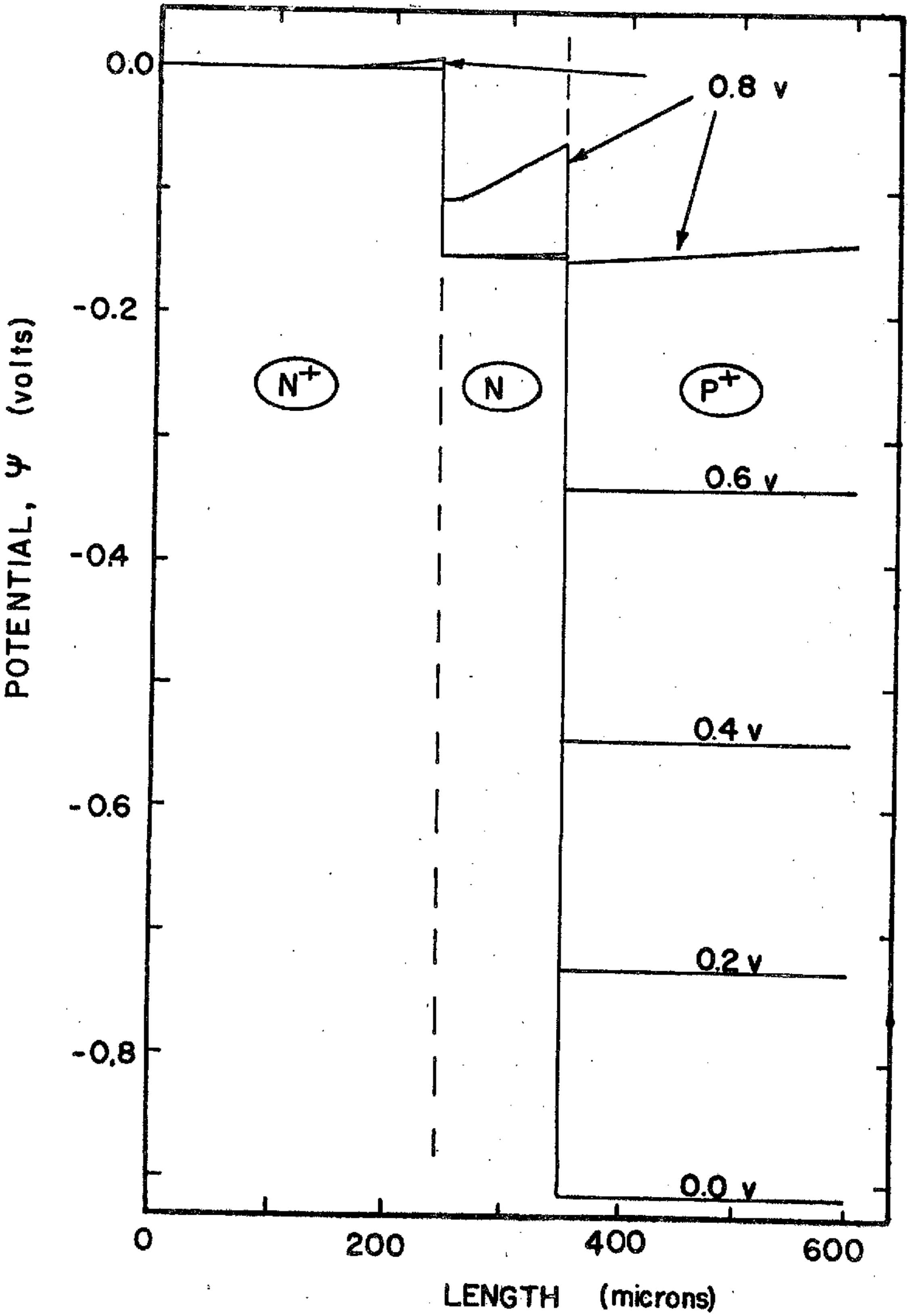

Figure 5. Electrostatic potential variation in n^+-n-p^+ device.

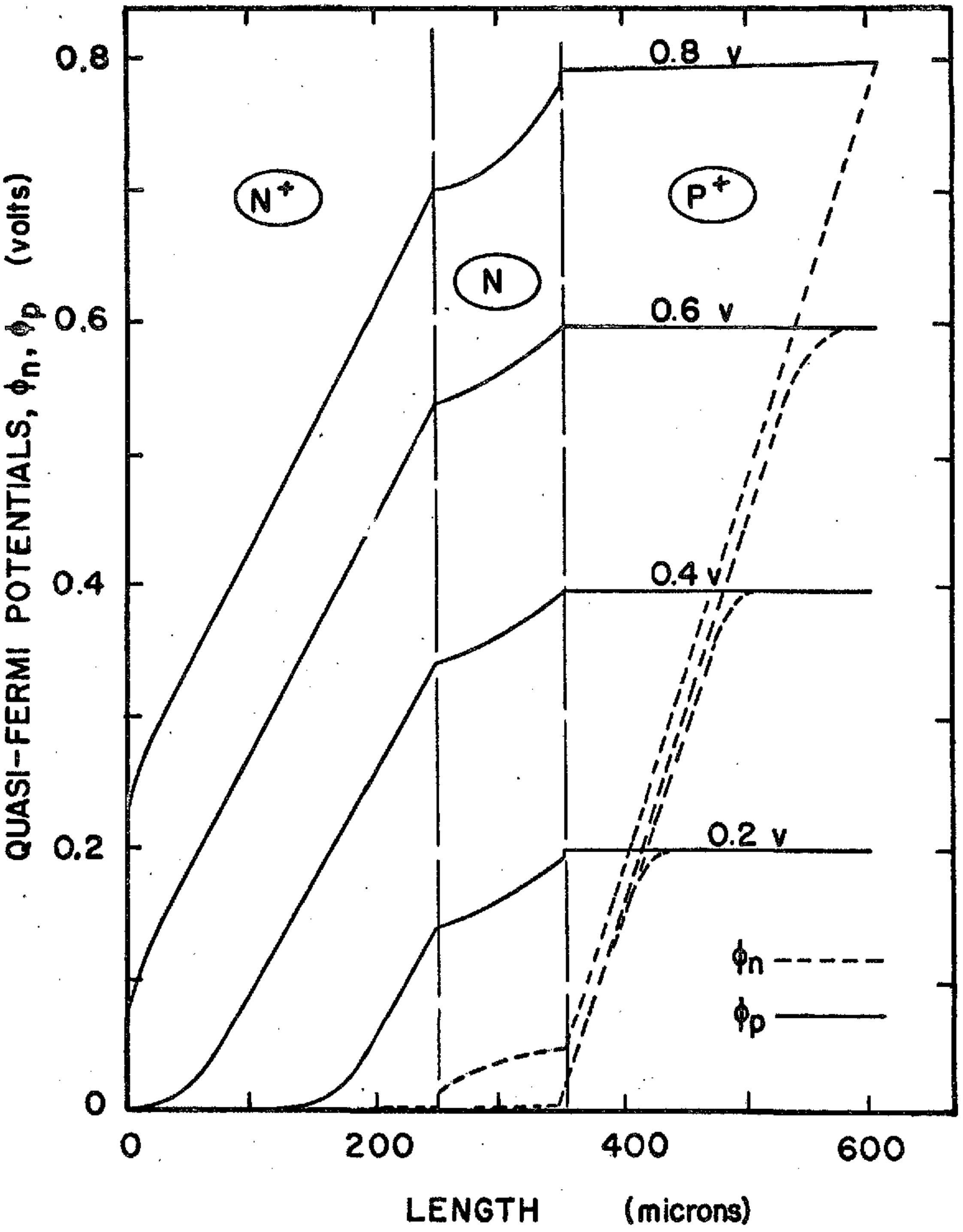

Figure 6. Quasi-Fermi potential variation in n^+-n-p^+ device (measured above equilibrium value of -0.466v).

118

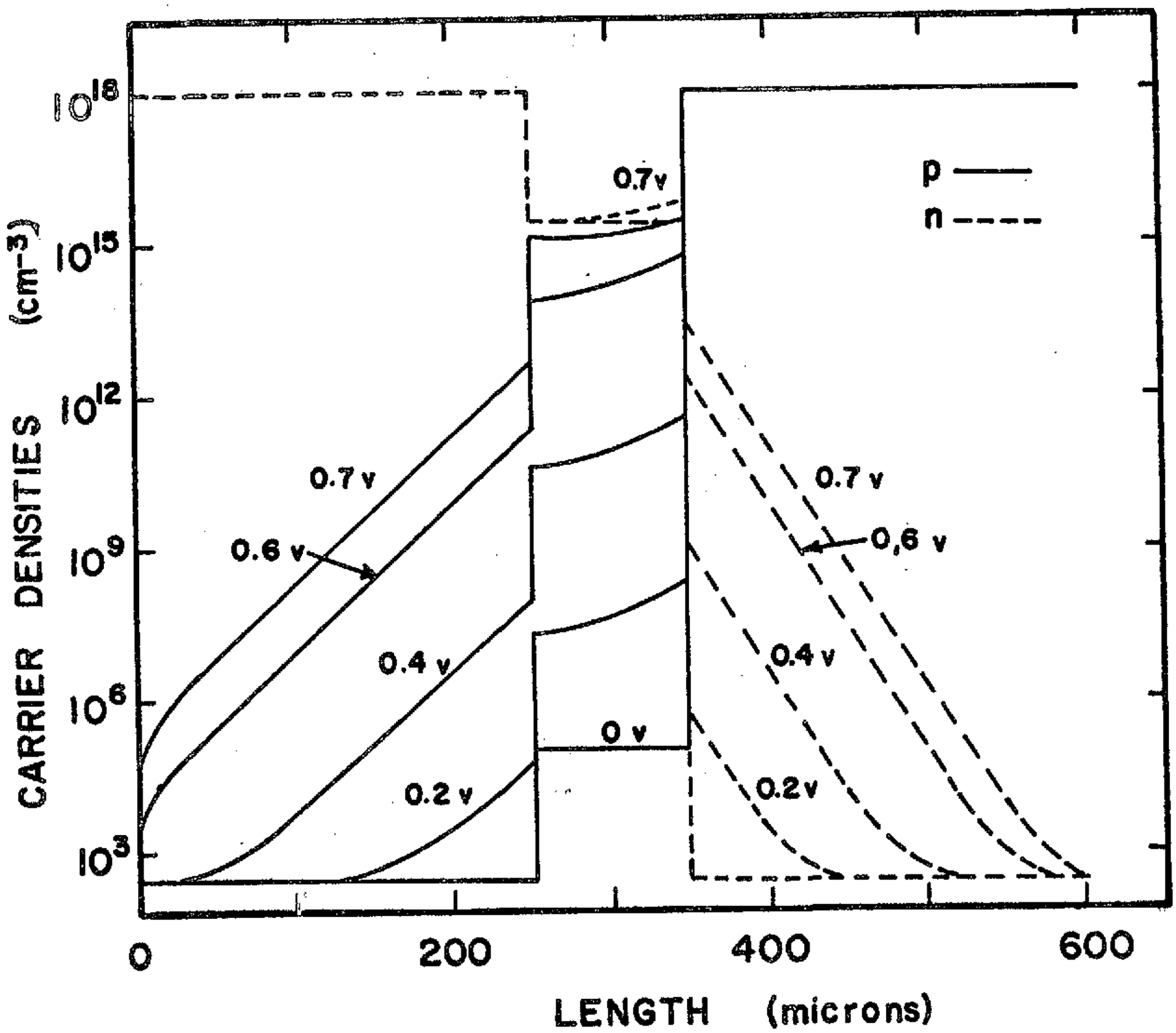

Figure 7. Hole and electron density variation in n^+-n-p^+ device.

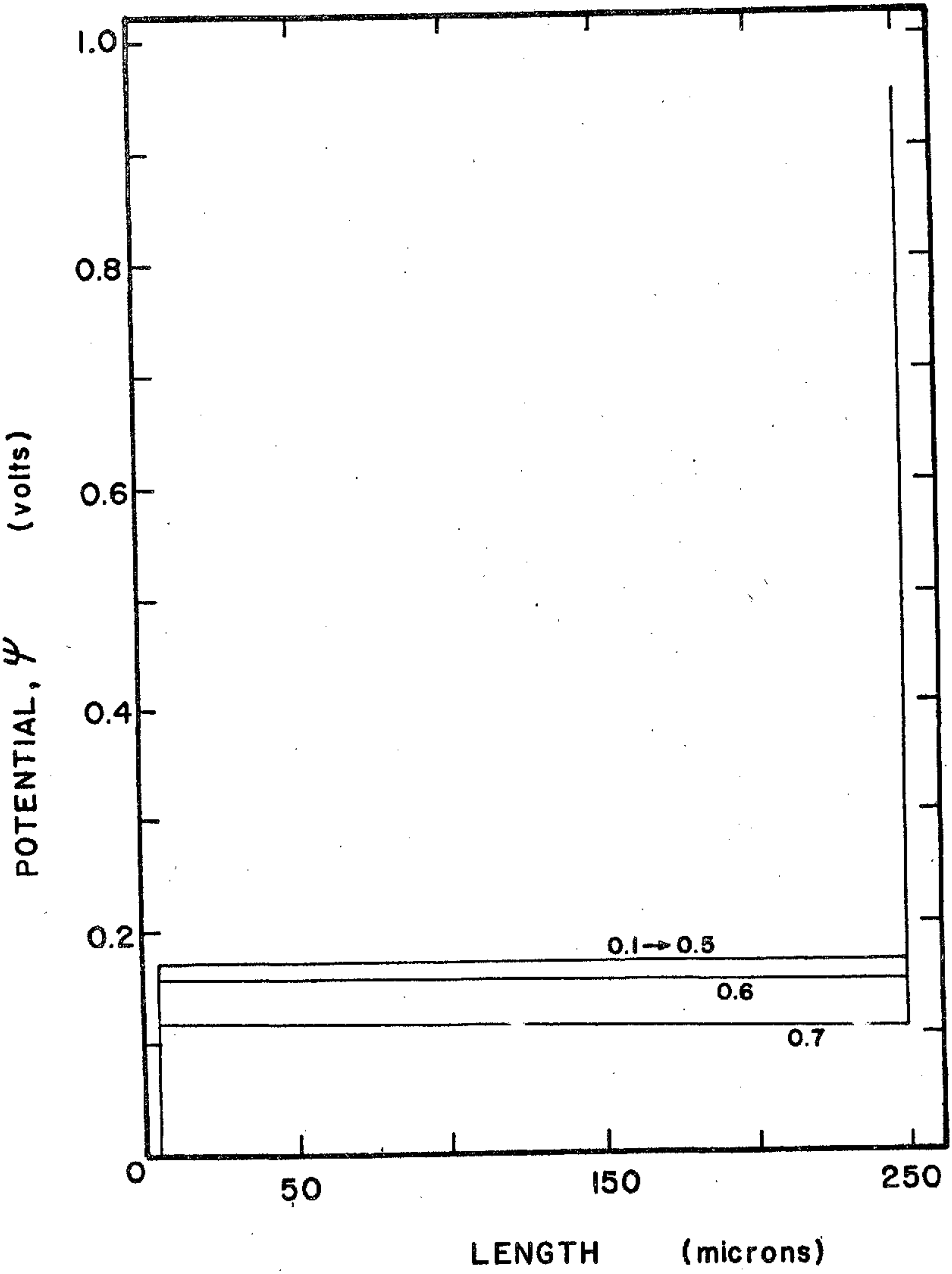

Figure 8. Electrostatic potential variation in p^+-p-n^+ device.

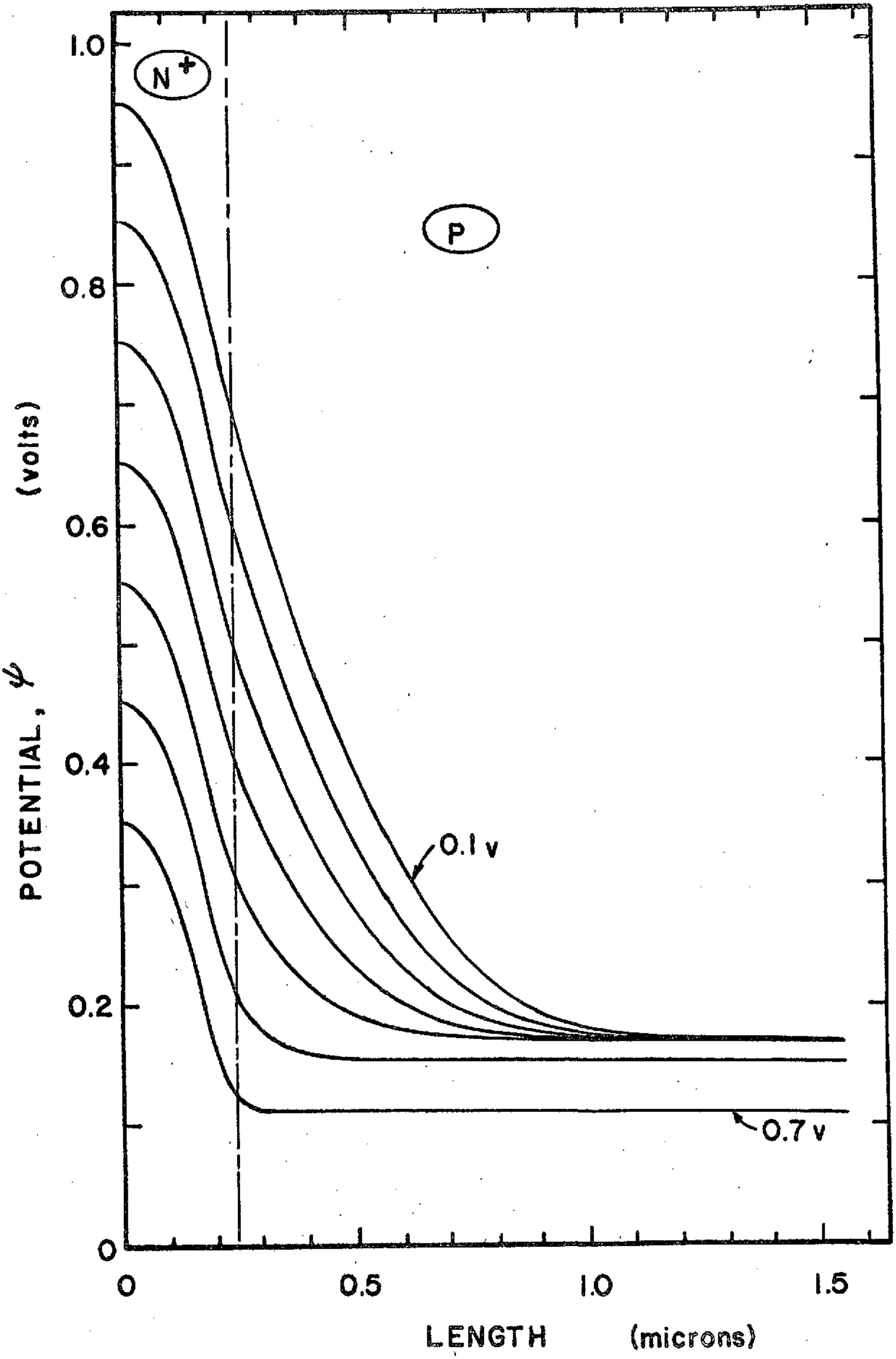

Figure 9. Electrostatic potential variation about n^+-p junction.

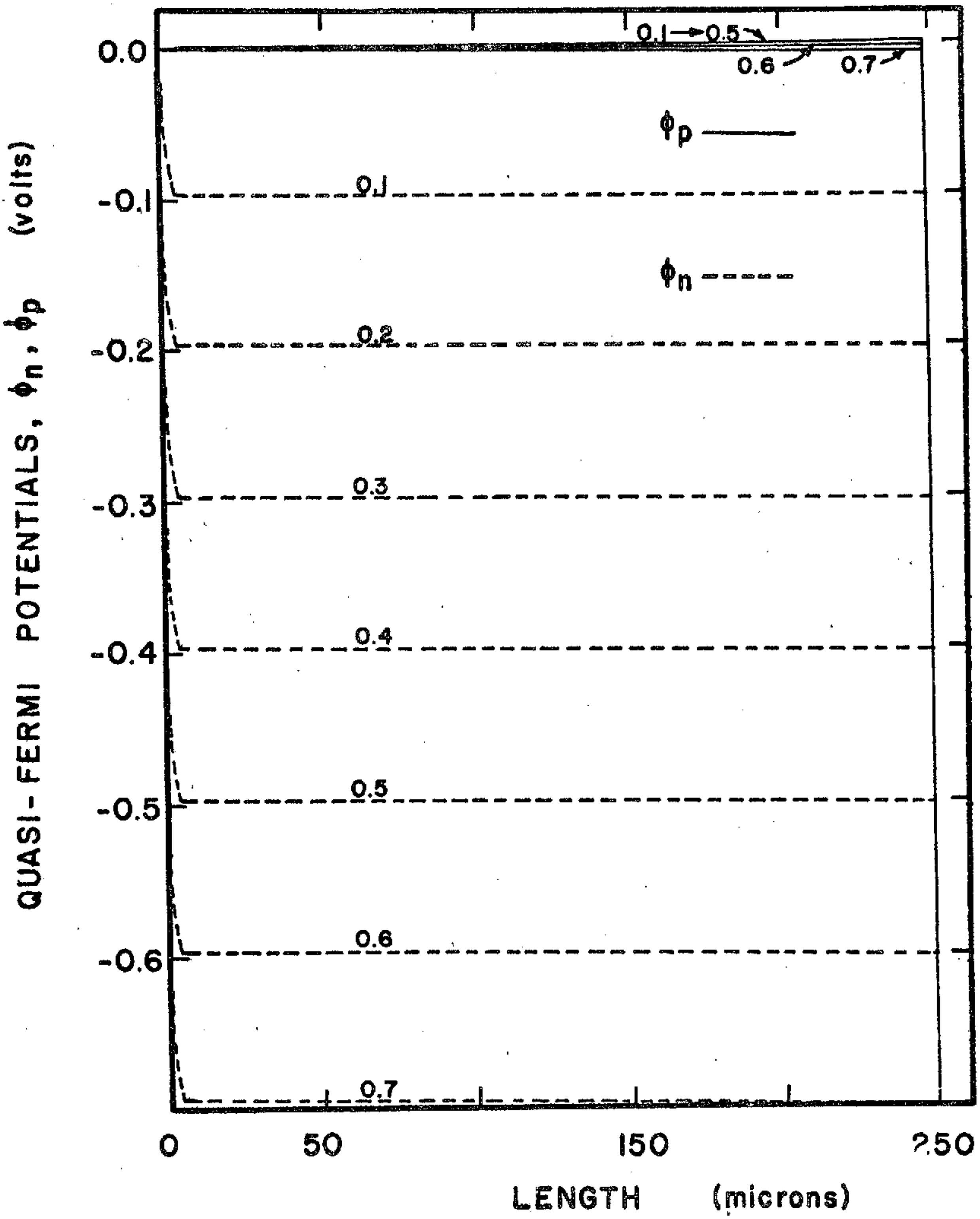

Figure 10. Quasi-Fermi potential variation in p^+-p-n^+ device (measured below equilibrium value of 0.466v).

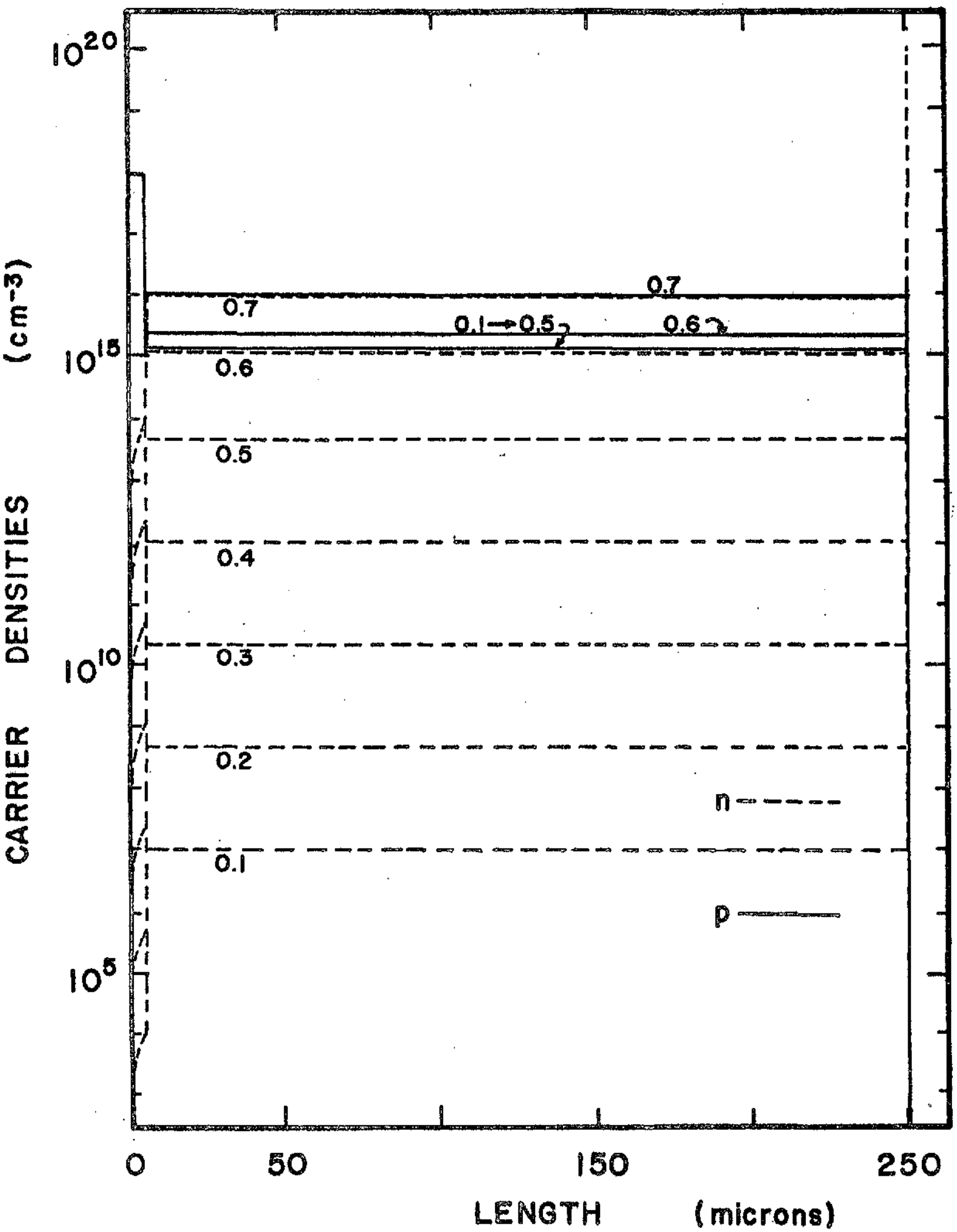

Figure 11. Hole and electron density variation in p^+-p-n^+ device.

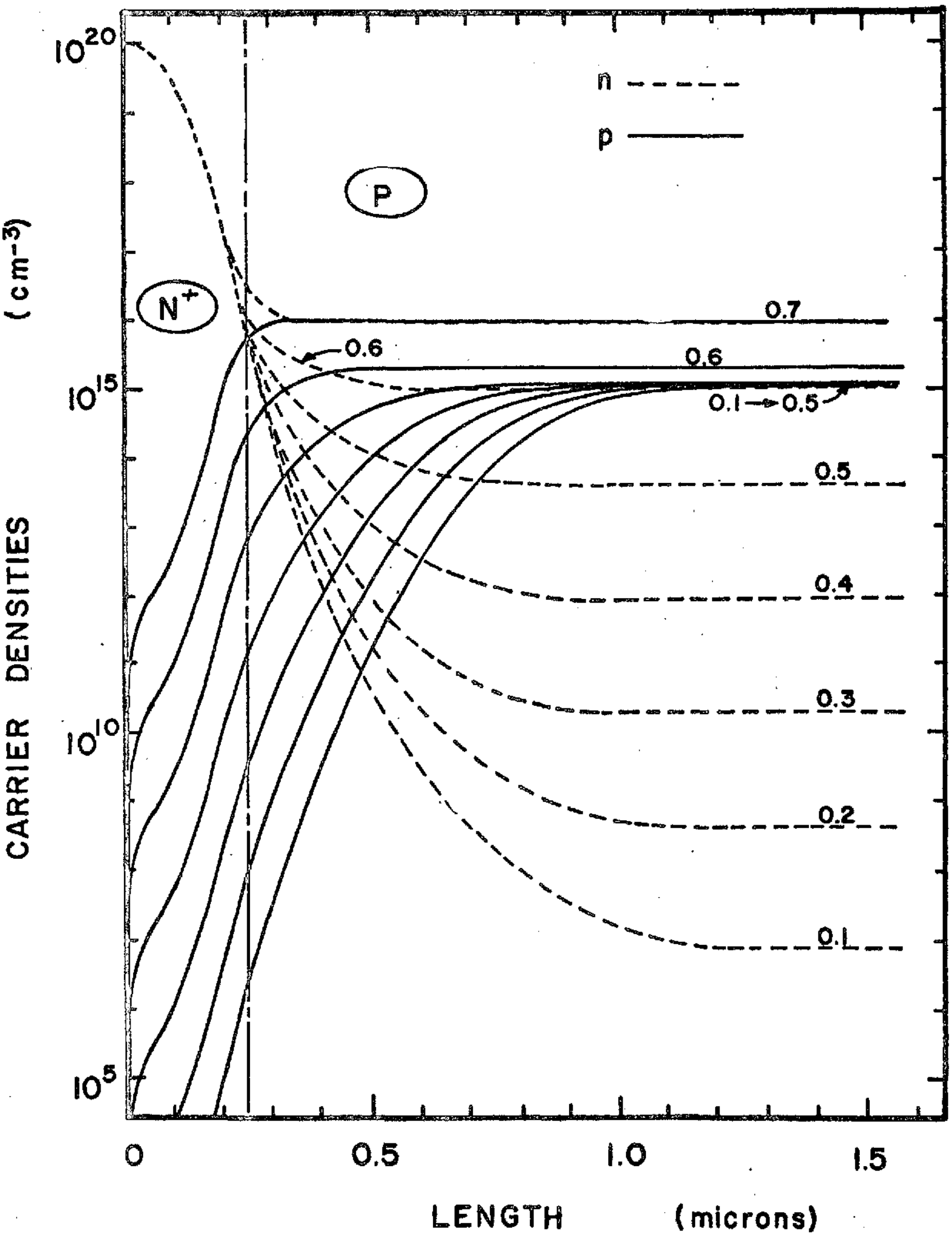

Figure 12. Hole and electron density variation about n^+-p junction.

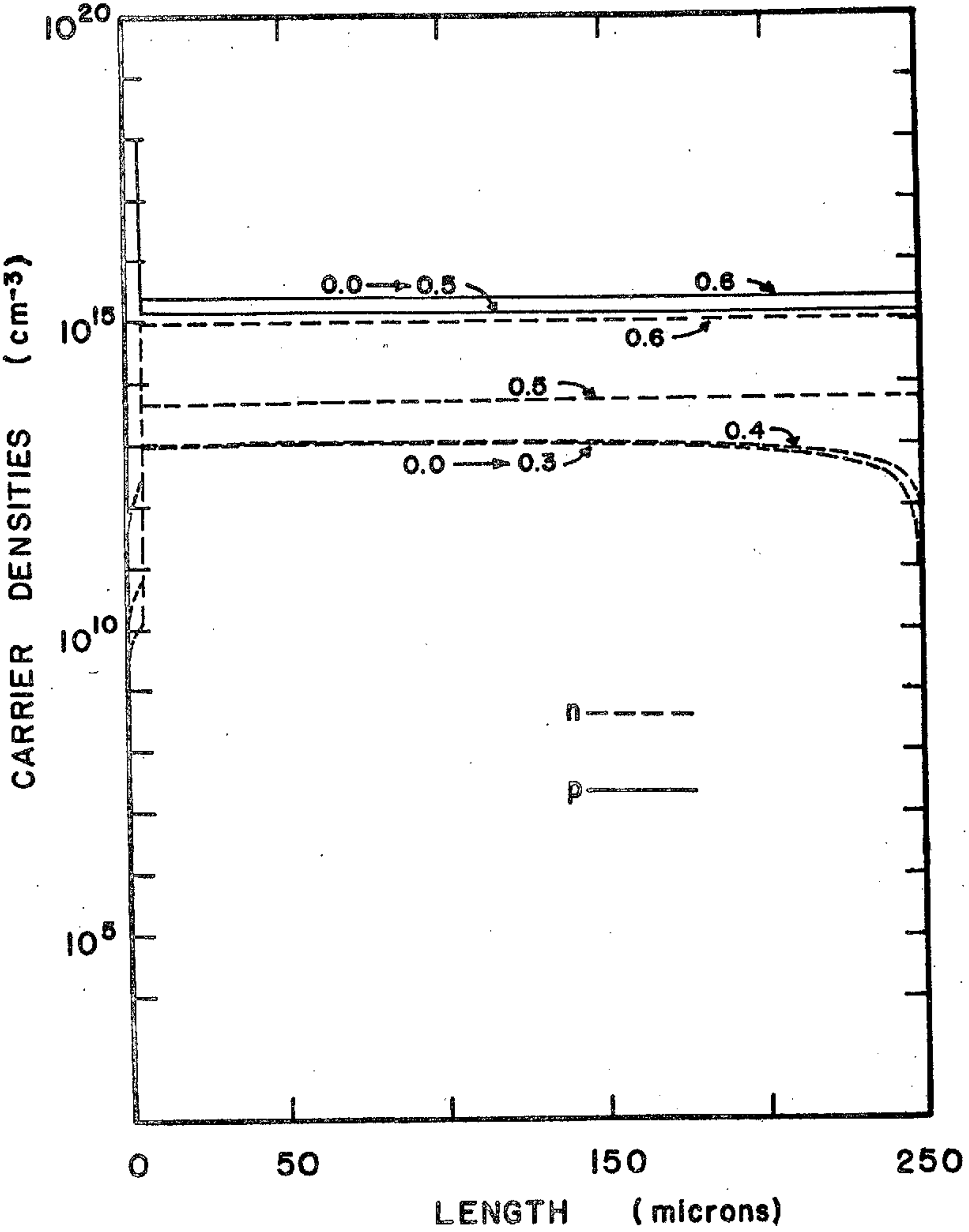

Figure 13. Hole and electron density variation in p^+-p-n^+ device under AM1 spectral irradiance (Irradiated surface at x = 250 microns).

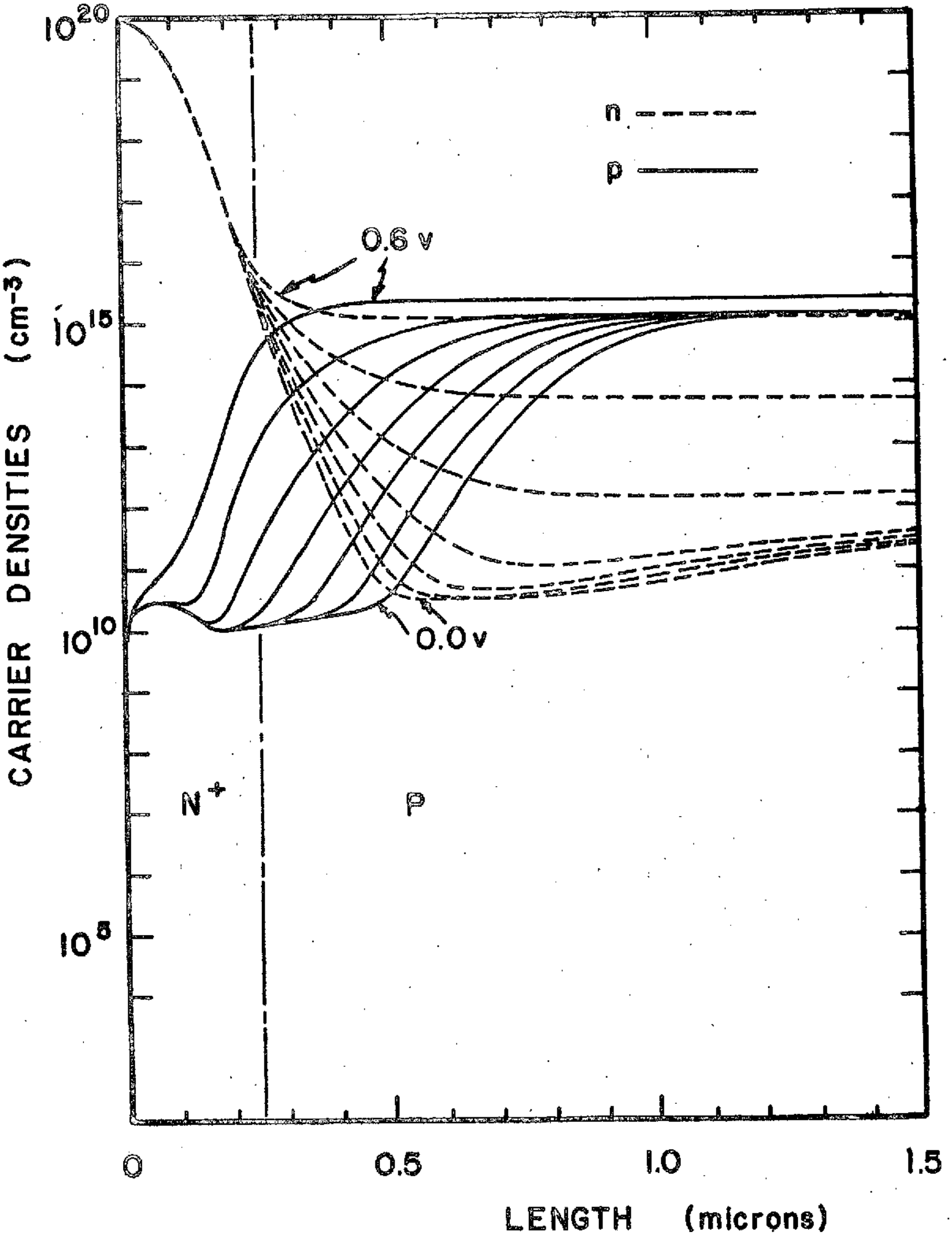

Figure 14. Hole and electron concentration about n^+-p junction near irradiated surface.

Appendix B: Optical Carrier Generation in Silicon

P. M. Dunbar and J. R. Hauser
Electrical Engineering Department
North Carolina State University, Raleigh, N. C. 27607

ABSTRACT

A numerical analysis of the spatial dependence of optical generation of electron-hole pairs in silicon due to full solar spectral irradiance is reported. The analysis includes the utilization of published experimental data on solar spectral irradiance, index of refraction, and absorption coefficients. Of particular interest is the illustration of the depth to which one must collect optical carriers in order to utilize given amounts of the incident photons. A determination of reflection and transmission coefficients is made for various thicknesses of SiO and SiO_2 antireflection coatings and optimum thicknesses for photon transmission are reported. Absorption in the SiO layer is included.

I. GENERAL FINDINGS

Electron hole pairs generated in a semiconductor arise from the interaction of photons with the valence band electrons in the semiconductor. The irradiated material is characterized by the absorption coefficient, α, which is a rather complex function of the incident photon energy. For full solar spectral irradiance, the number of incident photons as well as the reflectance properties of silicon are quite complex functions of the photon energy. Also at the higher energies of the solar spectrum the internal quantum efficiency exceeds unity. For these reasons an analytical development of the optical generation rate due to full spectral irradiance has not to date been undertaken. The present work incorporates experimental or empirical data concerning each of the above parameters in order to formulate the spatial dependence of the optical generation rate. This is performed for both air mass one (AM1) and air mass zero (AM0) solar spectral irradiance. Also calculated are the effects of both SiO and SiO_2 antireflection coatings on generation rate and the optimum thickness of these layers for maximum photon transmission into the silicon substrate. Absorption in the SiO film is included. Prior work in this area has been limited to equal energy spectral response and does not integrate into the response the full spectrum of solar irradiance, reflection losses, quantum efficiencies, or absorption in the antireflection film [1-8].

For monochromatic radiation an incident wave will decay in energy exponentially with respect to distance. This can be expressed as:

$$P(x) = P(0)\, e^{-\alpha x} , \tag{1}$$

where $\alpha = \frac{4\pi k_c}{\lambda}$ is the absorption coefficient, and k_c, the extinction coefficient, is the imaginary part of the index of refraction. Neglecting internal reflections the maximum current resulting from this incident energy may be expressed as:

$$J_{Ge} = \int\int qT(\lambda)\, N_{phi}(\lambda)\, \eta_\lambda [1-\exp(-\alpha(\lambda)x)]\, d\lambda\, dx, \tag{2}$$

where T is the transmission coefficient, $N_{phi}(\lambda)$ is the incident photon density per wavelength interval, and η_λ is the internal quantum efficiency. The generation rate is also expressed as

$$G_e(x,\lambda) = T(\lambda)\ N_{phi}(\lambda)\, \eta_\lambda\, \alpha(\lambda)\, \exp(-\alpha(\lambda)x). \tag{3}$$

A detailed discussion of the methods used to model the various components in the above expression is given in the next section. Figure 1 however, illustrates the resulting spatial variation of the calculated generation rate for a bare Silicon surface. Shown in Fig. 2 is the effect of SiO and SiO_2 single layer anti-reflection coatings under AMO conditions. For AMO conditions the generation rate is seen to exceed $10^{22}/cm^3\cdot sec$ at the surface and to decrease rapidly with distance into the semiconductor. A significant decrease is seen in generation rate as close as 10^{-6}cm ($10^{-2}\mu m$) from the surface.

A graphic illustration of the very rapid decay of the generation term can be obtained through an integration of the generation term versus distance. This calculation yields the maximum optical generation current as a function of the device depth over which optical carriers are collected. The result is presented in Fig. 3 in terms of the collection efficiency as a function of device thickness.

It is assumed in this calculation, as in the others, that the back contact is transparent. The total optical current in this work is defined as the total photon current which is present in the visible spectrum above the silicon band edge (1.11 eV in this work). The results for the other geometries and AM1 irradiance are within 2 or 3 per cent of this curve.

Table 1 summarizes the various optical parameters used in the calculations and results obtained. The total surface loss for a particular condition is the percentage of incident photons which are not transmitted into the device. This loss includes reflection and any absorption in the antireflection layer. Since the reflecting nature of silicon and any antireflection layer is strongly dependent of incident wavelengths the total surface loss will vary from AM1 to AM0 due to the difference in the two spectral densities. Results similar to these were presented by Milnes and Feucht [9]; however, their work assumed the SiO layer to be fully transparent, while in this work losses in the SiO layer have been taken into account. The theoretical calculations predict an optimum antireflection coating of about 800Å for SiO and about 1100Å for SiO_2. The predicted surface loss for SiO layers is slightly less than that for SiO_2.

II. REVIEW OF FACTORS DETERMINING GENERATION RATE

It is known that monochromatic photon absorption has an exponential dependence upon the absorption coefficient, α. Although it is possible to determine a functional dependence of the absorption coefficient upon photon energy it is quite complex, so experimental data on α <u>vs</u>. λ has been used. This data is that of H. R. Phillip [10], and Dash and Neuman [11]. However, in using this data it is necessary to review the major absorption processes in order to justify any assumptions pertaining to quantum efficiency. The single most important process for solar cell operation is that of intrinsic absorption, which is the generation of hole-electron pairs by photons of energy larger than the band gap energy. This is the most predominant mechanism in the solar spectrum range of wavelengths.

At energies above about 3/2 the band gap energy there is the possibility that hot carriers may create secondary pairs via impact ionization and thus raise the quantum yield above unity. This becomes appreciable in silicon for incident energies above 3 ev and is included in this present work by the following empirical model of Shockley [12]:

$$\eta_\lambda = 3-2\exp\left(\frac{3.3-h\nu}{2.2}\right), \quad h\nu > 3.3 \text{ ev} \qquad (4)$$

Although this increase in quantum yield is included, it can be considered somewhat secondary due to the low spectral power above 3.3 ev. Also the high absorption coefficients in this range of energy imply high surface absorption and probable subsequent loss due to surface recombination which would be present.

At energies at and below the absorption edge there are several mechanisms. The more important of these is free carrier absorption. This absorption is seen as a rise in α for photon energies near and below band edge. Of course, this mechanism has a quantum yield of zero. This zero yield is simulated by omitting any appreciable absorption coefficient data for energies below the band edge. However, free carrier absorption does still occur for energies above the band edge and could conceivably lower the effective quantum efficiency. Data by Spitzer and Fan [13] indicates a dependence of α on the square of the wavelength and on the carrier concentration. An extrapolation of their data to energies above the silicon band edge indicates that α is at most 50 cm^{-1}. Thus, the typical device will be effectively transparent to this effect.

Other low energy absorption mechanisms include lattice vibrations, exciton generation, band tailing, isoelectronic traps, and extrinsic centers (non ionized impurity centers) [14,15]. However, all of these are appreciable only into the infrared and even then have extremely low absorption coefficients. These were neglected in the development of the generation term in the same manner described above.

Reflection from the surface of the sample must be taken into account. A polished silicon surface, calculated as shown below, will lose in the neighborhood of 35% of the incident photons due to reflection. With a single layer antireflection coating this loss is reduced appreciably as shown in Table 1. For the structure illustrated in Fig. 4 the optical coefficients can be written as:

$$R = \frac{r_{12}^{2} + 2r_{12}r_{23}\exp(-2\beta)\mathrm{Cos}[2\delta-(\phi_{23} - \phi_{12})] + r_{23}^{2}\exp(-4\beta)}{1 + (r_{12}r_{23})^{2}\exp(-4\beta) + 2r_{12}r_{23}\exp(-2\beta)\mathrm{Cos}[2\delta-(\phi_{23} + \phi_{12})]}\ , \qquad (5)$$

$$T = \frac{(t_{12}t_{23})^{2}\ \exp(-2\beta)}{1 + (r_{12}r_{23})^{2}\exp(-4\beta) + 2r_{12}r_{23}\exp(-2\beta)\mathrm{Cos}[2\delta-(\phi_{23}+ \phi_{12})]}\ , \qquad (6)$$

$$T + R + A = 1, \qquad (7)$$

$$r_{12} = \frac{[n_{1}^{2} - n_{2}^{2} - k_{c2}^{2} + (2k_{c2}n_{1})^{2}]^{1/2}}{(n_{1}+n_{2})^{2} + k_{c2}^{2}}\ , \qquad (8)$$

$$r_{23} = \frac{\{(n_{2}^{2} - n_{3}^{2} + k_{c2}^{2} - k_{c3}^{2})^{2} + [2(n_{2}k_{c3} - n_{3}k_{c2})]^{2}\}^{1/2}}{(n_{2} + n_{3})^{2} + (k_{c2} + k_{c3})^{2}}\ , \qquad (9)$$

$$t_{12} = \frac{2n_{1}}{[(n_{1}+n_{2})^{2} + k_{c2}^{2}]^{1/2}}\ , \qquad (10)$$

$$t_{23} = \frac{2\{[n_{2}(n_{2}+n_{3}) + k_{c2}(k_{c2}+k_{c3})]^{2} + (n_{2}k_{c3}-n_{3}k_{c2})^{2}\}^{1/2}}{(n_{2}+n_{3})^{2} + (k_{c2}+k_{c3})^{2}}\ , \qquad (11)$$

$$\delta = \frac{2\pi}{\lambda}\, n_{2}d, \qquad (12)$$

$$\beta = \frac{2\pi}{\lambda}\, k_{c2}d, \qquad (13)$$

$$\phi_{12} = \mathrm{Tan}^{-1}\left\{\frac{2\ k_{c2}n_{1}}{n_{1}^{2} - n_{2}^{2} - k_{c2}^{2}}\right\}\ , \qquad (14)$$

$$\phi_{23} = \mathrm{Tan}^{-1}\left\{\frac{2(n_2k_{c3} - n_3k_{c2})}{n_2^2 - n_3^2 - k_{c3}^2 + k_{c2}^2}\right\} \qquad (15)$$

The quantities r_{12}, r_{23}, t_{12}, and t_{23} can be viewed as the magnitudes of the complex Fresnal Coefficients. The phase shifts ϕ_{12} and ϕ_{23} are due to absorption in the antireflection layer and the silicon respectively. In the above formulations "n" is the real part of the index of refraction and k_c is the imaginary part. For a transparent film, k_{c2} is zero, as is ϕ_{12}. In performing this calculation with a silicon substrate, experimental data for α, n_3, and k_{c3} versus wavelength were utilized. Results yielding the transmission coefficient as a function of photon energy are shown in Fig. 5. The reflectance for a bare silicon surface (d = 0) shown in the figure agrees directly with the data of H. R. Phillip [10]. Also shown is the transmission coefficient for an antireflection film of SiO_2 at its optimum thickness. For SiO, the transmission, reflection, and absorption coefficients are illustrated in Fig. 6. These optimum thicknesses are determined by the maximum efficiency of photon transmission into the substrate as described below.

The results for photon transmission efficiencies for both SiO and SiO_2 are shown in Fig. 7 as functions of antireflection layer thickness. This illustrates an optimum thickness of around 1100Å for SiO_2 and 800Å for SiO. It has been assumed in this calculation that the SiO_2 layer is transparent within the spectral region of interest with a constant index of refraction of 1.44. This is a good assumption for SiO_2, but SiO is somewhat lossey in this region. To include this absorption, the data of Hass and Salzburg [16] of the index of refraction and extinction coefficient was used to determine values for n_2 and k_{c2} for SiO. This data is illustrated in Fig. 8.

The available experimental data on reflectance from silicon surfaces is somewhat scattered. Prince has reported a maximum reflectance of 6% in the spectrum below 3 ev [4], while Phillip [10] and Malovetskaya [17] present data illustrating reflectances ranging over 30% within the same spectral energies. The reflectances calculated in this report for bare silicon (Fig. 5) agree closely with the most recent experimental data of Phillip. Although the program utilized the index of refraction and absorption coefficient data calculated by Phillip from the experimental reflectance measurements, it should be realized, however, that the absorption coefficient data is essentially the same experimental data as that published by Dash and Neumann [11]. Although Malovetskaya does not report the thickness of the SiO_2 layer utilized in his work, he does report a maximum transmission of about 93% at 1.5 eV for this case. This agrees quite well with the calculations presented in this paper.

III. CALCULATION TECHNIQUES

Utilizing the data and equations discussed in the previous section, a computer program has been developed to calculate the carrier generation rate under various conditions including that of a general single layer antireflection coating. The general flow of the program is illustrated in Fig. 9. The incident photon density is determined from published data on full spectrum solar irradiance. A most comprehensive collection of data on solar radiant energy is the NASA document for Space Vehicle Design Criteria which develops final data from weighted averages of several investigations [18]. The parameters of interest are the solar constant and the solar spectral irradiance. The data used for irradiance under AM1 conditions (sea level) is that of P. Moon [19]. Due to great uncertainties as to atmospheric absorption and latitude of measurement this data must be viewed as typical. The data was read numerically and stored in the program. The incident photon density is related to the photon energy, irradiance, and wavelength interval as

$$N_{phi} = \frac{\left(\frac{H}{\Delta\lambda}\right) \Delta\lambda}{E_\lambda} \; (\#/\mathrm{sec/cm}^2) \qquad (16)$$

where $\left(\frac{H}{\Delta\lambda}\right)$ is the average irradiance over an increment of $\Delta\lambda$, and E_λ is the average energy of the $\Delta\lambda$ increment. The published data is a tabular form of $\left(\frac{H}{\Delta\lambda}\right)$ versus wavelength. All available data above 1.11 eV and up to about 7 eV was included.

The next stage in the calculation is to read into the program the published data for the absorption coefficient and index of refraction for silicon. This data was supplied in tabulated form from H. R. Phillip [10]. These values are interpolated to the wavelengths of the spectral irradiance data. This then supplies N_{phi}, α, n_3, and k_{c3} for each wavelength available from the solar spectrum data. With these values the reflectance of the Si surface and the Si-SiO$_2$ surface can be calculated. For the SiO layer a similar interpolation process on the index of refraction (n_2) and extinction coefficient (k_{c2}) data [16] allowed the calculation of these coefficients at the relevant wavelengths. At this point the surface photon efficiency η_N is calculated as

$$\eta_N = \frac{\sum_\lambda N_{phi} \; T \; \eta_\lambda}{\sum_\lambda N_{phi}} \tag{17}$$

where T is the transmission coefficient. The surface loss of Table 1 is $1-\eta_N$.

Prior to calculating the generation rate, a spatial distribution is developed which limits the change in G_e between spatial points to about 10%. This then allows the generation rates to be calculated at each spatial point by summing the contribution to G_e of each incident wavelength. Once this data is developed in a tabular form, it is numerically integrated to obtain the spatial dependence of the maximum optical current.

The total number of incident photons in the visible spectrum for energies above the silicon band edge (1.11 eV for this work) sum to $3.31 \times 10^{17}/\text{cm}^2$ for AM0 and $2.14 \times 10^{17}/\text{cm}^2$ for AM1. These values are about 5% below what is normally used. There is, however, some ambiguity as to the proper value of these quantities since the published irradiance data for AM0 and AM1 vary somewhat. Also, since silicon is an indirect band gap material, there is not a sharp edge to the absorption curve making the assignment of the band gap energy somewhat ambiguous. For the AM0 condition a 3% change in the energy band gap (i.e. from 1.08 eV to 1.11 eV) can result in a 3% decrease in the total number of incident photons. Photons at these energies, however, contribute little to the photocurrent due to the extremely low absorption coefficients in the immediate vicinity of the band edge. The photon density from the irradiance data corresponds to an available current of 52.9 mA/cm^2 for AM0 and 34.2 mA/cm^2 for AM1. The inclusion of enchanced quantum efficiency at higher energies resulted in a 1.5% increase in the total available current over the total spectral current for AM0. The increase for AM1 was quite insignificant, being below 0.5%.

IV. CONCLUSIONS

It is found that the spatial decay of the optical generation rate in silicon due to solar irradiance is extremely rapid. This very rapid decay may allow narrower devices in collection applications than previously expected; however, it also indicates the importance of surface treatments to greatly reduce surface recombination. For AMO applications the SiO and SiO_2 antireflection layers are seen to be roughly equivalent, with the SiO layer slightly more efficient. This rough equivalence points out the need to include the absorption characteristics of the SiO film, for this degrades the efficiency of this film by roughly 5%. However, the optimum thickness for the SiO layer is somewhat thinner than the SiO_2, 800Å vs. 1100Å. In the actual use of SiO as an antireflection layer on solar cells the difference between SiO and SiO_2 is likely to be greater than indicated by the photon efficiency calculation. The SiO film results in a lowered generation rate near the surface and an enhanced generation rate deep within the silicon. Thus surface recombination losses may be less with SiO than with SiO_2 (assuming the same surface recombination velocity) giving SiO a slightly larger advantage over SiO_2. For AM1 applications the optimum film thicknesses are approximately the same as AMO. The SiO film is still somwhat more efficient than the SiO_2 with the difference slightly more pronounced since the AM1 spectrum is quite deficient in higher energy photons.

ACKNOWLEDGEMENTS

The authors would like to express their gratitude to Dr. H. R. Phillip for supplying tabulated data of the absorption coefficient and index of refraction for silicon.

140

REFERENCES

1. M. B. Prince, J. Appl. Phys. 26, 534 (1955).
2. J. J. Loferski, J. Appl. Phys. 27, 777 (1956).
3. M. Wolf, Proc. IEEE, 48, 1246 (1960).
4. M. B. Prince and M. Wolf, J. Brit. IRE, 18, 583 (1958).
5. J. J. Loferski, Proc. IEEE, 667 (1963).
6. M. Wolf, Energy Conversion, 11, 63 (1971).
7. L. M. Terman, Solid St. Electron, 2, 1 (1961).
8. P. Rappaport, RCA Review, 20, 373 (1959).
9. Milnes and Feucht, Heterojunctions and Metal Semiconductor Junctions, p. 134, Academic Press (1972).
10. H. Phillip, J. Appl. Phys., 43, 2835 (1972).
11. W. C. Dash and R. Newman, Phys. Rev., 99, 1151 (1955).
12. W. Shockley, Solid-St. Electron, 2, 35 (1961).
13. W. Spitzer and H. Y. Fan, Phys. Rev., 108, 268 (1957).
14. T. S. Moss, G. J. Burrell, B. Ellis, Semiconductor Opto Electronics, John Wiley (1973).
15. J. I. Pankove, Optical Processes in Semiconductors, Prentice-Hall (1971).
16. G. Hass and C. Salzberg, J. Opt. Soc. Amer., 44, 181 (1954).
17. V. M. Malovetskaya, V. S. Vavilov, and G. N. Galkin, Soviet Phys. of S. State, 1, 1099 (1960).
18. NASA, Solar Electromagnetic Radiation, NASA SP 8005 (1971).
19. P. Moon, J. Franklin Inst., 230, 583 (1940).

Table 1. Summary of Excess Carrier Generation in Silicon

Geometry	Spectral Conditions	Optimum Anti-Reflection Thickness (Å)	Surface Loss[†] (%)	Total Optical Current[†] (mA/cm^2)	Surface Generation Rate[†] (#/cc/sec)
Si	AM0	N. A.	36.4	34.2	$1.15x10^{22}$
	AM1	N. A.	34.7	22.4	$1.62x10^{21}$
Si + SiO	AM0	800	15.6	45.4	$5.96x10^{21}$
	AM1	800	10.4	30.7	$1.39x10^{21}$
Si + SiO_2	AM0	1100	17.6	44.3	$1.25x10^{22}$
	AM1	1100	14.5	29.3	$1.83x10^{21}$

[†] Computed at Optimum Antireflection Thickness if applicable.

FIGURE CAPTIONS

Figure 1. Spatial dependence of the excess carrier generation rate for AM1 and AM0 illumination.

Figure 2. Spatial dependence of the excess carrier generation rate for both single layer SiO and SiO_2 films at their optimum thickness.

Figure 3. Percentage of optical current collected versus device length. Although this curve is for AM0 with no anti-reflection coating the other conditions have quite similar results.

Figure 4. Structure utilized in the calculation of the optical coefficients.

Figure 5. Transmission coefficients for silicon and silicon plus the optimum thickness of SiO_2.

Figure 6. Transmission (T), Absorption (A), and Reflection (R) coefficients for optimum thickness of a single layer SiO film.

Figure 7. Efficiency of photon transmission into silicon versus film thickness for both SiO and SiO_2.

Figure 8. Real and imaginary parts of the index of refraction for SiO [16].

Figure 9. Flow chart for optical generation program.

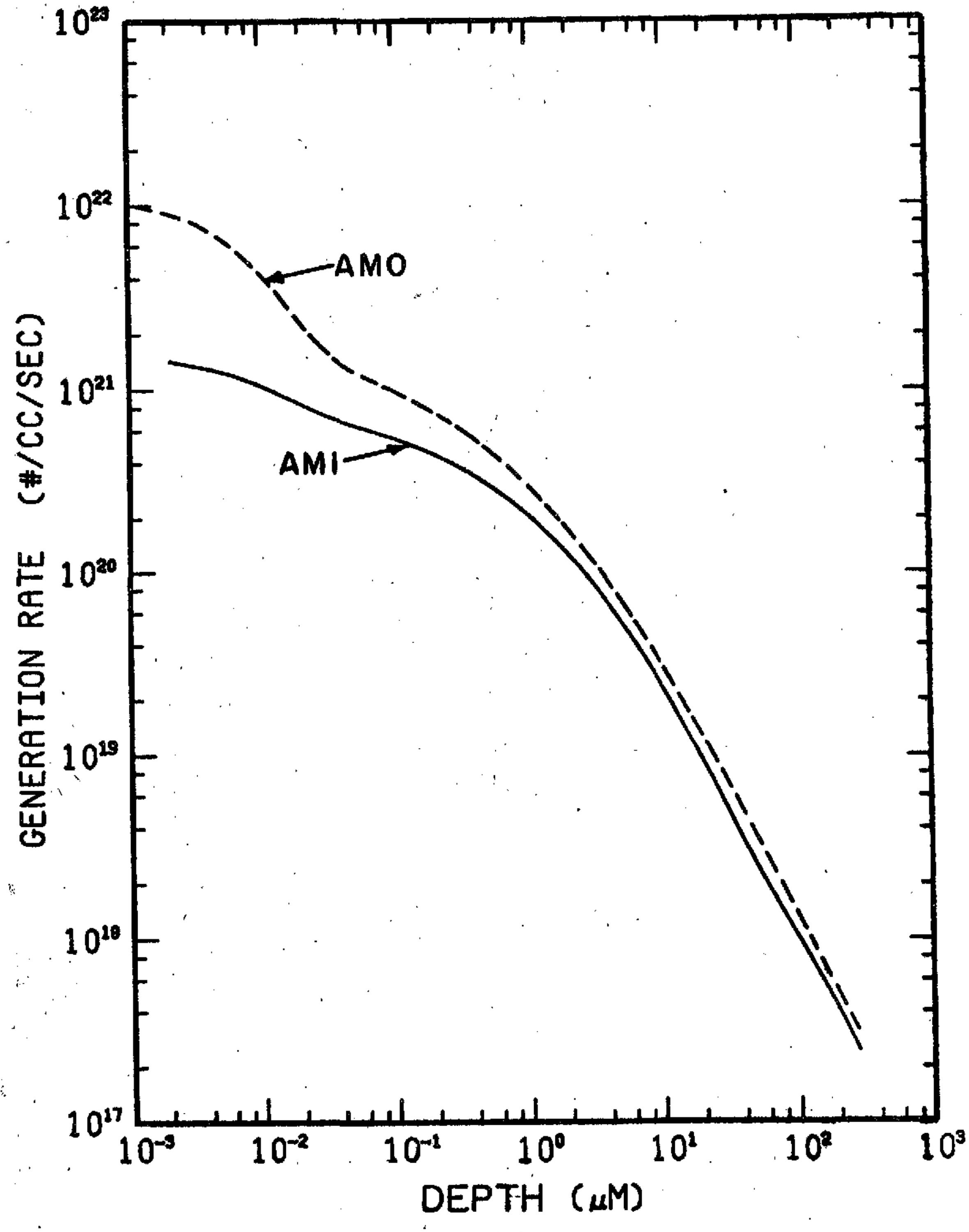

Figure 1. Spatial dependence of the excess carrier generation rate for AM1 and AM0 illumination.

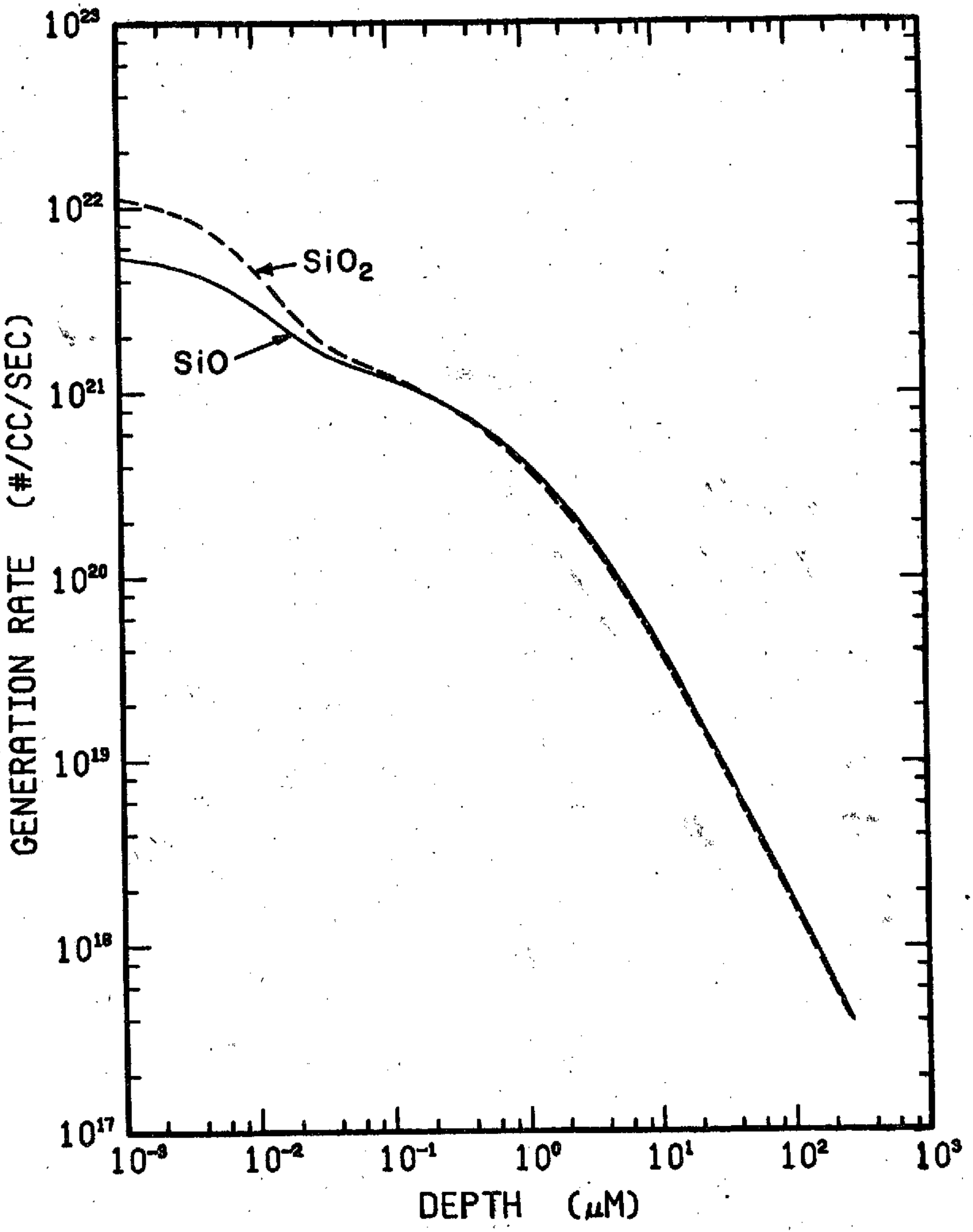

Figure 2. Spatial dependence of the excess carrier generation rate for both single layer SiO and SiO_2 films at their optimum thickness.

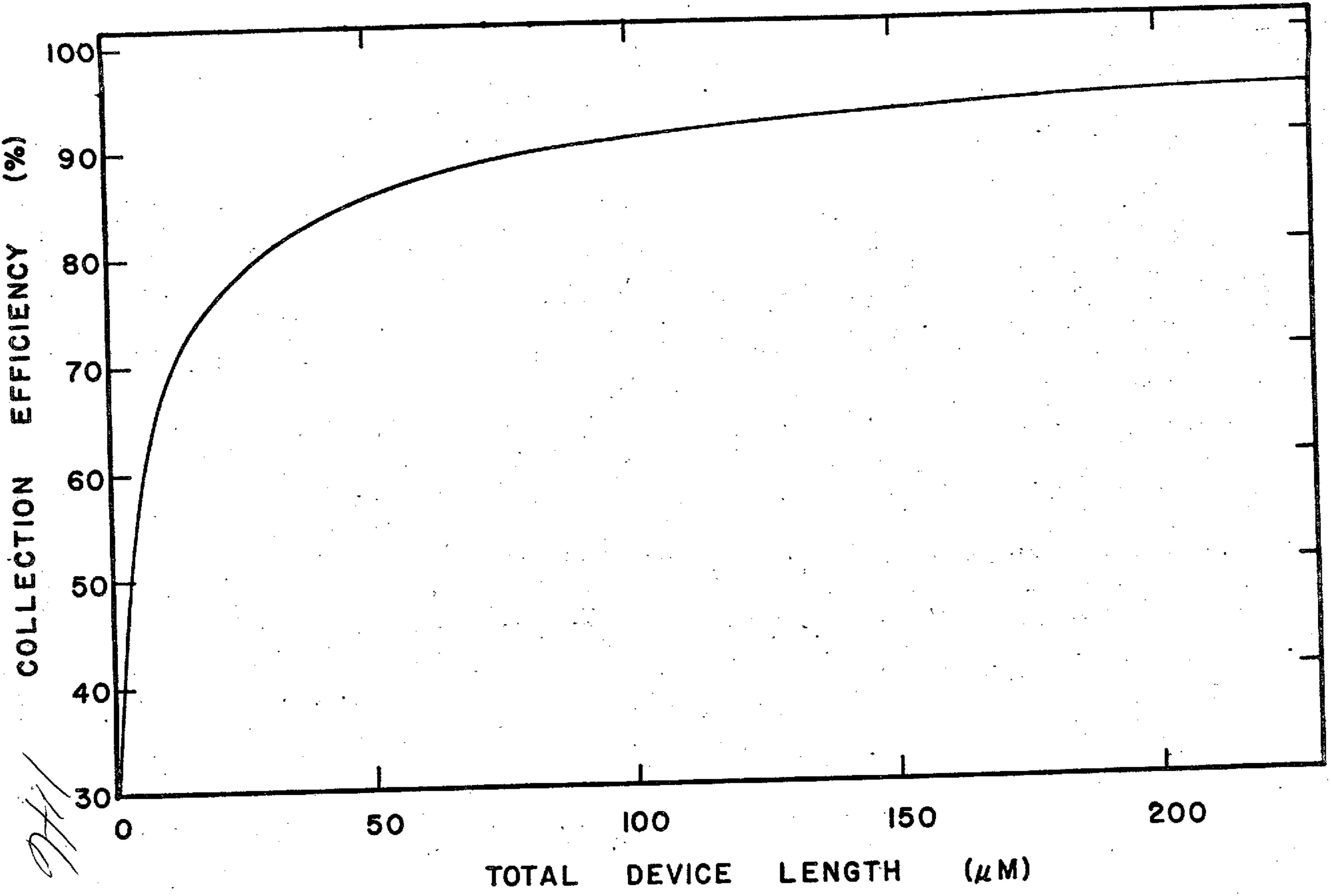

Figure 3. Percentage of optical current collected versus device length. Although this curve is for AMO with no antireflection coating the other conditions have quite similar results.

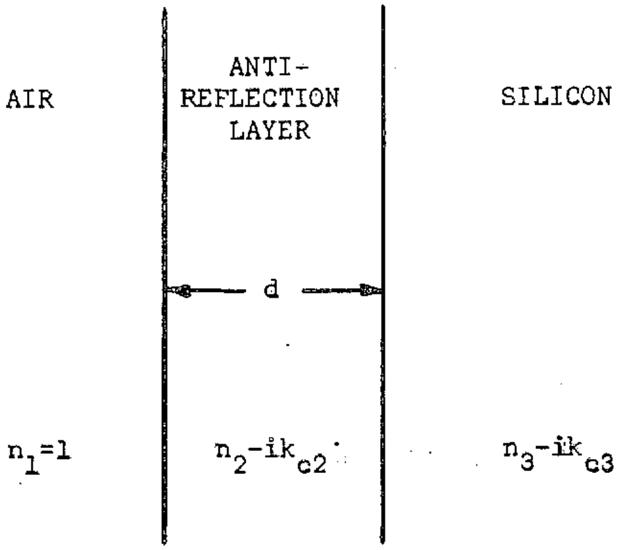

Figure 4. Structure utilized in the calculation of the optical coefficients.

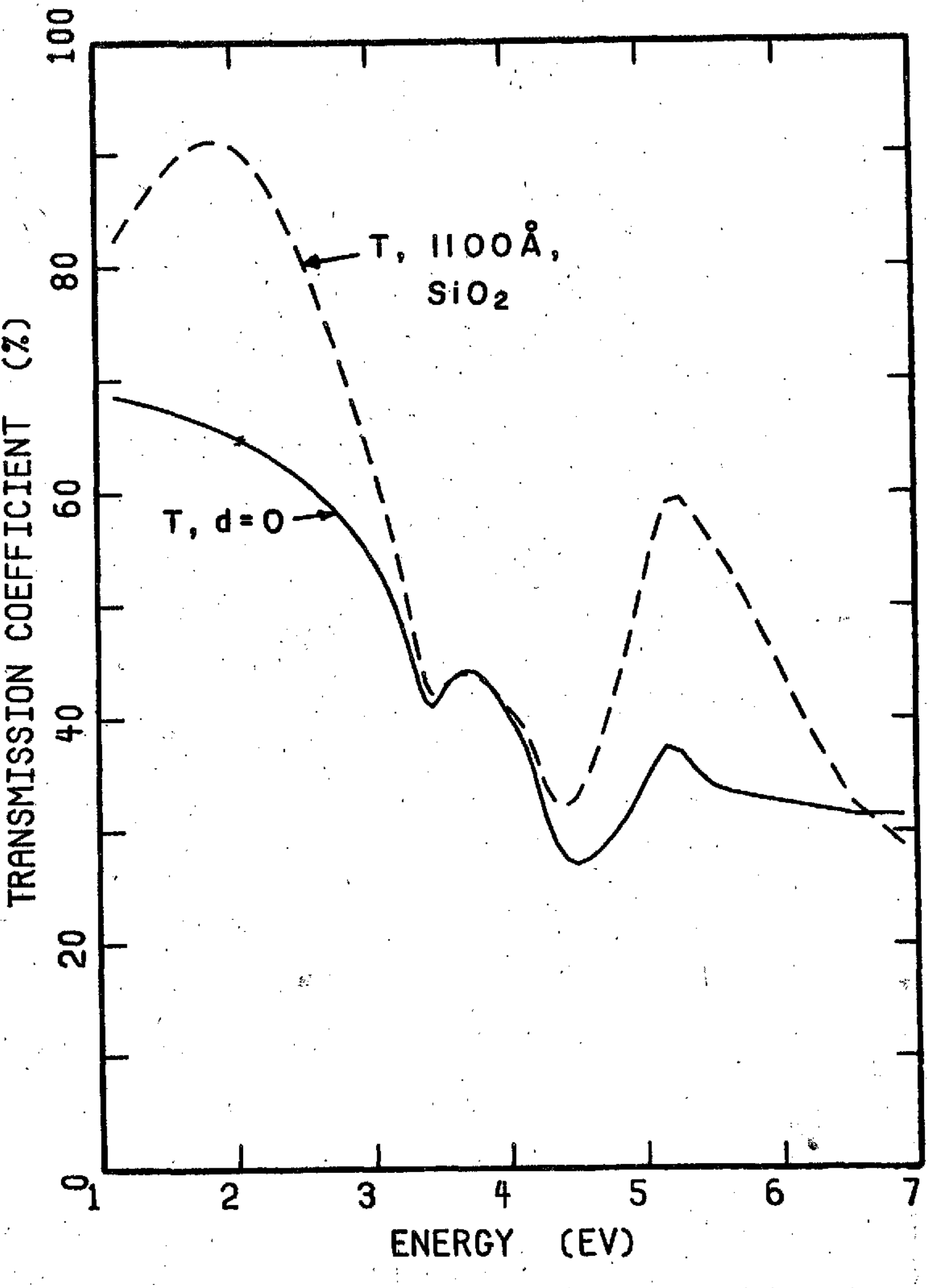

Figure 5. Transmission coefficients for silicon and silicon plus the optimum thickness of SiO_2.

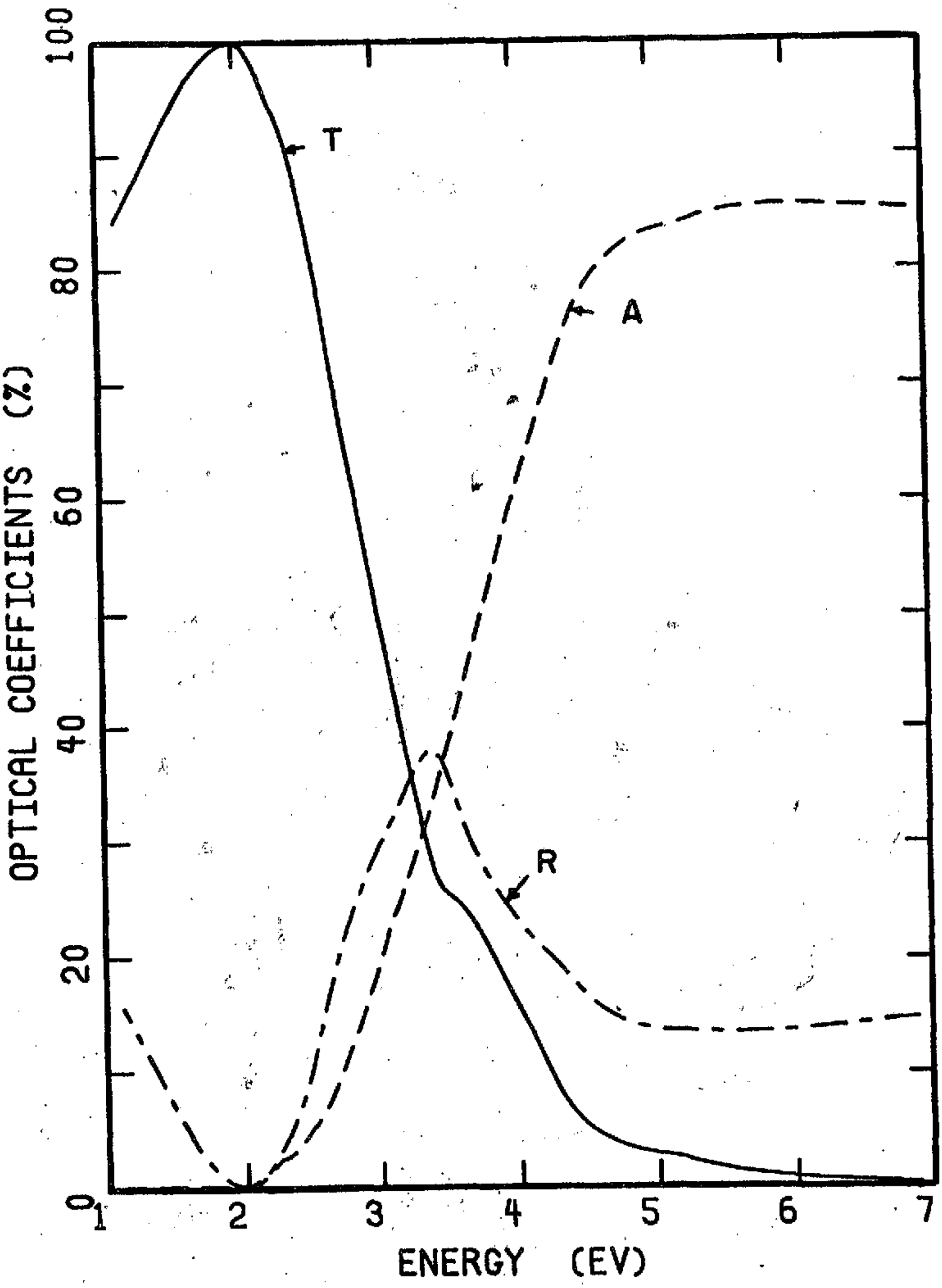

Figure 6. Transmission (T), Absorption (A), and Reflection (R) coefficients for optimum thickness of a single layer SiO film.

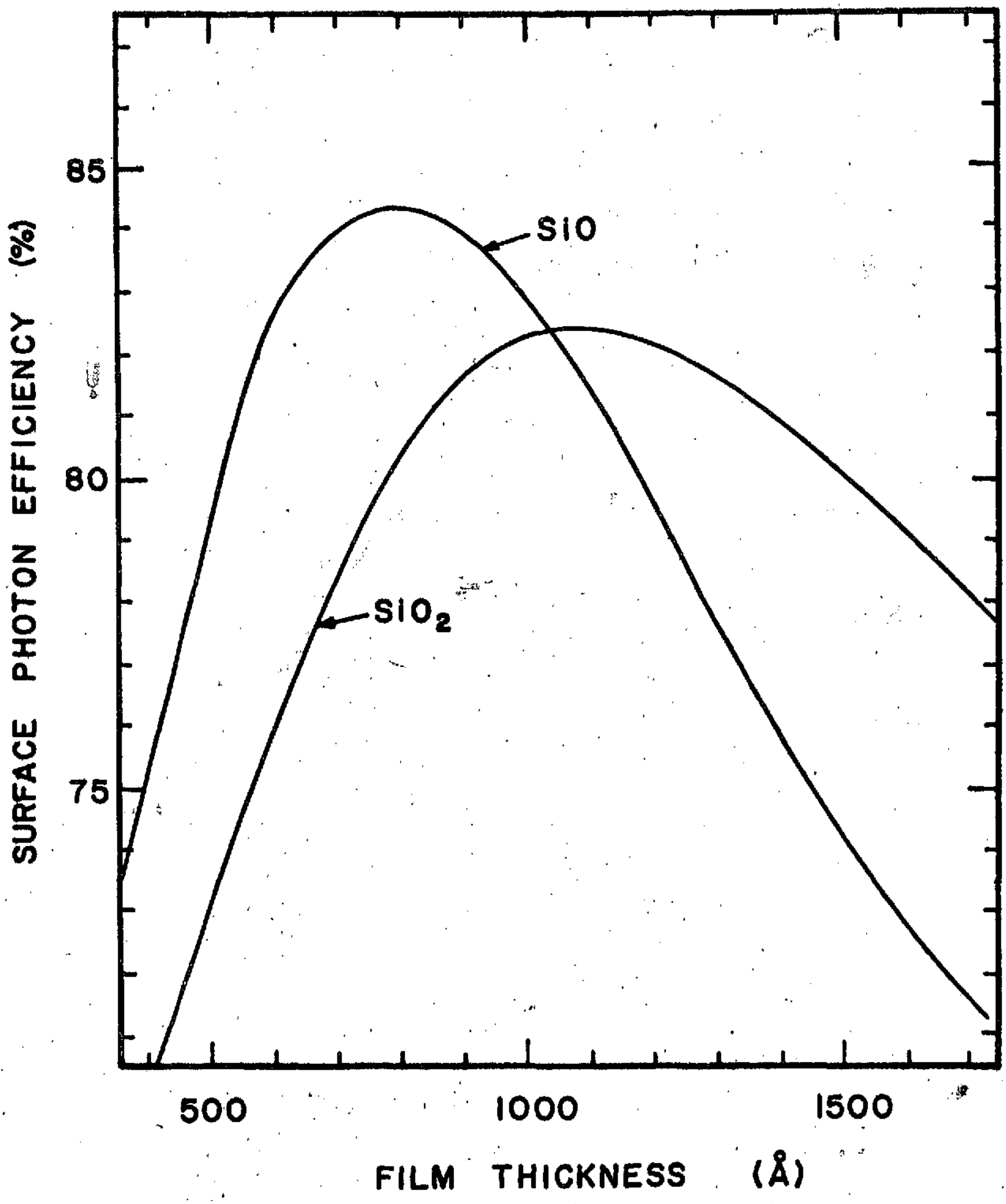

Figure 7. Efficiency of photon transmission into silicon versus film thickness for both SiO and SiO_2.

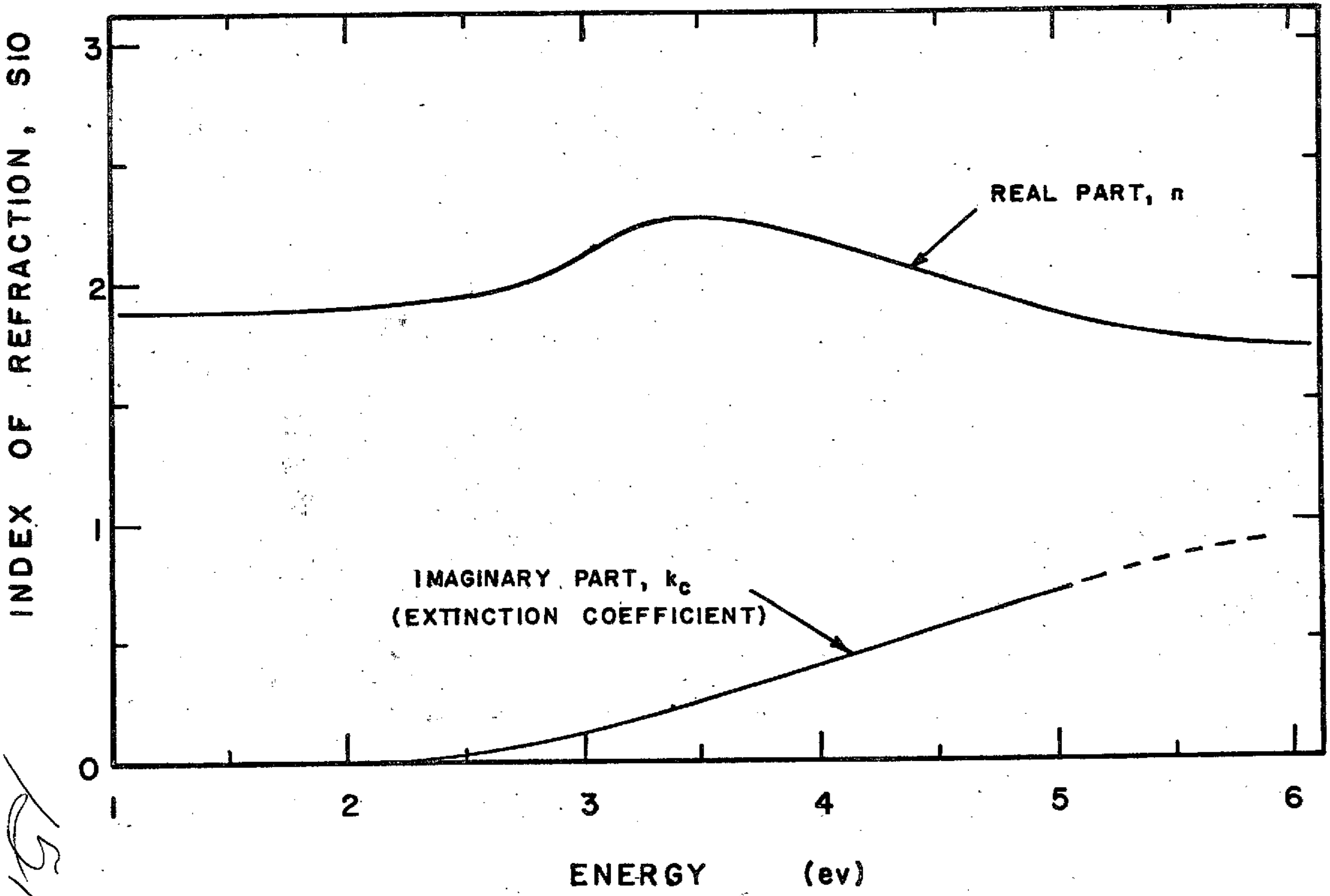

Figure 8. Real and imaginary parts of the index of refraction for SiO [16].

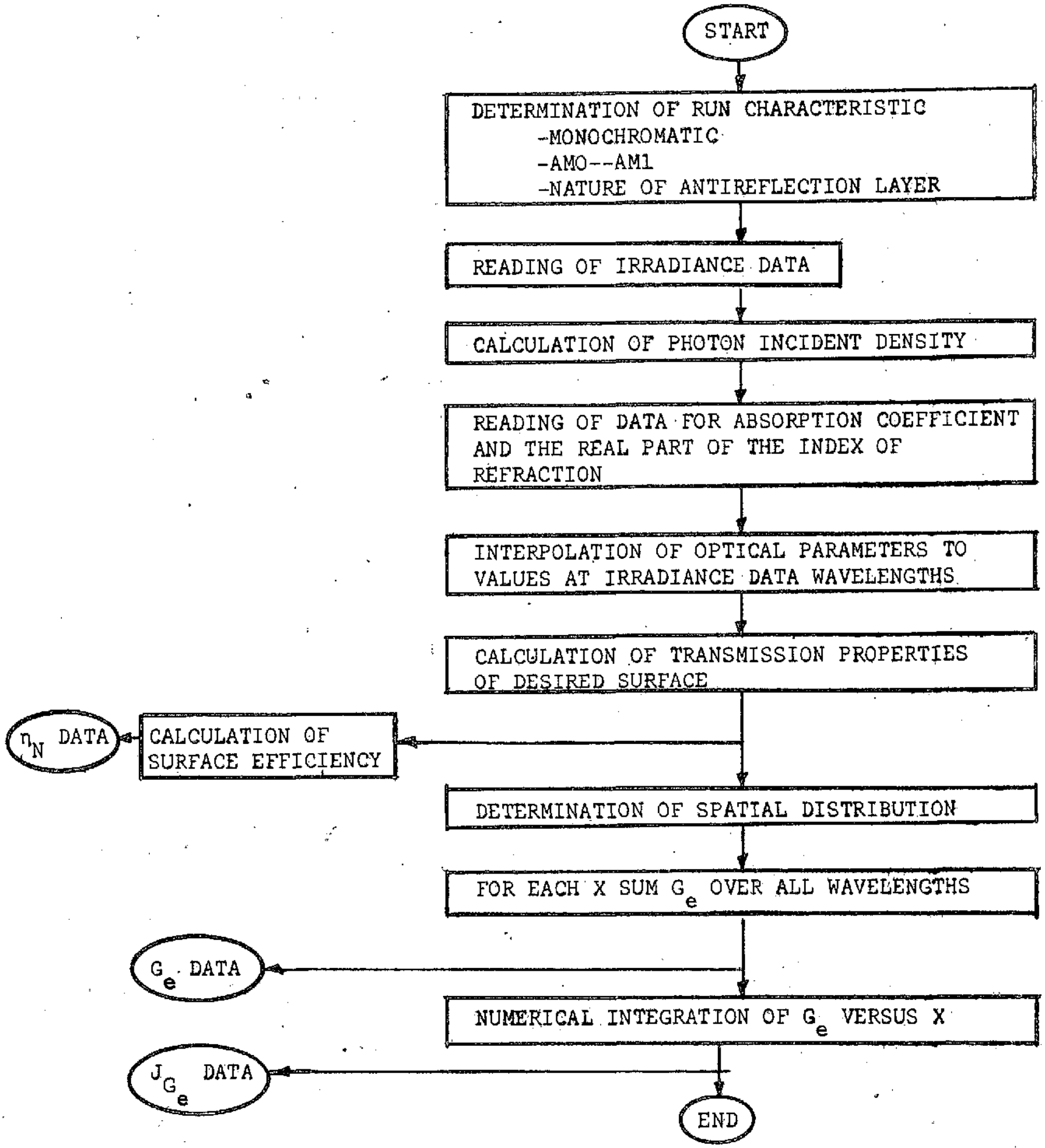

Figure 9. Flow chart for optical generation program.

Appendix C: Minority Carrier Reflecting Properties of Semiconductor High-Low Junctions

J. R. Hauser and P. M. Dunbar
Electrical Engineering Department
North Carolina State University
Raleigh, North Carolina 27607

ABSTRACT

This paper discusses the results of some computer calculations on the minority carrier reflecting properties of high-low junctions. In general it has been found that high-low junctions obey first order device models to a high degree of accuracy. The ratio of carrier densities on the sides of the junction depletion region is exponentially related to the high-low junction voltage, which is constant until high injection effects begin to occur. For high injection on the lightly doped side of the high-low junction, the junction potential decreases and the minority carrier reflecting properties of the junction are degraded.

I. INTRODUCTION

High-low junctions (either p^+-p or n^+-n) find a number of applications in solid state devices. They are most frequently used as an interface region between a more lightly doped semiconductor and a metal contact in order to provide an ohmic contact to the semiconductor. In this application they are known to provide an essentially linear current-voltage relationship for majority carrier flow across the high-low interface [1,2]. In addition to aiding in making ohmic contacts, high-low junctions also act as minority carrier reflecting boundaries. In many minority carrier devices this is a useful side effect which can significantly reduce minority carrier recombination at ohmic contacts.

The present work reports on some computer solutions of the minority carrier reflecting properties of high-low junctions which are located near an injecting p-n junction. This work has resulted from a study of p^+-p-n^+ type diode structures. However, the same type of behavior should be observed at any high-low junction located near an injecting p-n junction. A comparison is also presented of first order analytical models for high-low junctions with the exact computer solutions.

II. HIGH-LOW JUNCTION PROPERTIES

The device structure studied in this work is shown in Fig. 1. It is an n^+-p-p^+ diode with the n^+ diffused layer modeled by a Gaussian impurity profile with a surface concentration of $10^{20}/\text{cm}^3$ and a junction depth of 0.25 μm. The p-region is taken as a uniformly doped region with results for 10 Ω·cm and 2000 Ω·cm material reported in this work. The p^+ region has been taken as a uniformly doped region with an impurity concentration of $10^{18}/\text{cm}^3$ and a thickness of either 5 μm or 0.5 μm. The overall device thickness is 250 μm for the results reported in this paper.

The electron lifetime in the p-region was taken as 100 μsec and 1000 μsec for the 10 Ω·cm and 2000 Ω·cm material respectively. Other device thicknesses have been studied but the total device thickness does not strongly influence the minority carrier reflecting properties of the p^+-p junction.

The device structures studied have been less than a diffusion length in total thickness. The p^+-p interface thus acts as a minority carrier reflecting boundary preventing electrons injected by the n^+-p junction from reaching the back ohmic contact. Various injected electron concentration profiles for this diode can appear as shown in Fig. 2 as the back boundary ranges from a perfectly reflecting contact to an ohmic contact. For the devices studied in this work the high-low junction closely approximates an ideal reflecting back contact even for p^+ thicknesses of 0.5 μm.

There are several parameters which characterize a high-low junction as far as its minority carrier reflecting properties are concerned.

First, there is the equilibrium high-low junction voltage, V_{hlo}, which is related to the doping densities as

$$V_{hlo} = \frac{kT}{q} \ln (N_{p^+}/N_p), \tag{1}$$

where N_{p^+} and N_p are the p^+- and p-region doping densities. The high-low junction potential can only change from its equilibrium value if there is a significant change in the majority carrier concentration on one or the other side of the high-low junction. A second fundamental parameter is the ratio of minority carriers (electrons in this case) across the junction. Assuming that the change in minority carrier quasi-Fermi level is negligible across the interface gives [1],

$$n_{p^+} = n_p \exp(-qV_{hl}/kT). \tag{2}$$

If high injection does not occur on the lightly doped p-side, V_{hl} is approximately the equilibrium value and

$$n_{p^+} \approx n_p N_p/N_{p^+}. \tag{3}$$

This expression is the basis for the reflecting properties of the high-low junction since it shows that the minority carrier concentration is reduced by the ratio N_p/N_{p^+} in going from the p to p^+ side of the junction.

The expression of Equation (3) is based upon a low injection condition. In the more general case, Equation (2) must be combined with the assumption of charge neutrality at the edges of the junction depletion region to give the following more complete expression:

$$n_{p^+} = n_p \left(1 + \frac{n_p}{N_p}\right) \frac{N_p}{N_{p^+}}. \tag{4}$$

The additional correction factor of $(1 + n_p/N_p)$ becomes important when high injection occurs on the lightly doped side of the high-low junction.

A final parameter characterizing the minority carrier reflecting properties of a high-low junction is what Gunn [3] terms the junction leakage velocity or which can also be termed the effective surface recombination velocity, S_{pp^+}, of the high-low junction. As opposed to the ratio of minority carriers across the interface which depends only on the high-low junction doping levels, the leakage velocity depends on the width of the p^+ region and the minority carrier lifetime in this region. For uniform doping in the p^+ region and neglecting recombination within the high-low junction space charge region,

$$S_{pp^+} = \frac{D_{np^+}}{L_{np^+}} \coth \left(\frac{W_{p^+}}{L_{np^+}}\right) \frac{n_{p^+}}{n_p} , \tag{5}$$

where D_{np^+} and L_{np^+} are the electron diffusion constant and diffusion length in the p^+ region. The above can be combined with Equation (4) to give

$$S_{pp^+} = \frac{D_{np^+} N_p}{L_{np^+} N_{p^+}} \coth \left(\frac{W_{p^+}}{L_{np^+}}\right)\left(1 + \frac{n_p}{N_p}\right). \tag{6}$$

At low injection this is a constant but the value increases linearly with n_p at high injection. This causes the minority carrier current into the high-low junction to increase linearly with carrier density n_p at low injection and to increase as n_p^2 at high injection.

III. COMPUTED RESULTS

The simple models discussed in the previous section have been found to agree extremely well with exact computer calculations for high-low junctions. The computer program used in the present device analysis has been previously discussed [4]. Calculations have been made for the structure of Fig. 1 for a variety of dimensions and doping densities. Calculations are made at various terminal voltages which result in increasing levels of carrier injection into the p-region. Shown in Fig. 3 are curves for electron concentration plotted from the back surface through the high-low junction for a 0.5 μm wide p^+ region. The electron concentration in the p-side ranges from slightly above $10^9/cm^3$ to about $10^{16}/cm^3$ while the concentration on the p^+ side ranges from about $10^4/cm^3$ to about $10^{14}/cm^3$. The V_A values on the curves are the values of applied diode voltage corresponding to each injection level. For the low values of V_A the junction depletion region extends beyond 1.5 μm and the carrier densities are not yet constant. Shown in Fig. 4 is the dependence of n_{p^+} on n_p for this device (curve A). The solid curve is the simple model as given by Equation (4) while the data points are results of the exact computer calculations. The onset of high injection can be seen for the highest injection levels. Calculations for a 5 μm wide p^+ region are essentially identical with the results shown in Fig. 4 with the ratio of minority carriers across the high-low junction independent of the width of the p^+ region. Also shown in Fig. 4 are similar data (curve B) for a diode with a p-side concentration of $1.3x10^{15}/cm^3$. At high injection both curves approach the same limiting values which are independent of p-side doping density.

Under high injection conditions, the potential across the high-low junction decreases from its equilibrium value. This is shown in Fig. 5 where the decrease in potential is seen for the four highest injection levels. For curves (a) and (b) the junction depletion region extends beyond 1.5 μm. As the junction potential decreases at high injection, the ratio of minority carriers across the interface decreases and the reflecting properties of the high-low junction are degraded. The effective surface recombination velocity of the junction increases as high injection occurs according to Equation (6).

Shown in Fig. 6 is a comparison of the high-low junction leakage current as given by the expression

$$J_{nhl} = qn_p S_{pp^+}, \tag{7}$$

and the exact results of the computer solutions. Again it is seen that at low injection the leakage current is proportional to n_p indicating a constant S_{pp^+} while at high injection the leakage current depends on n_p^2 indicating that S_{pp^+} approaches a linear dependence on n_p. As indicated in the figure, at low injection the high-low junction has a low effective surface recombination velocity. The nearly ideal minority carrier reflecting properties of these high-low junctions is due to this low value of effective surface recombination velocity. Similar high-low junctions but with a 5 μm thick p^+ layer have about an order of magnitude smaller effective surface recombination velocity.

Implicit in the derivation of Equations (3) and (4) is the assumption that the minority carrier quasi-Fermi level does not change in going across the high-low junction. This assumption has been verified with the computer calculations. Shown in Fig. 7 is the calculated quasi-Fermi levels for electrons ϕ_n around the high-low junction. The only change in ϕ_n around the high-low junction is the almost abrupt change in slope of the ϕ_n curves at the high-low junction. This is to be expected since $\frac{d\phi_n}{dx}$ must be inversely proportional to the electron concentration in a region where there is negligible change in current density.

IV. CONCLUSIONS

This work has reviewed the first order approximations normally employed to describe the minority carrier reflecting properties of high-low junctions and compared these expressions with exact computed results. The first order results are found to be in very good agreement with the computer results when account is taken of high injection effects on the lightly doped side of the high-low junction. High injection reduces the effectiveness of the high-low junction as a minority carrier reflecting boundary and leads to an increased effective surface recombination velocity of the junction.

REFERENCES

1. J. B. Gunn, "On Carrier Accumulation and the Properties of Certain Semiconductor Junctions," J. Electronic Control, vol. 4, p. 17, 1958.

2. R. W. Lade and A. G. Jordan, "A Study of Ohmicity and Exclusion in High-Low Semiconductor Junction Devices," IEEE Trans. Electron Devices, vol. ED-10, pp 268-277, July 1963.

3. R. W. Dutton and R. J. Whittier, "Forward Current-Voltage and Switching Characteristics of p^+-n-n^+ (Epitaxial) Diodes", IEEE Trans. Electron Devices, vol. ED-16, pp. 458-467, May 1969.

4. E. D. Graham, Jr. and J. R. Hauser, "Effects of Base Doping and Width on the J-V Characteristics of the n^+-n-p^+ Structure", Solid-State Elec. vol. 15, pp 303-310, 1972.

FIGURE CAPTIONS

Fig. 1. Device structure for n^+-p-p^+ diode (A) 1000Ω·cm p-region, $N_p = 7\times10^{12}/cm^3$, $N_{p^+} = 10^{18}/cm^3$ (B) 10Ω·cm p-region, $N_p = 1.3\times10^{13}/cm^3$, $N_{p^+} = 10^{18}/cm^3$.

Fig. 2. Effect of back contact on injected electron concentration ($W_p \ll L_n$); (a) Ideal reflecting back contact (b) partially reflecting back contact (c) ohmic contact.

Fig. 3. Calculated minority carrier concentration around the high-low junction at various injection levels (1000 Ω·cm p-region).

Fig. 4. Minority carrier concentration at edge of depletion region in p^+-side as a function of minority carrier concentration at edge of depletion region on p-side. The solid curves are simple calculations from Eq. (4), while the data points are results of computer analysis.

Fig. 5. Electrostatic potential around high-low junction at various injection levels (1000 Ω·cm p-region).

Fig. 6. High-low junction leakage current as a function of injection level on p-side of junction. The solid curves are simple calculations from Eqs. (6) and (7) while the data points are results of computer analysis.

Fig. 7. Electron quasi-Fermi level variation around high-low junction (1000 Ω·cm p-region).

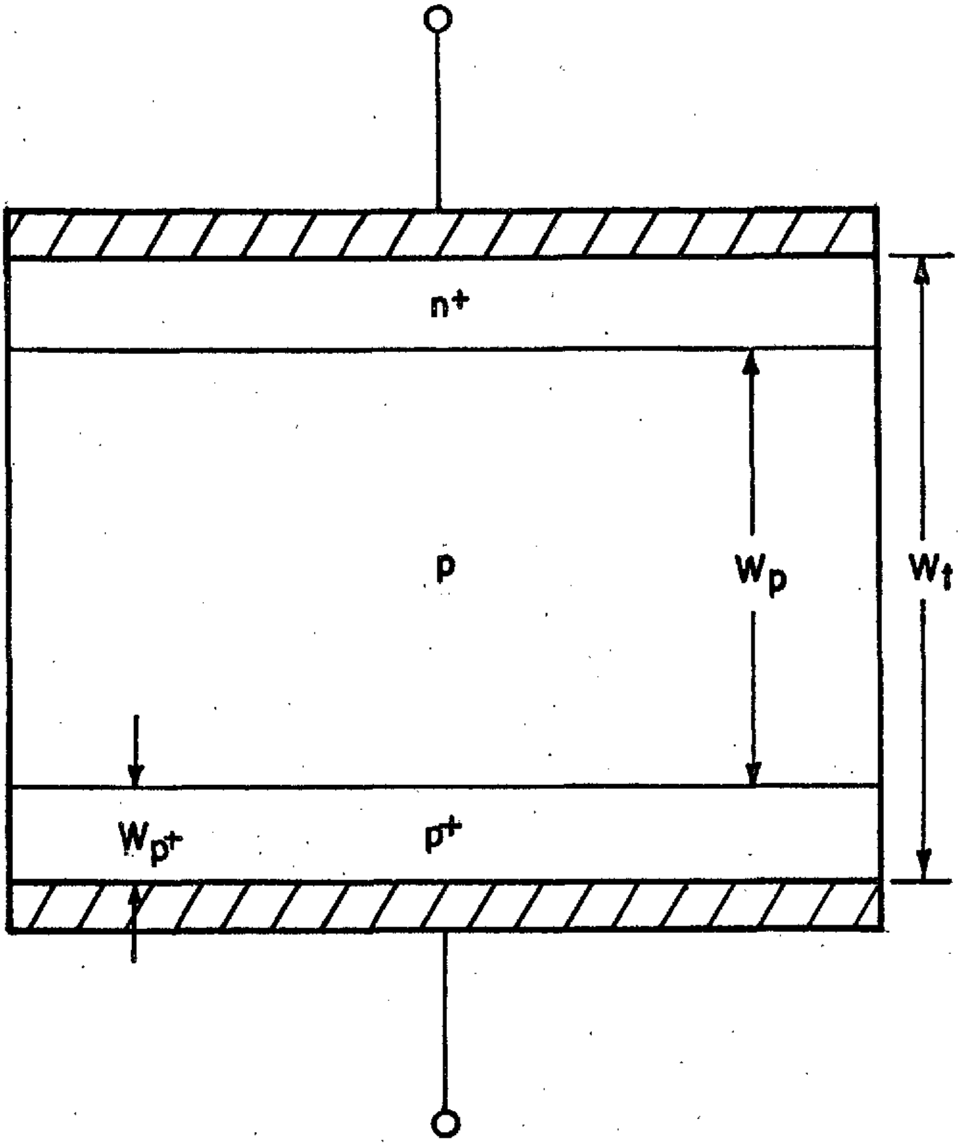

Fig. 1. Device structure for n^+-p-p^+ diode (A) 1000Ω·cm p-region, $N_p = 7\times10^{12}/cm^3$, $N_{p^+} = 10^{18}/cm^3$ (B) 10Ω·cm p-region, $N_p = 1.3\times10^{13}/cm^3$, $N_{p^+} = 10^{18}/cm^3$.

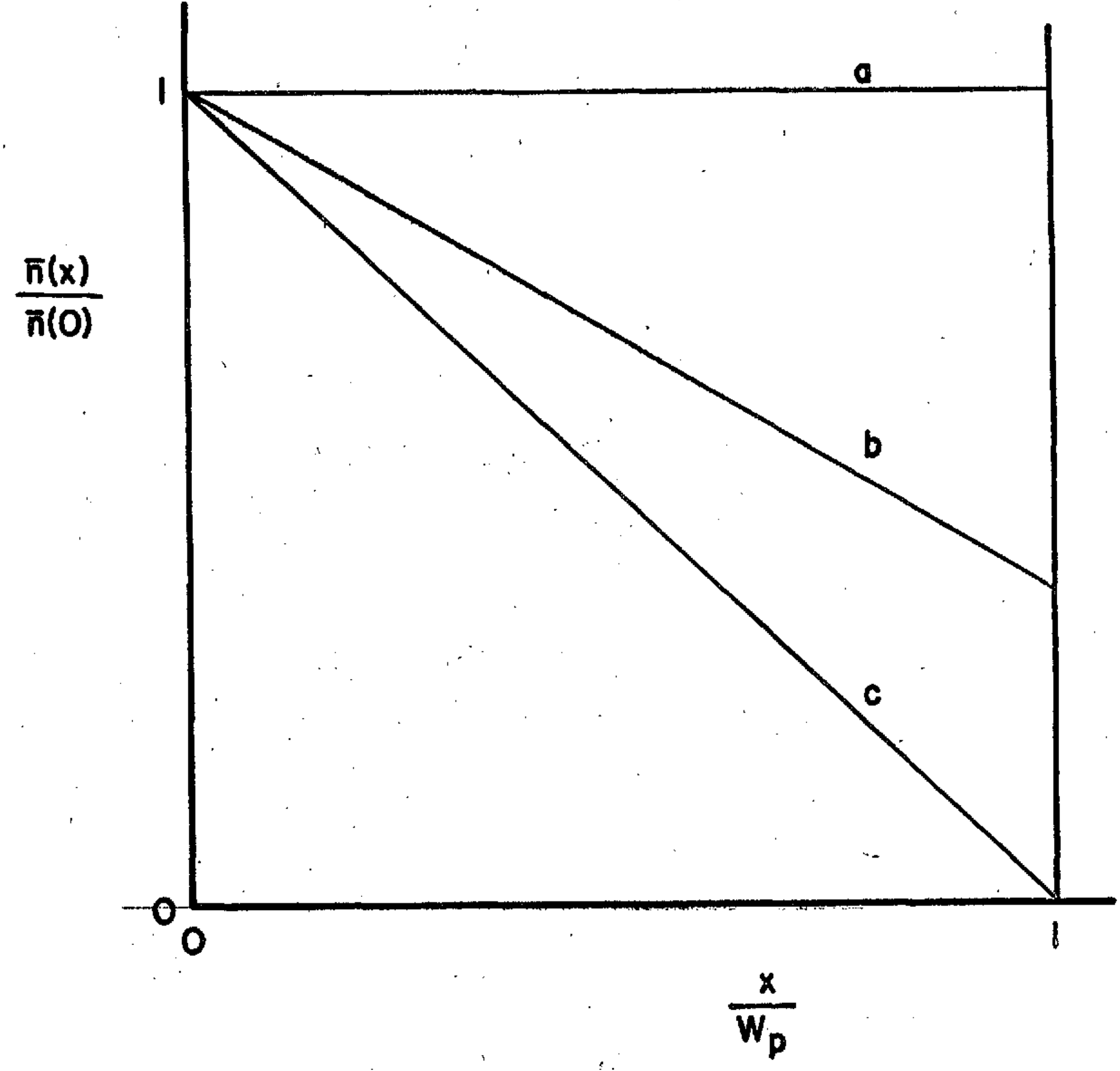

Fig. 2. Effect of back contact on injected electron concentration ($W_p \ll L_n$); (a) Ideal reflecting back contact (b) partially reflecting back contact (c) ohmic contact.

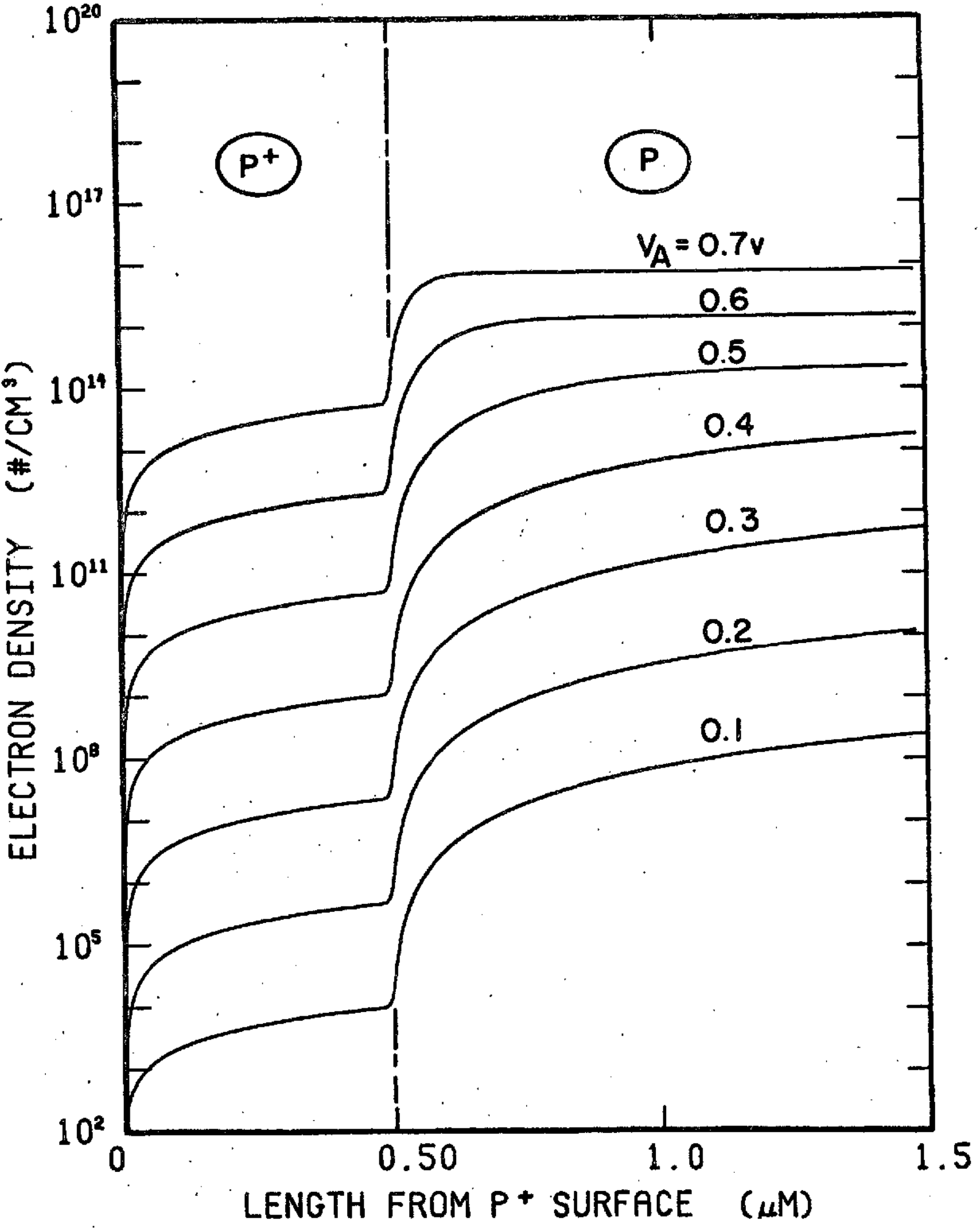

Fig. 3. Calculated minority carrier concentration around the high-low junction at various injection levels (1000 Ω·cm p-region).

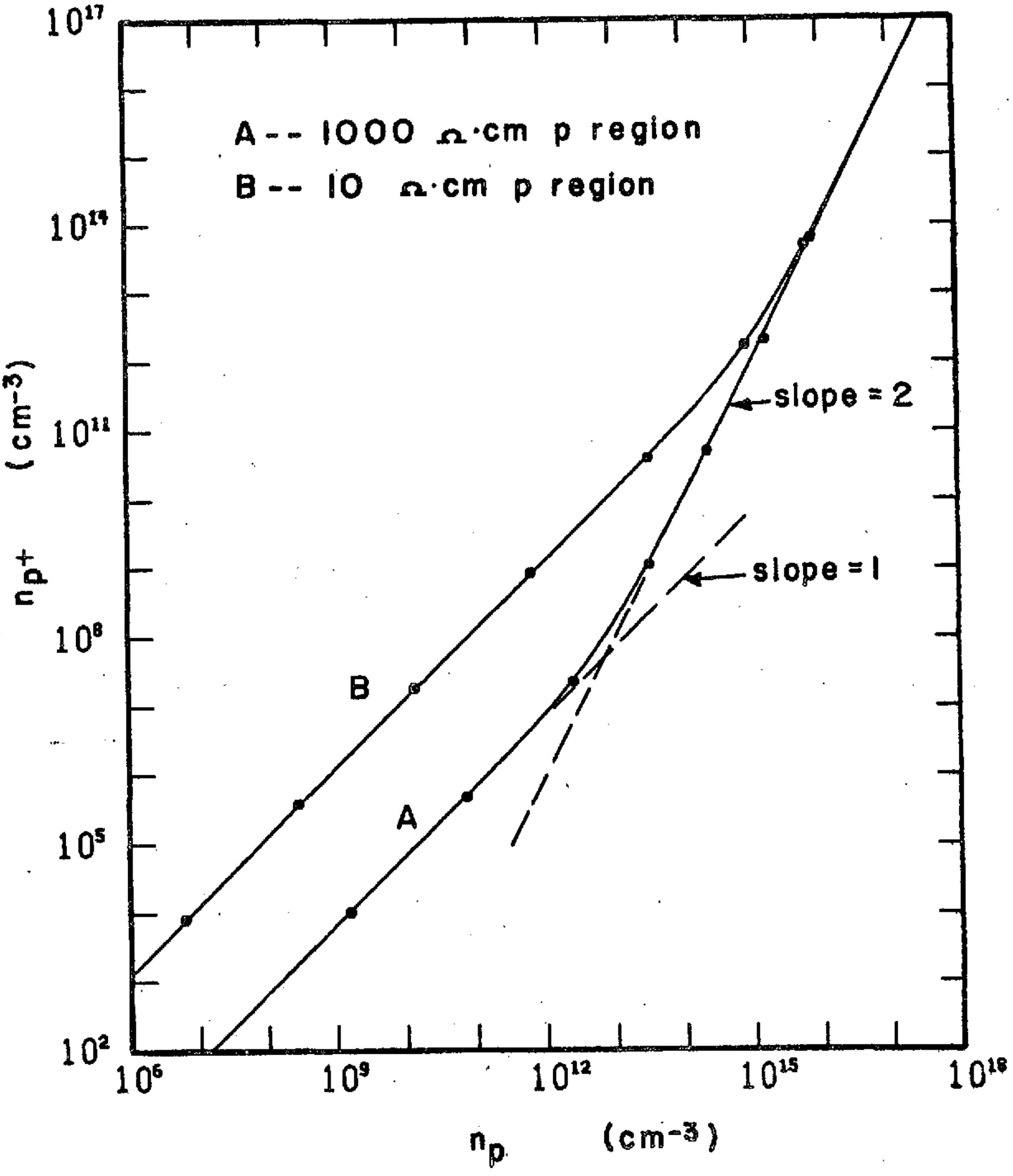

Fig. 4. Minority carrier concentration at edge of depletion region in p^+-side as a function of minority carrier concentration at edge of depletion region on p-side. The solid curves are simple calculations from Eq. (4), while the data points are results of computer analysis.

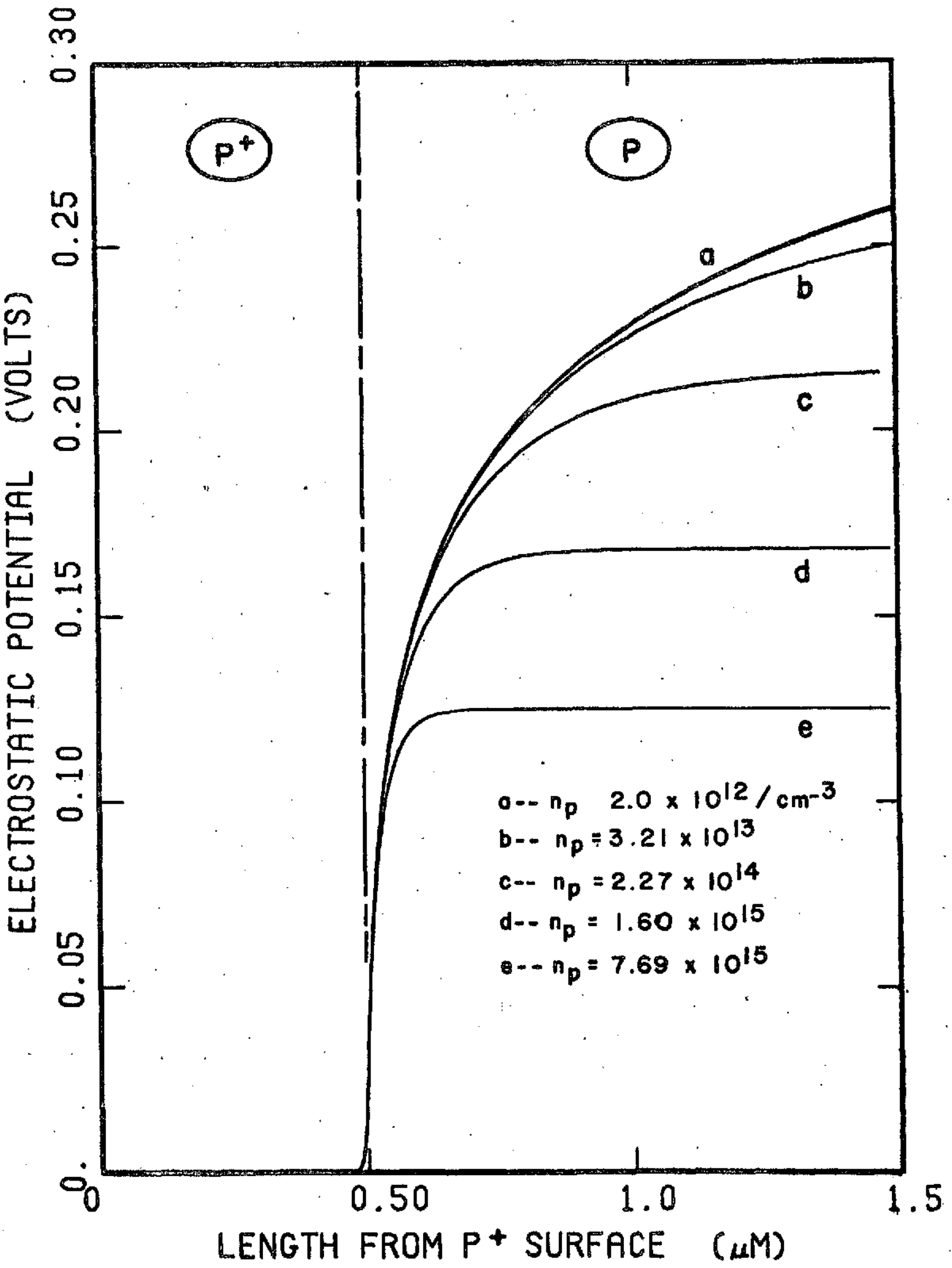

Fig. 5. Electrostatic potential around high-low junction at various injection levels (1000 Ω·cm p-region).

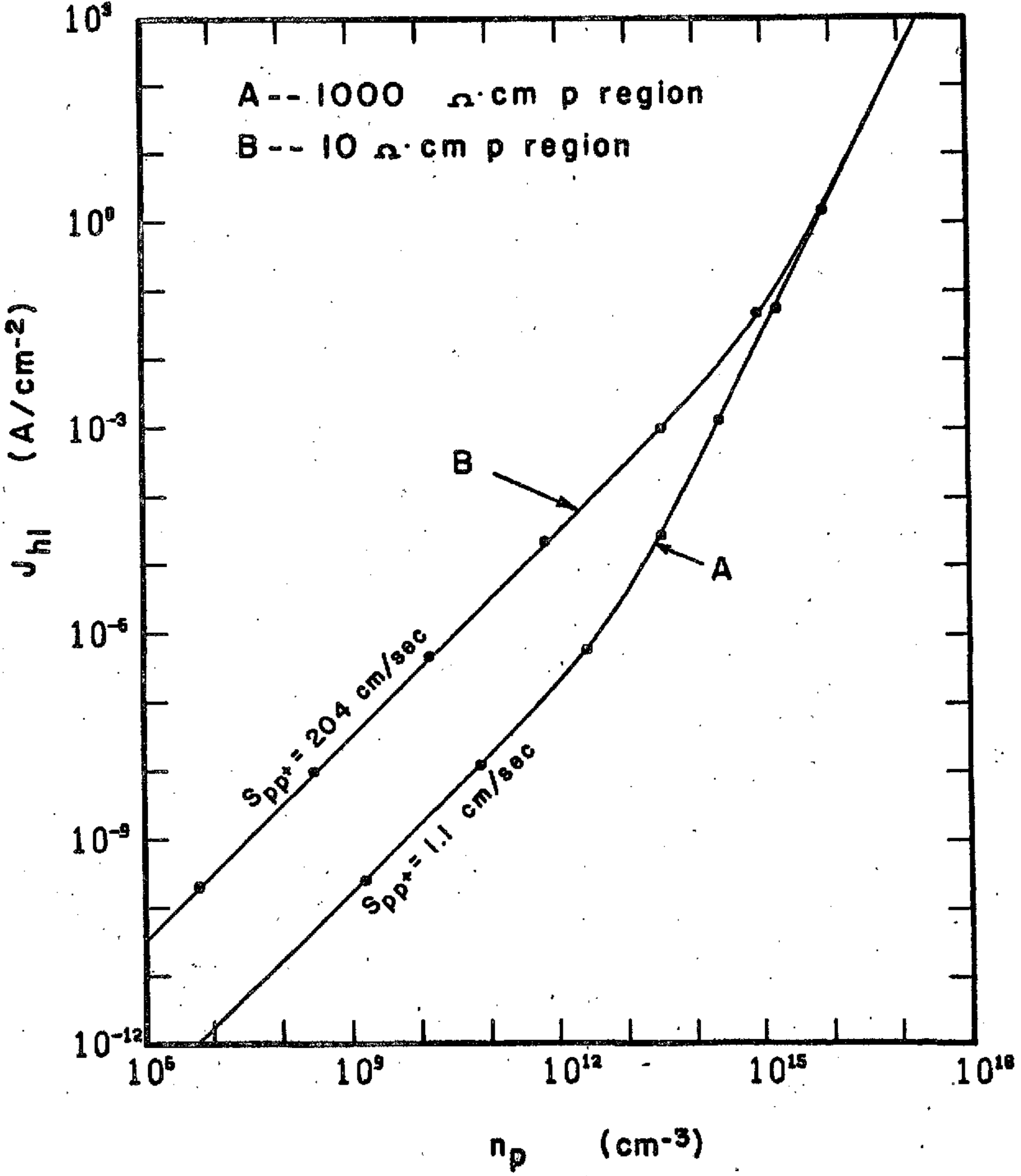

Fig. 6. High-low junction leakage current as a function of injection level on p-side of junction. The solid curves are simple calculations from Eqs. (6) and (7) while the data points are results of computer analysis.

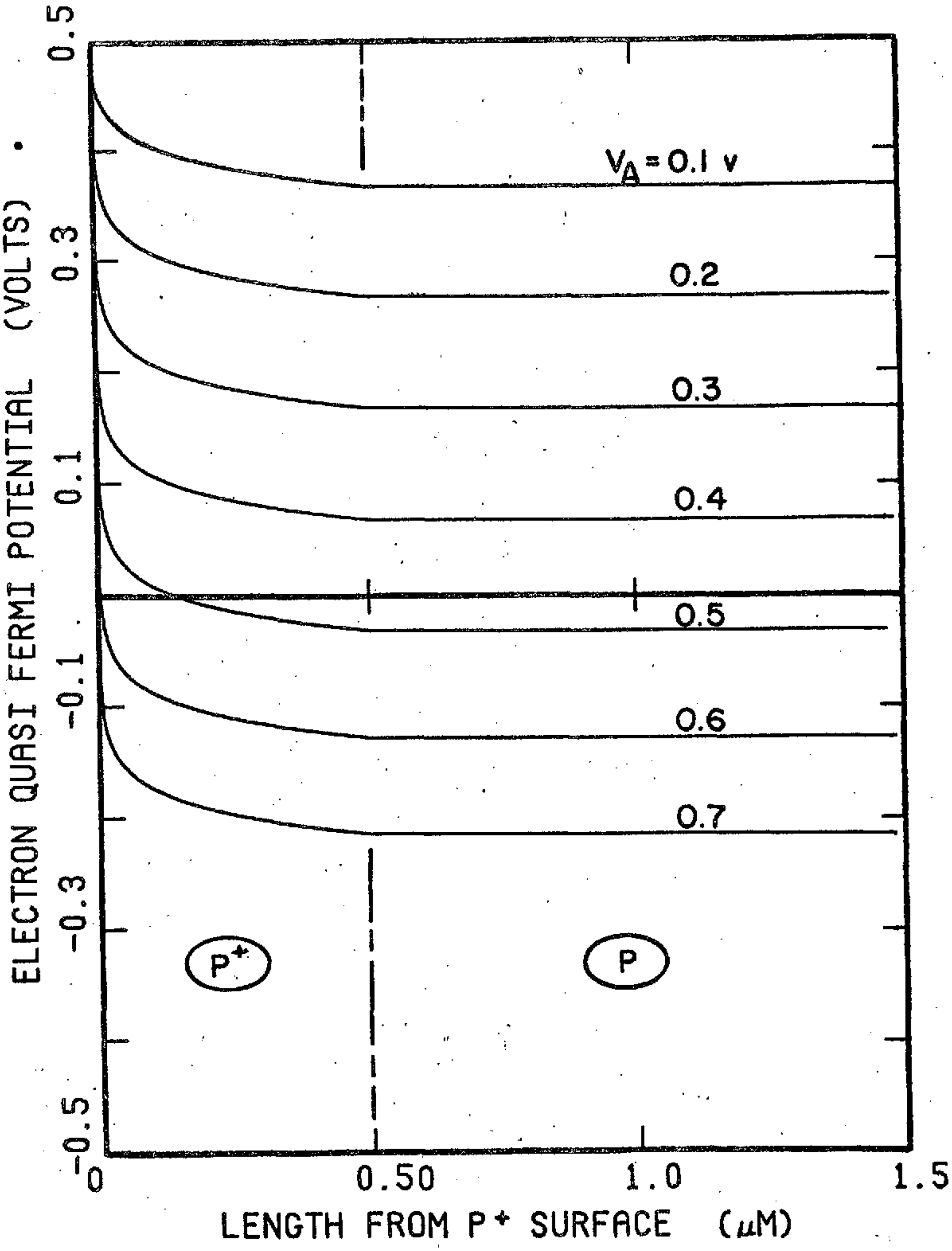

Fig. 7. Electron quasi-Fermi level variation around high-low junction (1000 Ω·cm p-region).